# REFLECTANCE CHANGE DUE TO SURFACE ROUGHNESS—WITH APPLICATIONS TO OCEAN OPTICS

A Dissertation

Presented to the Faculty of the Graduate School

of Cornell University

in Partial Fulfillment of the Requirements for the Degree of

Doctor of Philosophy

by

Wilhelmina Roa Clavano

January 2008

# REFLECTANCE CHANGE DUE TO SURFACE ROUGHNESS—WITH APPLICATIONS TO OCEAN OPTICS

Wilhelmina Roa Clavano, Ph.D.

Cornell University 2008

A simple sinusoidal function is used to study the reflectance change from a rough, homogeneous surface in two dimensions along the solar plane, and in three dimensions for a full hemispherical distribution. Results indicate that, for nadir viewing, observed radiance decreases substantially as roughness increases, but that there is virtually no change in the spectral character of the radiation. Second order reflectance contributes little to the overall reflectance even for the roughest surfaces considered. Shadowing and obscuration result in abrupt changes in reflectance for large viewing or illumination angles, which are likely to be insignificant for above-water, nadir-viewing instruments.

Light reflected into different directions by a rough, locally diffuse surface loses its Lambertian behavior as roughness increases. The darkening of a surface as observed by a remote sensing system is due to the redistribution of light into the retroreflection and forward scattering directions. It is shown that the geometric variation that causes the surface roughness alone can significantly affect the apparent roughness of a surface. An analytical expression is developed that describes the near-field situation and that shows how the far-field condition is reached.

To study how light is redistributed as it reemerges from an air-water-bottom system consisting of roughened surfaces with subsequent changes in indices of re-

fraction, the surface representation is transformed from a three-dimensional function describing the location and orientation of facets to a point in space with facet tilts varying according to a statistical distribution. Specular reflections from the surfaces are transferred in the system using Mueller matrices and Stokes vectors in order to include polarization that cannot easily be handled using other formulations. Model predictions match published observations. As with a diffuse surface, specular reflections are redistributed with surface roughness. The specular peak initially appears to be centered around the specular direction but moves toward the horizon with increasing incidence angle. This peak also widens with roughness but at the same time decreases in intensity. Light is polarized as it interacts with each surface in the system, however, without absorption or scattering in the medium there is very little or no significant overall effect.

## BIOGRAPHICAL SKETCH

Very lovingly called Wendy, she was raised. All her parents wanted was for her to stay home and settle well. When she was 4 years old, however, she had requested that her kindergarten teacher write down her "real" name so she could learn to write it herself. Her Dad should have seen it coming: Wilhelmina, after that woman of daring on a horse at the battlefront. At 5, she chose to learn Chinese because it sounded challenging. The Chinese school was also the only school with boys in class to play marbles with and the only one where she would not have to be separated from Ryan, her brother younger only by a year.

Instead of leaving her hometown to go to a better high school in a big city, she decided she wanted to play a little longer with her childhood friends. By the time she turned 17, she was ready to leave. She pursued mathematics for the fun of it at a Jesuit university. Although she took college for granted, it did not her and instead provided the grounding that is holding very strong. For a year after that, she vanished to do some volunteer work. Then took another year to travel with the excuse of getting an interdisciplinary environmental science degree. She returned closer to home to do research running up and down mountain streams, tinkering with weather stations and forest plots, picking up another language, and getting sustenance from single malt whiskey and Butterfinger bars.

Oh, but there was more to discover so she left again, this time with the intent of burying herself in schoolwork. But as if it could not have been helped: in almost no time she had made friends. No one back home realized she had made very good friends with a girl. Through this blond, blue-eyed Afrikaans-speaking spirit, a whole new life evolved but only as if a reawakening. The rest is a quasi-Ithacan story, left much later for the telling. This dissertation became only a side effect.

for Peter

## ACKNOWLEDGMENTS

For showing me the depth and beauty of simple questions and the value of transparency, Prof. Bill Philpot. May Life always keep you on your toes.

For opening up the wonderful world of programming, Andy Pershing.

For believing that I could read IDL like I could read French, Bruce Monger.

For dropping the line "You should know about Mullamaa" that pushed this research forward, Ron Zaneveld.

For stretching me to my limits and teaching me some, and showing me the power of the dark side, Emmanuel Boss.

For encouraging me to have a look-see at the other side of the Atlantic, Mike Clark.

For pointing the way to the treasures of the library and showing me the heart of a librarian, Mary Patterson.

For taking people on the street in to their home, Lena and Chris Kourkoutis.

For online froggies, Nuno Carvalhais. May that beach be there for strolling when our limbs begin to falter.

For surprise appearances and cheers during that *blitzkrieg* on D-day, Ethan Bernard, Bruce Monger, Mary Patterson, Todd Ansty and Matt Horak.

For all the times we have spent together and for all the times we have missed, Nick Jones, Wendy Baxter, Cassie Shigeoka, and Ethan Minot.

For many a quiet moment together and only one on the dancefloor, Mr. Bernard.

For demanding that one should only work as much as one is allowed play, Jeandrew.

For slowly leaving me go and trusting that I am always in Good Hands, my Mum and Dad.

For being at once my boon and my bane, Matthew. May our life together grow in time on top of boulders and under the stars.

Support for the initial work of this research has been granted by the U.S. Navy Office of Naval Research (ONR) Environmental Optics Program under Contract No. N00014-97-1-0721.

## TABLE OF CONTENTS

## LIST OF FIGURES

CHAPTER 1

# PROLOGUE

Day 1

First scientist: I think it works *this* way.

Second scientist: No, I think it works *this* way.

Day 2

First scientist: I'm sorry, I think *you* are right.

Second scientist: No, I'm sorry, I think *you* are right.

*Two scientists in the Bahamas in 2001*

## 1.1 Motivation

Does the apparent reflectance of a sandy bottom increase or decrease with increasing roughness? The question may seem trivial; a simple *gedankenexperiment* would have told us that if the surface were perfectly diffuse, its bright "spots" would be distributed in a wider range of directions other than straight up as its roughness increases. But would its overall reflectance decrease, and if so, how quickly, and is there a roughness beyond which there is no change? A detector would have to be extensive enough to be capable of receiving all the light leaving from the surface in all directions. How would the light be redistributed by the rough surface and would that modify the assumptions underlying a diffusely reflecting surface? If one considered a wide enough area on the surface, assuming that this is possible, would one not detect an average brightness that would compensate for any directional loss of light? How small do the roughnesses need to be to be detectable? The

simple question becomes a more interesting problem and, as it happens, is important in many aspects of imaging, from planetary remote sensing, tactical planning, computer graphics and rendering, machine vision, and the many branches that extend from these fields. It is interesting in the forward problem: if we had such and such a surface, what would it look like? It is equally interesting in the reverse problem: if we had an image of a surface, can we deduce its shape or texture?

Many of the approaches to the problem address issues raised for a particular application. In our case, the initial question had to do with the ability to distinguish the different optically shallow water bottom types that were apparent from just above-water or tell their depths by looking at the changes in their reflectances at different spectral wavelengths. For most oceanographic applications, light is measured by a detector looking in a certain direction within a narrow field of view. This adds a directional component to our problem. Would the same surface look darker or brighter as we move toward looking at grazing angles, i.e., very close to parallel the surface? Are there ways to optimize the observations for particular types of measurements? How does the direction dependence affect the directional distribution of its roughness if such a directionality exists?

The simple answer is: As the rippling, the deepening of the troughs and the heightening of the peaks, of a submerged shallow bright sandy bottom in clear natural water intensifies, it becomes less bright than a similar material but flat surface. The energy distribution is also significantly different than that of a flat surface. This, nonetheless, leads to further questions.

Can one measure the effect of surface geometry and be able to separate it from material effects given the specifications of an instrument? How much does the surface reflectance change as one moves farther away from the surface? What

would the behavior of the full reflectance distribution look like? What would the difference be between a shiny and a dull surface? What follows is the story of further explorations.

## 1.2 Overview

The use of a sinusoid is perhaps the simplest way to express the roughness or shape of a surface and to vary it. For a sinusoid, the ratio of the amplitude to the period of its defining waveform provides a simple, convenient measure of roughness. Specifically, we choose as a roughness measure the ratio of half its height to its period and use this throughout the three main parts of this work, even as we move from two to three dimensions.

In two dimensions, the surface geometry is the simplest and allows the easy inclusion of absorption by the water medium, multiple reflections on the surface, as well as shadowing and obscuration effects. Changes in reflectance in Part I (Chap. 2) are affected by the distance light traverses in the water; the longer these paths, the greater the opportunity that light is absorbed and thus less light emerges. The surface in Chapter 2 is assumed to be perfectly diffuse such that light incident at a point on the surface is equally scattered in all directions. A tilted part of the surface thus contributes to light incident on other parts of the surface. However many interactions light has with the surface determines the order of scattering. To study the effects of multiple scattering we explore second order reflections. Also, because we are mainly concerned with the geometrical effects of roughness, the phenomena of shadowing and obscuration are explored. It turns out that care is required in choosing the functional expression to represent a surface to properly take these into account.

A related question of how much brighter or darker an undulating surface appears when a detector sees different portions of it is addressed in Part II (Chap. 3). When a detector is close enough to the surface it may see only a portion of a waveform and the observed reflectance can be expected to change with the distance from the surface. Chapter 3 is dedicated to finding an analytic expression to understand the purely geometrical effects of viewing the surface in transition from the near-field to the far-fieldcase. In this chapter we move into three dimensions but keep the detector looking straight down. Furthermore, there is no absorption in the water and the air-water interface is ignored. This short exposition confirms our results in Chapter 2.

Part III (Chap. 4) is a preliminary attempt to treat the entire system including a realistic water surface and a rough bottom. In order to simplify the calculations in three dimensions, a statistical distribution of slopes at a single point in space is used to represent the surface and thus the light distribution below the water surface. This distribution can then be assumed to be spatially invariant, as if the slopes were distributed randomly over a two-dimensional water surface. Absorption in the water is again ignored. No multiple reflections are allowed. Only the specular component of the surface interactions is studied for this preliminary test. These simplifying assumptions facilitate the analysis of the directional distribution of the reflectance, further confirming previous results. Vector calculus and Mueller matrices are used because they provide the most convenient way of following the interactions of and describing light transfer in the system. The measure of the polarization state of light at any point is intrinsic to a Mueller matrix and allows us to briefly analyze polarization changes throughout the system. However, without absorption in the system polarization effects induced in the system by

surface roughness alone are negligible. The model formulation does not prohibit absorption, but is left for later investigations.

The treatments in Chapter 2 only deal with light traveling in two dimensions, and on the principal plane. Surface roughness in this system has an infinite boundary on either side of this plane. Although the surface is extended into three dimensions in Chapter 3 there is no directional reflectance distribution to consider, the only viewing direction being straight down. The calculus developed for the Mueller matrix approach (more below) allows for the computation of the directional distribution of light, but also introduces a whole new notation set. We modify it only as needed to distinguish the variables that change as the light is transferred within the system. In Chapter 2 we adhere closely to the notation set out by Mobley (1994) that is used by the ocean optics community. A greater generalization was desired in Chapter 3 and, because it was mostly a calculus problem, we used notation for vectors from general calculus, including attaching spherical trigonometric concepts as required, while tending to the notation of the wider field of optics.

## 1.3 Radiometry basics

A plane angle is measured in radians and its unit measure is defined as the ratio of the length of arc on a circle to its radius (Fig. 1.1):

$$\theta = \frac{l}{r}\,[\text{rad}]\,. \tag{1.1}$$

The concept of a solid angle is an extension of this idea into three dimensions. Imagine a sphere given some radius, $r$, the "angle" that encompasses a projection of this area onto the origin of the sphere—or hemisphere, for that matter—is known as a solid angle. It is measured in steradians and is defined as this area over the

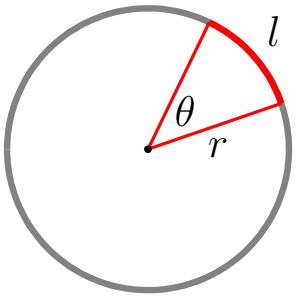


Figure 1.1: A plane angle $\theta = l/r$, in units radian, but essentially dimensionless.

radius squared; again the result is dimensionless (Fig. 1.2):

$$\Omega = \frac{A}{r^2}\,[\mathrm{sr}]\ . \tag{1.2}$$

The short introduction above to the measure of spherical angles allows us to define the two radiometric quantities that are relevant to the study of light transfer here (see Nicodemus 1976 for standard definitions of the other quantities and their interrelationships). Within the realm of geometric optics, a time average can be assumed so that light impinging at a point on a surface is measured in radiance as the power per unit area per unit solid angle. This can be visualized using the concept of the solid angle. Radiance is the amount of energy $\Phi$ (in Watts) incident at a point through an area $A$ (in square meters) that subtends a solid angle $\Omega$ (in steradians) at that point is

$$L = \frac{\Phi}{A\,\Omega}\,[\mathrm{W\ m^{-2}sr^{-1}}]\ . \tag{1.3}$$

Of the other units of measure in radiometry, the only other one relevant to the development that follows is irradiance. Strictly speaking, irradiance is simply the radiant power incident on a surface. For our purposes, however, we are concerned

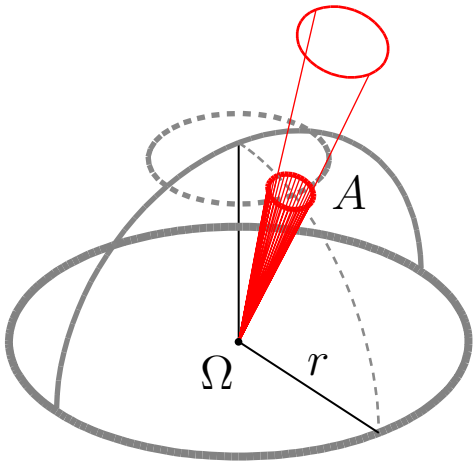


Figure 1.2: A solid angle is an angular measure in three dimensions that is defined by the ratio of the "area" of interest projected onto a spherical surface to the square of the radius of the sphere, thus $\Omega = A/r^2$[sr] in units steradian, but essentially dimensionless.

specifically with hemispherical, directional irradiance, which is the amount of light incident on a surface from the whole half-sphere that can illuminate that point. For illumination in the present case, we are concerned with downwelling irradiance, which can be understood as the integral of the radiance from all directions of the hemisphere above a surface that is incident on that surface, thus

$$E = \int_0^{2\pi} \int_0^{\frac{\pi}{2}} L(\theta, \phi) \cos\theta \sin\theta \, d\theta \, d\phi \, [\mathrm{W\ m^{-2}}] \, . \tag{1.4}$$

The cosine factor in the equation arises from the decrease in radiance due to a foreshortening of the projected area parallel to the direction of propagation of light relative to the surface normal and the sine factor a result of the transformation from Cartesian to spherical coordinates (a result of the Jacobian matrix of transformation).

CHAPTER 2

# PART I. REFLECTANCE CHANGE FROM A TWO-DIMENSIONAL SURFACE

## 2.1 Abstract and introduction

Reflectance is a function of the shape of the reflecting surface as well as the inherent optical properties of the reflecting material and the adjoining medium. We analytically model the effects of morphology on the spectral reflectance of collimated light incident upon a submerged, locally Lambertian, sinusoidal surface. The model includes shadowing and obscuration, which affect variations in the observed in-water reflectance due to changes in the incidence direction. When the incidence angle is low, some of the light is not reflected into the direction of observation; when the observation direction is low, some of the light–although in a path toward the observer–is blocked from view. Changes in the reflectance are apparent in first order reflections from the sinusoidal model. As roughness increases the amplitude decreases and non-Lambertian behavior becomes apparent. Effects due to second order reflections are small. Spectral differences in reflectance are dominated by absorption by the medium due to increased optical paths.

Light reflected from shallow waters is a function of the water optical properties, the depth of the water and the inherent reflectance of the bottom. Since even clear water is a strongly absorbing medium over the depths of interest in coastal bathymetry, even small changes in the optical path can have a significant effect on the overall reflectance. This effect allows for reasonably accurate bathymetric mapping when the bottom reflectance is uniform; however, Lyzenga (1978), Philpot (1989), and Mobley et al. (2003) show that there may be appreciable errors in the

retrieved depths if there is a change in the bottom reflectance. Mobley et al. (2003) suggest that the errors are no more than 10%. The problem is complicated by the sensitivity of errors to spectral attenuation by water and the spectral reflectance of the bottom. Voss et al. (2003) show from measurements that a bright underwater sandy bottom has radiances increasing toward nadir compared to deep water where it increases toward the horizon. We pose the problem here of the additional sensitivity of reflectance to bottom roughness.

It is common to assume that the bottom can be treated as a flat, perfectly diffuse (i.e., Lambertian) surface. This assumption has been useful in studies using passive optical remote sensing to extract bathymetry (e.g., Lyzenga 1978, Carder et al. 1993) and to classify bottom type (e.g., Hochberg & Atkinson 2000, Louchard et al. 2003). However, it is not clear whether these assumptions are generally valid, or whether they are valid only over a limited range of conditions. For example, the applications cited above each use a specific viewing geometry defined by the remote imaging system used. In other cases, when the viewing geometry varies significantly, or when the surface is not flat within the field of view (FOV) of the detector, or where the Lambertian assumption is simply inadequate, there may be coincident changes in the expected reflectance pattern. A further complication is that the spectral dependence of specular reflectance is different from that of diffuse reflectance. Spectral reflectance (treated as a surface property) follows from the Fresnel equations and depends entirely on the complex refractive index of the material at a particular wavelength. To the extent that diffuse reflectance includes volume reflectance, it is dependent on the scattering properties of the material. For the particular case of an air-water system where the light source is in air, strong reflection from the source in the specular direction becomes evident.

However, where specular reflection is minimal, the water looks dark, perhaps blue or green depending on the constituents in the water column. For now we only deal with the diffuse distribution of light, taking into account only the light that is "returned" to the detector after having interacted with the water and the bottom and then transmitted back up through the air-water interface.

In the model as it is formulated here, a change in the index of refraction of the bottom surface is allowed but the volume scattering by the surface material is ignored. The other obvious surface in the system is, of course, the air-water interface, where because light travels through a boundary layer between two different media (with different refractive indices), it is either refracted or reflected back. However, we assume that this interface remains flat and only effectively changes the direction of the incoming and outgoing light. Finally, we assume that the water is homogeneous and purely absorbing (i.e., there can be no scattering of light out of its path).

The purpose of this chapter is to develop an analytical model of spectral reflectance from a submerged, undulating surface as a means of exploring the variability in spectral reflectance for remote sensing in shallow water environments. The model includes shadowing and obscuration effects on reflectance, as well as roughness effects. There are two roughness scales of interest: the local roughness scale that is much smaller than the detector FOV (or "footprint"), but much larger than the illuminating wavelength, and the bottom morphology that can be rough on a scale that is the same order as the detector footprint. On the local scale we consider areas small enough to be modeled as flat, diffusely reflecting facets. Changes in apparent reflectance are then associated with changes in roughness that are on the order of the "size" of the detector FOV. We treat the water column as

a purely absorbing medium, with no scattering or internal light sources. Spectral changes in reflectance is then due to the absorption of light along its path in the water as well as spectral reflectance from the bottom. We use a sinusoidal function to represent the reflecting surface so that increasing the amplitude-to-period ratio of the analytic function of the surface is analogous to increasing the surface roughness. Using a continuously differentiable surface facilitates examination of the effects of shadowing and obscuration.

In this section we begin by describing the model setup with the assumption that the theory of geometric optics applies (i.e., the roughness scales are much larger than the incident wavelength) and that the optical properties are time-averaged. The concept of shadowing and obscuration is discussed before presenting an analytical expression of the model. We focus the discussion of modeling results first on the effects of bottom morphology, then on the change in the spectral shape due to changing morphology and the attenuation in the light field.

## 2.2 Background

The classic and most commonly used description of diffuse reflectance is Lambert's cosine law (Lambert 1760), which states that reflectance is proportional to the cosine of the incidence angle. Although simple and useful, the Lambertian model has long been known to be inaccurate for a number of important applications. Minnaert (1941) suggests that the reflectance of diffuse surfaces is symmetric about the normal to the surface and uses a model that is proportional to the product of the cosines of the incident and emergent angles relative to a measure of surface roughness. This is a modification of an empirical non-Lambertian model of the moon. Oren & Nayar (1995) assert that the Minnaert model, although obeying

the reciprocity principle (reversing the light source and detector locations, see later Eq. eq:reciprocity), has no physical foundation and proves to be incorrect.

Several recent models have been developed in order to more accurately describe reflectance from a rough surface. Hapke (1993) and Oren & Nayar (1995) discuss the use of randomly oriented facets to represent the surface of interest, the former with bottom surface peaks and depressions at the same levels, the latter with each facet having its highest point at the same level as all the other facets but having different depression levels. Torrance & Sparrow (1967) as well as Zaneveld & Boss (2003) use a more symmetric form: a triangular wave with each facet having constant slope on either side of a global normal to represent the reflecting surface. As is illustrated later, such representations result in abrupt, discontinuous effects on the surface reflectance that can be significant at the small scale. The footprint of a detector looking straight down sees equivalent parts of a sinusoid wave and a triangle wave. However, with the assumption of parallel incoming rays there can be abrupt effects to the illumination of areas of a triangle wave that a sinusoid does not–even in the extended case where more wave periods are illuminated and viewed.

Laboratory measurements of reflectance from rough surfaces exhibit two significant deviations from a Lambertian model. The first, as Oren & Nayar (1995) show, is an increase in reflectance observed when the viewing direction approaches the direction of illumination, a feature that appears in virtually all their observations. This feature is variously known as the opposition effect, the "hot spot", the retroreflection peak, or (dry) Heiligenschein (Minnaert 1948), and is caused by enhanced brightness at small angles between the incidence and scattering directions when shadows caused by small-scale roughness features are not visible (e.g., sand

or vegetation canopies, Mobley et al. (2003)). Hapke (1998) suggests that this may be caused as much by coherent backscattering effects as it is by shadow hiding. The second deviation is a distinct reflectance peak at angles slightly off the specular angle observed by Torrance & Sparrow (1967). They show non-Lambertian behavior resulting from a triangular wave model, the roughness of which is determined by the distribution of slopes of the grooved facets. Each facet includes a specular component and a Lambertian, i.e., diffuse, component. Torrance & Sparrow (1967), simultaneously considering shadowing and obscuration, succeed in reproducing both the hot spot and the off-specular peak. They do not explicitly include higher order reflections (interreflections), but assume that the diffuse component averages out these effects.

Furthermore, to show that the opposition effect is not part of the specular component of reflectance, Oren & Nayar (1995) model the bi-directional reflectance distribution function (BRDF) of real surfaces without the specular component. Their model demonstrates an increase in reflectance near the retroreflection direction and a decrease in reflectance away from it that becomes more pronounced as the roughness of the surface increases. The opposite is true for higher order reflections, where the reflectance is negligible near the retroreflection direction and uniformly increases away from that direction. Close to the retroreflection direction both shadowed and obliquely illuminated areas within the detector FOV are decreased. Away from these directions the proportion of area viewed that is shadowed and obliquely illuminated increases and the directly illuminated portion decreases (see also Hapke 1993). Since the surfaces that are weakly lit by indirect illumination contribute to higher order reflections, these areas may be important when considering higher order reflectance.

Multiple reflections also alter reflectance in the specular direction. Torrance & Sparrow (1967) suggest that multiple diffuse reflections increase the diffuse reflectance of a surface and thus the peak around the specular direction (indeed, the peak is not always exactly in the specular direction). In fact, Shen & Maradudin (1980) show that surface roughness reduces the specular component, suggesting that multiple reflections (disregarding any specular reflectance) drives the enhancement in the specular direction. Gu et al. (1993), however, suggest that the effect is due to single scattering alone, but from a rough surface. Otremba (2004) suggests that this second maximum (the first being in the backscattering direction) is caused by single *and* multiple scattering. How significant this contribution by multiple scattering is not clear.

In general, estimates of the effects of surface roughness indicate that higher order reflections may not contribute significantly to the overall detected brightness of a surface. Hapke (1993), in a special model designed specifically to estimate second order reflectance, uses a hemispherical cup as a surface shape model to give a maximum estimate (illumination and detection at nadir) of roughly only a 6% contribution by second order reflections to the overall brightness from the lowest area of the cup where the maximum reflectance is expected.

Observations of the BRDF of ooid sediment underwater by Zhang et al. (2003b) show deviations from pure Lambertian reflectance very similar to those modeled by Oren & Nayar (1995). In their measurements the hot spot is very evident but the off-specular reflectance peak is not apparent and present an empirical model that fits their experimental data well. In contrast, observations of the BRDF of corals in very shallow water by Joyce & Phinn (2002) show little evidence of the hot spot but a pronounced off-specular peak. This, however, may be due to specular

reflection from the water surface since the measurements were made above water. They also note significant variability in the BRDF that appears to be associated with differences in the morphology of the corals studied. Note that they assume that the spatial and spectral variability are independent of one another.

In the references cited above, the focus has been on the deviation from Lambertian behavior of surfaces that are rough on relatively small scales, but essentially flat at the scale of the detector FOV. Zaneveld & Boss (2003) provide a theoretical treatment of this problem for a detector positioned at nadir (a convenient viewing direction for remote sensing in shallow waters) and viewing multiple waveforms. They represent a rough, sandy bottom as a sequence of triangular waves with Lambertian facets. Considering only first order reflectance (with neither shadowing nor obscuration), they show that the effective reflectance of the bottom is proportional to the average cosine of the bottom slope and that, for these conditions, the observed reflection from a rough surface can differ from that of a flat surface by as much as 30% depending on the roughness type. Oren & Nayar (1995) show similar results for a nadir-viewing detector and incidence angles of 45°, 60°, and 75°. The goal in this paper is to develop an analytical model for a rough, but differentiable surface. The intent is to produce one that is general enough to span the differences in the designs of the existing empirical models and related experiments.

## 2.3 Surface description and roughness measure

A shallow-water bottom is represented as a sinusoidal surface that is homogeneous, locally Lambertian and of infinite lateral extent. We consider sinusoidal surfaces of varying widths and amplitudes from a nearly flat bottom surface to a waveform

that is undulating, with an analytic form given by the function

$$f(x) = a \sin\left(\frac{2\pi}{l}x\right) , \tag{2.1}$$

where $a$ is the amplitude of the waveform and $l$ is its period. While we are ultimately interested in the apparent reflectance that could be detected by above-water sensors, we limit the initial results to upwelling radiances that would be perceived at a plane, **W**, just below the water surface (i.e., being fully submerged) and utilize the geometry of an operational reflectance sensor in the model. This last condition, in effect, avoids the need to account for atmospheric effects in the model and omits complications caused by transmission effects at the water surface. However, for completeness, the analytical expressions that are developed in this paper include the transmission of reflectance leaving through the air-water interface toward a sensor above the water surface.

We define a single waveform (Fig. 2.1) to be that area from crest to crest of the bottom surface, with an amplitude-to-period ratio $a/l$. The distance $z$ is that from the average water surface height, **S**, to the level that represents the average depth of the bottom waveform (this becomes the bottom surface reference plane), **T**, which is set to be perpendicular to the global normal. Another distance, $\nu$, is defined here to represent the distance from the detector plane fully submerged just below the water surface to the level of the highest point of the bottom waveform, **U**. This distance is held constant and is determined by the period of a single waveform so that the detector only sees this single unit waveform. An elementary beam of radiance $L_0$ from a source just above the water surface is first incident at some point **0** on the water surface. The beam is either reflected upward ($L_{\mathrm{w}0}$) or transmitted down ($L_0{}'$) toward some point **1** on the bottom surface.

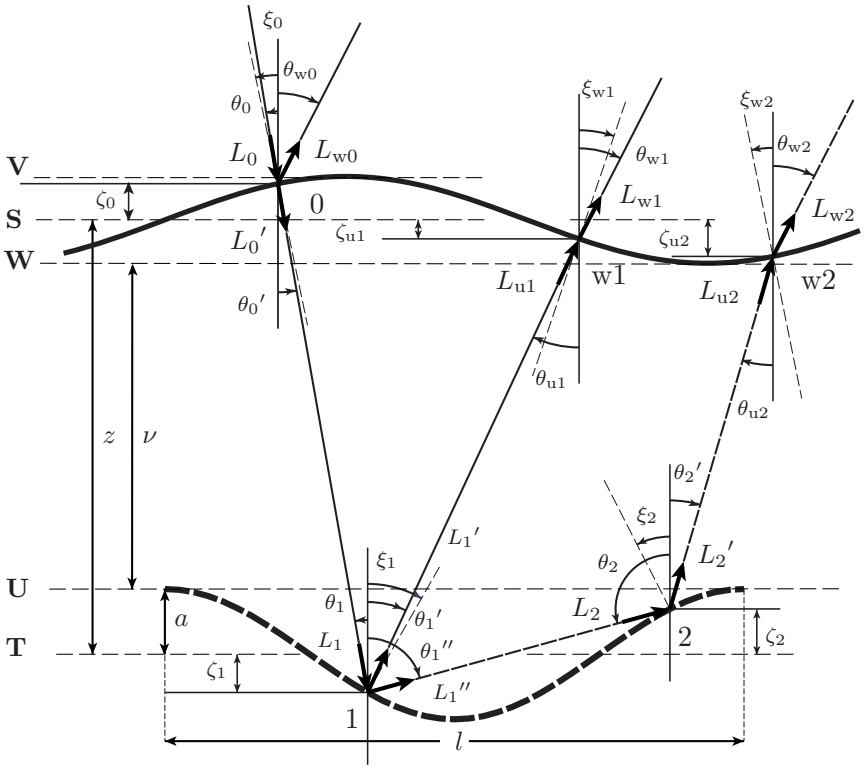


Figure 2.1: Diagram for the modeling environment on the scattering (or solar) plane $\phi_0$. Here we show a single source beam incident on the water surface at point **0** making an angle $\theta_0$ from the vertical. This is refracted and impinges on point **1** on the bottom waveform at an angle $\theta_1$, that then either travels back through the water column to point **w1** in the direction $\theta_1'$ or is interreflected along the bottom towards point **2** in the direction $\theta_1''$ and reflected again in the direction $\theta_2'$ out into the air through point **w2**. $L_i$ represents the radiance impinging at a point on the bottom for the $i$th time, $L_i'$ the radiance reflected off that point, and $L_i''$ the radiance interreflected the $i$th time towards another point on the bottom. $\xi_i$ represents the local normal at point **i**, and $\zeta_i$ the vertical difference between a point and its reference surface level, which could either be the water surface average height, or the bottom waveform average depth. The difference between these reference levels is the distance $z$ and $\nu$ is the vertical distance between the levels of the highest point along the bottom and the lowest point of the water surface. The amplitude of the bottom waveform is designated by $a$ and its period by $l$.

Now, assume that the water is optically homogeneous both vertically and horizontally and that the bottom surface is an opaque boundary layer such that any volume reflectance is included in $\rho$, the surface radiance reflectance function. The angle of the local normal, $\xi_i$, is at a point along the bottom, $i$ referring to the $i$th order reflection. $\zeta_i$ is the vertical distance of point $i$ on the bottom to the bottom reference plane $\mathbf{T}$, while $\zeta_{wi}$ is the distance of a point on the water surface to the water surface reference height.

We consider only first and second order reflections from the bottom, $i = 1$ and $i = 2$, respectively, although the final expression has been developed to be used to describe $n$th order reflections. The terminology and notation here follows closely that of the ocean optics community (see, e.g., Mobley 1994). From a radiance $L_0{}'$ that is refracted and transmitted through the water surface, an attenuated value $L_1$ impinges on the bottom at point **1**. First order reflection from point **1** results in radiance $L_1{}'$ that is incident on the air-water interface from below (i.e., water-incident) on some point **w1**, determined by the viewing direction. The same reflection event also produces radiance $L_1{}''$ that is incident at point **2** on the bottom as radiance $L_2$ after being attenuated. That second order reflection produces radiance $L_2{}'$ that is water-incident at some point **w2** as $L_{u2}$, the direction of the latter is determined by the detector orientation. Transmitted radiances emerging above the water surface at $\mathbf{w}i$ are denoted as $L_{wi}$, where $i$ again is the order of reflection. Each local normal denoted $\xi_i$, centered at a point $\mathbf{i}$, has radiance reflected in the direction represented by the polar angle pair $(\theta_i, \phi_i)$ in the global spherical coordinate system, and radiance is transmitted in the direction $(\theta_i', \phi_i')$.

The notation for the local normals ($\xi$), and zenith and azimuth angles $(\theta, \phi)$ relative to the global vertical for the incident, reflected and transmitted direc-

tions match that for the radiance representation (e.g., $(\theta_0', \phi_0')$ is the transmitted direction through point **0**, and so on).

At present we assume optically shallow waters in which the bottom depth is less than one attenuation length for a specific wavelength considered, $\lambda = 550$nm in this study. Furthermore, only the case in which the bottom waveforms are oriented in the direction of the solar plane is considered, both because it is a simplification and because this is the case for which the effects of the illumination direction $(\theta_0, \phi_0)$ on the reflectance is at a maximum. Recall that the bottom surface reflectance function is assumed to be locally Lambertian, i.e.,

$$L_i' = \frac{\rho E_i}{\pi} , \tag{2.2}$$

for $i \neq 0$, where $E_i$ is the incident irradiance, $\rho$ denotes the local (directional-hemispherical) radiance reflectance function (assumed to be an inherent optical property of the material), and $i$ designates the incoming beam, which results in the $i$th order reflection $i'$ or interreflection $i''$. Thus, the radiance $L_i$ impinging on a surface along the path towards point $i$ results in the reflected or interreflected radiances, $L_i'$ or $L_i''$, from point $i$, respectively.

Given an above-water source illumination direction, $(\theta_0, \phi_0)$, we simulate a collimated beam by defining an extended, unidirectional source, **V**, on a horizontal plane just above the water surface (corresponding to infinitely distant sun-only illumination). A detector on a plane, **W**, fully submerged just below the water surface senses the reflected radiance. The detector views a single waveform and is assigned some viewing direction, $(\theta_{ui}, \phi_{ui})$, where its azimuth angle is set to $\phi_{ui} = \phi_0$ or $\phi_0 + \pi$. Note that in theory, both the source and detector planes may be placed above or below the water surface. The location of these planes,

along with the modeled bottom incidence and reflection points determine the path lengths to be considered for all order reflections.

## 2.4 The transfer equations: multiple reflections and attenuation through the water column

Oren & Nayar (1995) show experimentally that the geometry of a rough surface affects its apparent Lambertian property even in the absence of shadowing, obscuration, and multiple reflections. We demonstrate the same effects, but express the simplified radiative transfer equations analytically for multiple reflections in what follows.

An instrument viewing multiple periods of the sinusoidal surface at any one time sees reflectance effects "average out" so that at a certain distance the reflectance value converges and the condition is considered to be in the far-field case, more in Part II (Chap. 3). When only one period of the sinusoidal surface is viewed at any one time, such reflectance effects is not expected to average out and we are still within the conditions of the near-field case.

### 2.4.1 Bottom reflection

The solar irradiance, $E_{\mathrm{s}}$, just above the water surface is defined by

$$E_{\mathrm{s}}(\lambda) = L_{\mathrm{s}}(\lambda)\,\Omega_{\mathrm{s}}\,[\mathrm{Wm}^{-2}]\,, \tag{2.3}$$

where $\Omega_{\mathrm{s}}\,[\mathrm{sr}^{-1}]$ is the solid angle in steradians subtended by the solar disk, $L_{\mathrm{s}}$ $[\mathrm{Wm}^{-2}\mathrm{sr}^{-1}]$ is the solar radiance impinging at a point on that surface, and $\lambda\,[\mathrm{nm}]$ is the wavelength of incident light. All variables other than distances and angles are functions of wavelength; for simplicity, however, we omit the notation for

wavelength dependence in the succeeding expressions. Light is incident upon the water surface from a direction specified by the angle pair ($\theta_0$, $\phi_0$), where $\theta_0$ [rad] is the angular distance in radians from zenith and $\phi_0$ [rad] is the azimuth angle (here defined as the angular distance from the positive $x$-axis in the counterclockwise direction). The radiance incident from this direction at a point on the water surface with local normal $\xi_0$ [rad] is

$$L(\theta_0, \phi_0) = L_s \cos\left|\theta_0 - \xi_0\right| , \tag{2.4}$$

with the vertical bars denoting the absolute distance between the angles that may occur on either side of the zenith direction in the solar plane. For the treatment of the two-dimensional case here, the local normals are assumed to lie in the solar plane so only the distance $\xi$ from zenith is necessarily specified. The radiance leaving an area on the water surface towards the bottom in the direction $\theta_0{}'$ is expressed as

$$L(\theta_0{}', \phi_0{}') = \int_{\Omega_0} L(\theta_0, \phi_0)\,(n_w)^2\,\tau(\theta_0, \phi_0 \rightarrow \theta_0{}', \phi_0{}')\cos\left|\theta_0{}' - \xi_0\right|\, d\Omega_0 , \tag{2.5}$$

where $n_w$ [dimensionless] is the index of refraction of water and $\tau(\theta_i, \phi_i \rightarrow \theta_i{}', \phi_i{}')$ [$sr^{-1}$] is the radiance transmission function at the surface, which allows the transfer of radiance through this interface from direction $i$ into direction $i'$. $\Omega_0$ is the solid angle subtended by the source along the path to point **0**. In general, the solid angle is considered in its differential form and we have

$$d\Omega = \sin\theta\, d\theta\, d\phi , \tag{2.6}$$

where $d\Omega$ is a function of $(\theta, \phi)$; the angular dependence from here on is implied. If the reflectance hemisphere were to be subdivided in angular increments, the solid angle has an operational definition that is illustrated in Fig. 2.2. The changes

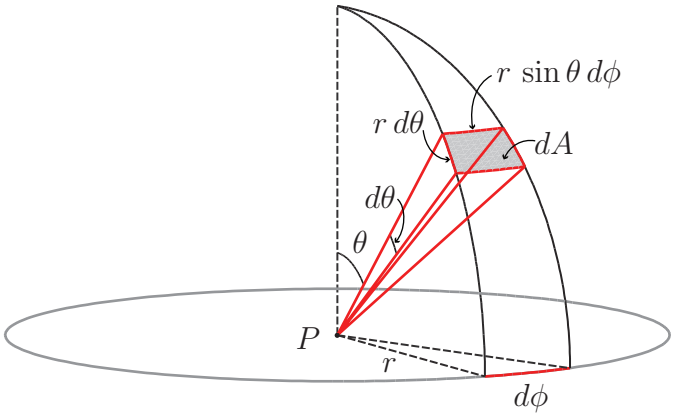


Figure 2.2: A functional representation of a solid angle for a reflectance hemisphere that is subdivided in angular increments. To simplify the concept further the hemisphere is of unit length, $r = 1$.

$d\theta$ and $d\phi$ are very small so that the projected area on the hemisphere can be approximated by $dA$. For a unit hemisphere, $r = 1$, the solid angle by definition is just this area divided by $r^2 = 1$.

With the water having an (volume) absorption coefficient $a_{\mathrm{w}}$ $[\mathrm{m}^{-1}]$ the radiance through it that would be incident on the bottom surface with normal $\xi_1$ is

$$L(\theta_1, \phi_1) = L(\theta_0{}', \phi_0{}') \exp(-a_{\mathrm{w}} d_1) \cos\left|\theta_1 - \xi_1\right| \quad (\forall \left|\theta_1\right| < \max\left|\xi\right|) \,, \tag{2.7}$$

where the distance

$$d_1 = \frac{z + \zeta_0 - \zeta_1}{\cos\theta_1} \,[\mathrm{m}] \tag{2.8}$$

is the path length from point **0** to point **1**, and the attenuation (specifically absorption in this consideration) is represented by the exponential expression along this path. Shadowing is accounted for by considering values for $L(\theta_1, \phi_1)$ alone when the primary incidence directions on the bottom are less than the maximum normal along the bottom (this refers to the condition that $\left|\theta_1\right| < \max\left|\xi\right|$ in Eq. 2.7 and Figs. 2.3 and 2.4). Finally, the radiances emerging from an area on the bottom

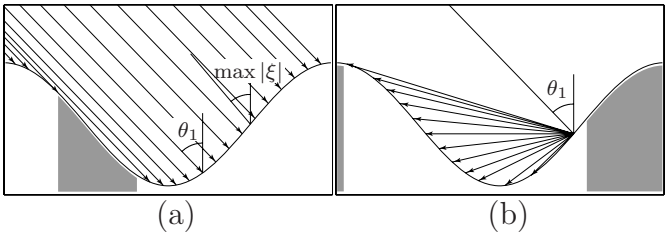


Figure 2.3: Shadowing in the first and second order. Shadowing occurs in (a) as the collimated incident beams strike the bottom at an angle $|\theta_1|$ greater than the maximum slope of the sinusoid, $\max|\xi|$. The shaded area under the curve indicates where the bottom is in shadow. For the interreflections the occurrence of shadowing is shown in (b). Here we consider a single beam and its interreflections. Again, the shaded areas indicate the portion of the surface in shadow.

surface in the directions $(\theta_1', \phi_1')$ and $(\theta_1'', \phi_1'')$ are, respectively,

$$L(\theta_1', \phi_1') = \int_{\Omega_1} L(\theta_1, \phi_1)\rho(\theta_1, \phi_1 \to \theta_1', \phi_1') \cos\left|\theta_1' - \xi_1\right| \, \mathrm{d}\Omega_1 \ , \text{ and} \tag{2.9}$$

$$L(\theta_1'', \phi_1'') = \int_{\Omega_1} L(\theta_1, \phi_1)\rho(\theta_1, \phi_1 \to \theta_1'', \phi_1'') \cos\left|\theta_1'' - \xi_1\right| \, \mathrm{d}\Omega_1 \ , \tag{2.10}$$

where $\rho\,[\mathrm{sr}^{-1}]$ is the wavelength-dependent radiance reflectance function of the bottom surface.

### 2.4.2 First order reflection

The radiance leaving the bottom toward another point on the surface is given in Eq. 2.9. Referring back to Fig. 2.1, the radiance from the bottom that is incident at a point **w1** on the water surface with normal $\xi_{\mathrm{w1}}$ in the direction $(\theta_{\mathrm{u1}}, \phi_{\mathrm{u1}})$ is

$$L(\theta_{\mathrm{u1}}, \phi_{\mathrm{u1}}) = L(\theta_1', \phi_1') \exp(-a_{\mathrm{w}} d_1') \cos\left|\theta_{\mathrm{u1}} - \xi_{\mathrm{w1}}\right| \ , \tag{2.11}$$

where

$$d_1' = \frac{z - \zeta_1 + \zeta_{\mathrm{u1}}}{\cos\theta_{\mathrm{u1}}} \,[\mathrm{m}] \ . \tag{2.12}$$

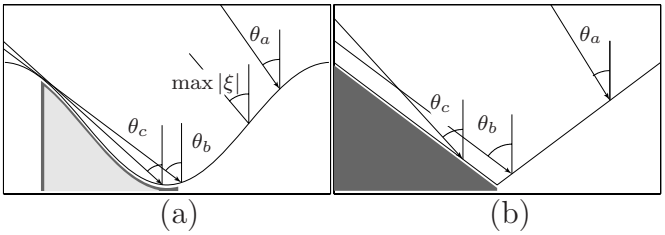


Figure 2.4: Comparing shadowing effects between a triangular wave and a sinusoidal wave. Both surfaces in (a) and (b) have the same amplitude-to-period ratio. For an incidence direction $|\theta_a|$, less than the maximum normal of the sinusoid, $\max|\xi|$, both surfaces are fully illuminated. For another incidence direction $\theta_b$, that is equal to the grazing angle of the triangular wave, half of that surface is shadowed while the sinusoid is only partially shadowed. At an intermediate incidence angle less than the grazing angle for the triangular wave, $\theta_c$, there is no shadowing; some shadowing occurs for the sinusoid when $\theta_c$ is greater than the maximum normal of the bottom waveform.

The radiance transmitted through an area on the water surface is then

$$L(\theta_{\mathrm{w}1},\phi_{\mathrm{w}1}) = \int_{\Omega_{\mathrm{u}1}} L(\theta_{\mathrm{u}1},\phi_{\mathrm{u}1})\, {n_{\mathrm{w}}}^{-2}\, \tau(\theta_{\mathrm{u}1},\phi_{\mathrm{u}1} \rightarrow \theta_{\mathrm{w}1},\phi_{\mathrm{w}1}) \cos\left|\theta_{\mathrm{w}1} - \xi_{\mathrm{w}1}\right|\, d\Omega_{\mathrm{u}1}\ , \tag{2.13}$$

where $\tau(\theta_{\mathrm{u}i},\phi_{\mathrm{u}i} \rightarrow \theta_{\mathrm{w}i},\phi_{\mathrm{w}i})$ is the transmission (at order $i$) affecting the water-incident radiance and ${n_{\mathrm{w}}}^{-1}$ is the wavelength-dependent index of refraction in this direction (i.e., from water to air).

Expanding from Eq. 2.11 and simplifying, the once-reflected radiance just below the water surface in terms of the incident solar radiance on the water surface is expressed as

$$\begin{aligned} L(\theta_{\mathrm{u}1},\phi_{\mathrm{u}1}) = \int_{\Omega_1}\int_{\Omega_0} & L(\theta_0,\phi_0)\,(n_{\mathrm{w}})^2\,\tau(\theta_0,\phi_0 \rightarrow {\theta_0}',{\phi_0}')\rho(\theta_1,\phi_1 \rightarrow {\theta_1}',{\phi_1}') \\ & \exp\left[-a_{\mathrm{w}}({d_1}+{d_1}')\right]\cos\left|{\theta_0}'-\xi_0\right|\cos\left|\theta_1-\xi_1\right|\cos\left|{\theta_1}'-\xi_1\right| \\ & \cos\left|\theta_{\mathrm{u}1}-\xi_{\mathrm{w}1}\right|\, d\Omega_0\, d\Omega_1\ . \end{aligned} \tag{2.14}$$

### 2.4.3 Second order reflection

From Eq. 2.10, we have the radiance incident once more on the bottom surface from points **1** to **2** (interreflected) with normal $\xi_2$ in the direction $(\theta_2, \phi_2)$ as

$$L(\theta_2, \phi_2) = L(\theta_1{''}, \phi_1{''}) \exp(-a_{\mathrm{w}} d_1{''}) \cos\left|\theta_2 - \xi_2\right| , \tag{2.15}$$

where

$$d_1{''} = \frac{\left|\zeta_1 - \zeta_2\right|}{\sin\left(0.5\left|\theta_1{''} - \theta_2\right|\right)} \tag{2.16}$$

is the interreflection path length. The radiance from an area on the bottom in the direction $(\theta_2{'}, \phi_2{'})$ can be written as

$$L(\theta_2{'}, \phi_2{'}) = \int_{\Omega_2} L(\theta_2, \phi_2)\ \rho(\theta_2, \phi_2 \rightarrow \theta_2{'}, \phi_2{'}) \cos\left|\theta_2{'} - \xi_2\right|\ d\Omega_2 . \tag{2.17}$$

Now the radiance in the direction $(\theta_{\mathrm{u2}}, \phi_{\mathrm{u2}})$ incident at a point **w2** with normal $\xi_{\mathrm{w2}}$ on the water surface from the bottom is

$$L(\theta_{\mathrm{u2}}, \phi_{\mathrm{u2}}) = L(\theta_2{'}, \phi_2{'}) \exp(-a_{\mathrm{w}} d_2{'}) \cos\left|\theta_{\mathrm{u2}} - \xi_{\mathrm{w2}}\right| , \tag{2.18}$$

where the distance from point **2** to **w2** is given by

$$d_2{'} = \frac{z - \zeta_2 + \zeta_{\mathrm{u2}}}{\cos\theta_{\mathrm{u2}}} . \tag{2.19}$$

The radiance transmitted through an area on the water surface is

$$L(\theta_{\mathrm{w2}}, \phi_{\mathrm{w2}}) = \int_{\Omega_{\mathrm{u2}}} L(\theta_{\mathrm{u2}}, \phi_{\mathrm{u2}})\, {n_{\mathrm{w}}}^{-2} \tau(\theta_{\mathrm{u2}}, \phi_{\mathrm{u2}} \rightarrow \theta_{\mathrm{w2}}, \phi_{\mathrm{w2}}) \cos\left|\theta_{\mathrm{w2}} - \xi_{\mathrm{w2}}\right|\ d\Omega_{\mathrm{u2}} . \tag{2.20}$$

Focusing on the radiance detected just below the water surface, we expand from Eq. 2.18 using the preceding relevant expressions so that the twice-reflected radiance at a point just below the water surface expressed in terms of the incident solar radiance is given by (compare this to the first order value in Eq. 2.14):

$$L(\theta_{\mathrm{u2}}, \phi_{\mathrm{u2}}) = \int_{\Omega_2} L(\theta_2, \phi_2)\ \rho(\theta_2, \phi_2 \rightarrow \theta_2{'}, \phi_2{'}) \exp(-a_{\mathrm{w}} d_2{'}) \cos\left|\theta_2{'} - \xi_2\right|$$

$$
\begin{aligned}
&\cos\left|\theta_{\mathrm{u}2}-\xi_{\mathrm{w}2}\right|\, d\Omega_2 \\
&=\int_{\Omega_2}\int_{\Omega_1}\int_{\Omega_0} L(\theta_0,\phi_0)\,(n_{\mathrm{w}})^2\,\tau(\theta_0,\phi_0\rightarrow\theta_0{}',\phi_0{}') \\
&\rho(\theta_1,\phi_1\rightarrow\theta_1{}'',\phi_1{}'')\;\rho(\theta_2,\phi_2\rightarrow\theta_2{}',\phi_2{}') \\
&\exp\left[-a_{\mathrm{w}}(d_1+d_1{}''+d_2{}')\right]\cos\left|\theta_0{}'-\xi_0\right|\cos\left|\theta_1-\xi_1\right| \\
&\cos\left|\theta_1{}''-\xi_1\right|\cos\left|\theta_2-\xi_2\right|\cos\left|\theta_2{}'-\xi_2\right| \\
&\cos\left|\theta_{\mathrm{u}2}-\xi_{\mathrm{w}2}\right|\, d\Omega_0\; d\Omega_1\; d\Omega_2\;. \qquad (2.21)
\end{aligned}
$$

### 2.4.4 Higher order reflection

For higher order reflections $n \geq 2$, we use the convention above to illustrate the incorporation of an arbitrary radiance reflectance function, which gives the radiance finally at the detector below the water surface,

$$
\begin{aligned}
L(\theta_{\mathrm{u}n},\phi_{\mathrm{u}n}) = &\int_{\Omega_{\mathrm{n}}}\cdots\int_{\Omega_1} L(\theta_0,\phi_0)\,(n_{\mathrm{w}})^2\,\tau(\theta_0,\phi_0\rightarrow\theta_0{}',\phi_0{}') \\
&\left[\prod_{i=1}^{n-1}\rho(\theta_i,\phi_i\rightarrow\theta_i{}'',\phi_i{}'')\right]\rho(\theta_n,\phi_n\rightarrow\theta_n{}',\phi_n{}') \\
&\exp\left[-a_{\mathrm{w}}(d_1+\sum_{i=1}^{n-1}d_i{}''+d_n{}')\right]\cos\left|\theta_0{}'-\xi_0\right| \\
&\left[\prod_{i=1}^{n}\cos\left|\theta_i-\xi_i\right|\right]\left[\prod_{i=1}^{n-1}\cos\left|\theta_i{}''-\xi_i\right|\right]\cos\left|\theta_n{}'-\xi_n\right| \\
&\cos\left|\theta_{\mathrm{u}n}-\xi_{\mathrm{w}n}\right| d\Omega_1\cdots d\Omega_n \quad (\forall\;\theta_1<\max\left|\xi\right|)\;. \qquad (2.22)
\end{aligned}
$$

where now extending,

$$
d_1=\frac{z-\zeta_0+\zeta_1}{\cos\theta_1}\;, \qquad (2.23)
$$

$$
d_i{}''=\frac{\left|\zeta_i-\zeta_{i+1}\right|}{\sin\left(0.5\left|\theta_i{}''-\theta_{i+1}\right|\right)}\;, \qquad (2.24)
$$

and

$$d_n{}' = \frac{z - \zeta_n + \zeta_{\mathrm{u}n}}{\cos\theta_{\mathrm{u}n}} \ . \tag{2.25}$$

We can simply replace the radiance reflectance function, $\rho$, with a bi-directional reflectance distribution function (BRDF) in Eq. 2.14 above, to get the first order reflected radiance just below the water surface. A similar replacement is now possible in Eq. 2.21 for reflections of order $n \geq 2$ as well. We take the definition of the BRDF from Nicodemus et al. (1977) and further on from notes in a discussion by Mobley & Mazel (1999), from Otremba (2003), as well as a review by Martonchik et al. (2000). Note that in remote sensing applications investigators refer to the remote sensing reflectance that is usually represented by

$$R_{\mathrm{RS}} = \frac{L_{\mathrm{u}i}(\lambda)}{E_{\mathrm{s}}(\lambda)} \, [\mathrm{sr}^{-1}] \ , \tag{2.26}$$

which is the ratio between upwelling radiance and downwelling irradiance. The BRDF is a similar concept except that the irradiance is treated as being directional, so that the BRDF is a function of a pair of angles, the incident angle and one of the emergent angles, denoted by $(\theta_0, \phi_0)$ and $(\theta_0{}', \phi_0{}')$ respectively, thus the term "bidirectional".

## 2.5 Shadowing, obscuration and geometric focusing

Shadowing refers here to shadows that are cast by one part of the bottom waveform on another part, a phenomenon which Oren & Nayar (1995) call self-shadowing. This occurs in the first order when the bottom incidence angle is greater than the maximum normal found along the bottom waveform, i.e., $|\theta_1| > \max|\xi|$, see Fig. 2.3(a) (the shaded areas indicate the affected regions). For the second order, shadowing occurs when the emergent beams from a point only directly illuminate

areas bounded by the relative curvature of the waveform, Fig. 2.3(b) (the shaded area on the right is an example of "projected" shadowing, see Hapke 1993). Note that for a single viewing direction there is only one first order reflection for each initial incidence at each point along the bottom while interreflections toward that point produce multiple second order reflections toward the same viewing direction.

Obscuration occurs when one of the return directions grazes the bottom waveform or when the return directions are blocked by other parts of the waveform, so that the detector does not "see" sections of the bottom surface. The grazing angle depends on the relative position of the detector with respect to the bottom, for example, in Fig. 2.5. Torrance & Sparrow (1967) refer to this phenomenon as masking; although another type of obscuration is when a facet is tilted away from the detector (i.e., $|\xi_i - \theta_d| \geq \pi/2$, where $\theta_d$ is the angle the detector normal makes to the global normal). While these phenomena of shadowing and obscuration are similar, their effects on the overall expected reflectance cannot be expected to be the same, nor can they be treated as invariant.

A shadowed area may be illuminated by higher order reflections and therefore these contribute to the overall reflectance. To illustrate, consider an illuminated point with radiance $L_1$ and its interreflections, Fig. 2.6(a). An arbitrary interreflection $L_1''$ from an illuminated area onto a part of another area that is shadowed in Fig. 2.6(a) contributes a value $L_2$ to the overall surface reflectance. Similarly, a point that is in the region obscured from the detector, shown in Fig. 2.6(b), directly illuminated with $L_1$ may produce interreflections $L_1''$ contributing $L_2$ to the overall reflectance of the bottom. It is evident that these phenomena are dependent on the relative geometry of the bottom.

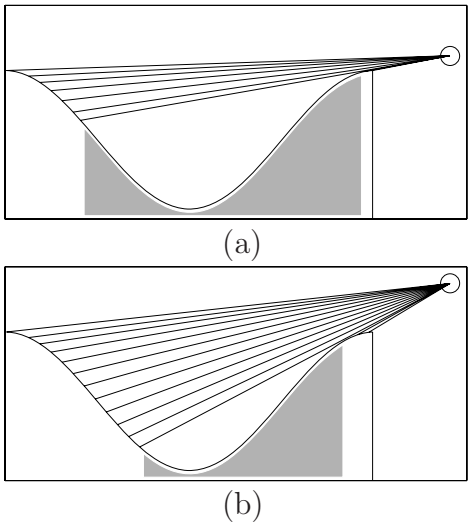


Figure 2.5: Obscuration occurs when parts of the bottom waveform are hidden from the detector. The relative position of the detector determines the obscured areas; (a) and (b) show two different viewing situations.

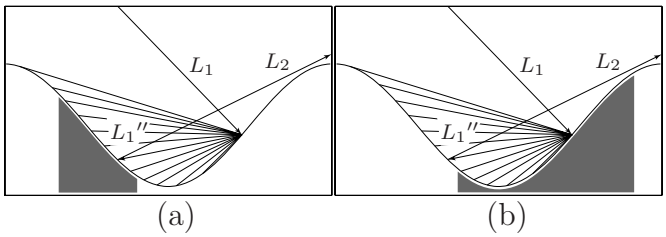


Figure 2.6: The effects of shadowing and obscuration on the overall reflectance are not exactly the same. (a) shows a shadowed area with no first order reflections, $L_1$, but which nonetheless contributes $L_2$ to the overall reflectance from interreflections $L_1''$. On the other hand, in (b) an area that is illuminated in the first order but obscured from direct view contributes to overall reflectance via its interreflections.

The effects of shadowing and obscuration change gradually as the roughness changes on a smooth surface such as a sinusoid, while they would be abrupt on surfaces modeled as macro-facets, such as a triangular wave. Take two simple surfaces with the same amplitude-to-period ratios: Fig. 2.4(a) shows a sinusoid and Fig. 2.4(b) shows a triangular wave. Say we have an incidence direction, $|\theta_a|$, less than the maximum normal of the sinusoidal bottom, $\max|\xi|$. All the facets are directly illuminated, both for the sinusoidal and the triangular bottom. On the other hand, observe that the grazing angle of a triangular wave, $\theta_b$, is greater than the maximum slope of the sinusoid, $|\theta_b| > \max|\xi|$, in Fig. 2.4(a). At this grazing angle and for greater angles of illumination, half if not more of the triangular wave in Fig. 2.4(b) is suddenly shadowed while shadowing increases more gradually for parts of the sinusoid. This illustrates the abruptness of the phenomenon on the triangular wave but also highlights the subtleties that result from a continuously differentiable model. Furthermore, for incidence directions, $\theta_c$, greater than the maximum normal of a sinusoid but less than the grazing angle of the triangular wave, a sinusoid may be shadowed while the triangular wave is still fully and directly illuminated (Fig. 2.4(b)).

Similarly, half or more of the triangular wave is abruptly hidden when the viewing angle is equal to or greater than its grazing angle, $\theta_d$, while different parts of the sinusoid are obscured for the same angle in Fig. 2.7 (the shading indicates obscured areas). Also, for an angle $\theta_e$ greater than the maximum slope of a sinusoid but less than the grazing angle of a triangular bottom, part of the sinusoid is hidden while the triangular wave would be in full view.

Another interesting geometrical feature is the way light is redistributed into seemingly preferential directions by an undulating surface that is locally Lamber-

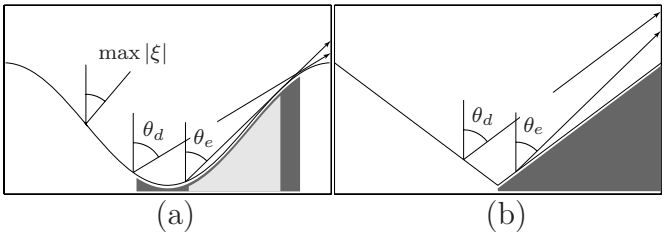


Figure 2.7: Obscuration effects differ between sinusoidal and triangular bottom models. Consider viewing directions from any point along the surface. For an angle $\theta_d$ that is equal to the grazing angle of the triangular wave, half of that surface is obscured while only part of the sinusoid is hidden. For a viewing angle $\theta_e$ less than that grazing angle, no part of the triangular wave is obscured while part of the sinusoid is still hidden from the detector FOV.

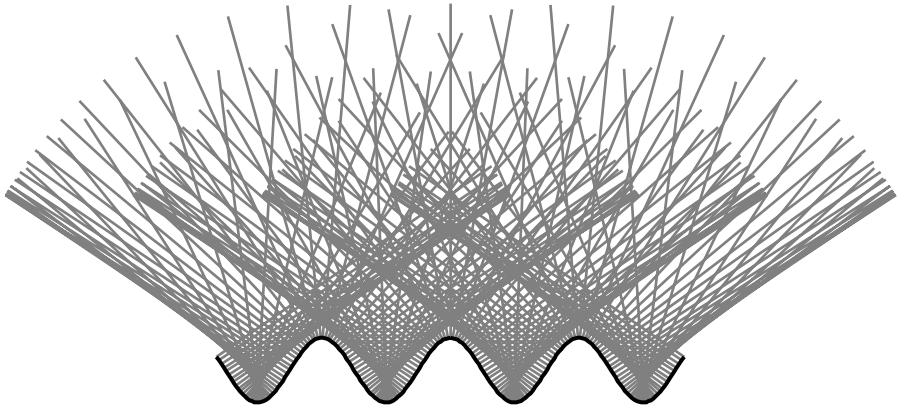

Figure 2.8: Diagram illustrating geometric focusing.

tian. Light that is incident on a point on the surface has the highest reflectance in the direction normal to the surface tangent at that point. In Fig. 2.8 is shown the local normals at select points along a two-dimensional surface. The lines are drawn to be of equal length to represent equal intensities at the end points of the light emerging from the surface. The preferential direction changes with a change in the amplitude-to-period ratio of the defining waveform. A detector looking straight down does not see this effect.

## 2.6 Realization using an actual sensor

> Were the eye not attuned to the Sun,
> The sun could never be seen by it.
>
> *Goethe*

To illustrate the changes in reflectance, we use the optical properties of a specific instrument, the HyperTSRB (see Satlantic, Inc. 2000), as an example. This instrument is designed to collect upwelling, near-surface radiance in water. It has a rectangular entrance slit with a width-to-length ratio of 0.028 (70mm/2500mm) and a half-angle of 8.5°. The instrument is deployed as a buoy and the input optics positioned below the water surface at a depth of $z' = 0.66$m (see Fig. 2.9). This defines the detector reference plane, $z_0$, the distance to the bottom reference plane, $\nu$, and the projected surface area of the bottom, $A_s\,[\mathrm{m}^2]$. The projected surface area of the bottom is taken at a level just above the highest point of the surface (i.e., at crest level). For computational purposes, a horizontal reference surface is used to keep track of points along the bottom. The reference surface is divided into equally spaced points representing areas with the bottom surface projected onto it, the centroids of these areas act as reference points. The maximum in-water incidence angle is limited to within Snell's cone, in this case, $|\theta_1| \lesssim 48°$ and has a more distinct boundary when the water surface is flat). The corresponding above-water incidence angles span the full angular range within the solar plane and are determined from the in-water incidence angles. We trace backward to the source to assign the incoming uni-directional solar irradiance. Recall that the detector reference plane in the model, $\mathbf{W}$, is just below the lowest point of the water surface perpendicular to the global vertical (Fig. 2.1). In this implementation, however,

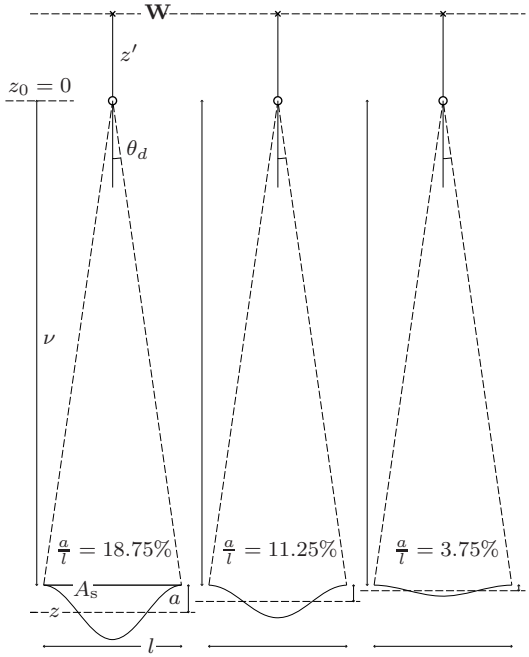


Figure 2.9: Specific setup for the HyperTSRB. Keeping the bottom waveform period, $l$, constant, and changing the amplitude, $a$, adjusts the $a/l$ ratio. This keeps the projected area, $A_s$, constant as viewed by the detector at a fixed depth, $\nu$. The reference plane for the water surface is **W**, the detector is at $z_0 = 0$, and the bottom is at $z$. Only the average bottom depth, $z$, is variable. The HyperTSRB has a viewing half-angle of $\theta_d = 8.5°$. The $a/l$ ratios given in the figure are three of the actual dimensions used in the modeling and are here drawn to scale.

we assume that the water surface, **S**, is flat and fix the detector reference plane at $z_0 = 0$m (still theoretically submerged) and the illumination plane at $z' = -0.66$m.

With this setup the detector views only one single waveform from crest to crest. Viewing a single waveform simplifies the comparison of changes in reflectance due to changes in the shape of the bottom surface. Depending on the amplitude-to-period ratios considered, the average depth of the bottom surface, $z$, is shallower for less rough bottom waveforms. The detector is positioned directly above the center of the bottom waveform and its viewing angle is held at nadir ($\theta_{ui} = 0°$). The

bottom incidence angles of the light transmitted through the air-water interface are also limited to $|\theta_0'| \lesssim 48^\circ$ (occurring only in the solar plane, i.e., $\phi = \phi_0$ or $\phi_0 + \pi$). In the actual modeling the amplitude-to-period ratio, $a/l$, of the bottom waveform varies from 0 to 0.225, while the period is kept constant at $l = 1.1$m.

Although the notation of wavelength dependence is omitted in the analytic expressions above, we wish to explore the spectral changes that are caused by varying bottom morphology. The wavelength range considered is between 400–750nm. For the input directional downwelling irradiance, we assume an air mass of 1.5 (dimensionless) using ISO standard tables (ISO 1992), the water absorption coefficients for each wavelength is taken by Smith & Baker (1981), and the spectral reflectances of sand, shown in Fig. 2.10, are from measurements made in the Bahamas by Louchard et al. (2003) and those used by Mobley (2006) in his model Hydrolight. The original sand spectrum has a chlorophyll-$a$ absorption feature centered at 685nm in a region that would be dominated by water absorption. An artificial absorption feature was added, centered at 500nm in order to more effectively track effects due solely to the bottom.

Given the transmitted directions $|\theta_0'| \lesssim 48^\circ$, Snell's law (*ceteris paribus*) gives the incident directions in air as

$$\theta_0 = \sin^{-1}\left(\frac{n_\mathrm{a}}{n_\mathrm{w}} \sin {\theta_0}'\right) \ . \tag{2.27}$$

Similarly, the viewing angles in air are

$$\theta_{\mathrm{w}i} = \sin^{-1}\left(\frac{n_\mathrm{w}}{n_\mathrm{a}} \sin \theta_{\mathrm{u}i}\right) \ . \tag{2.28}$$

The transmittance of the air-water surface from any incident direction is based on Fresnel's equations (see, e.g., Sears 1949), which for randomly polarized incident

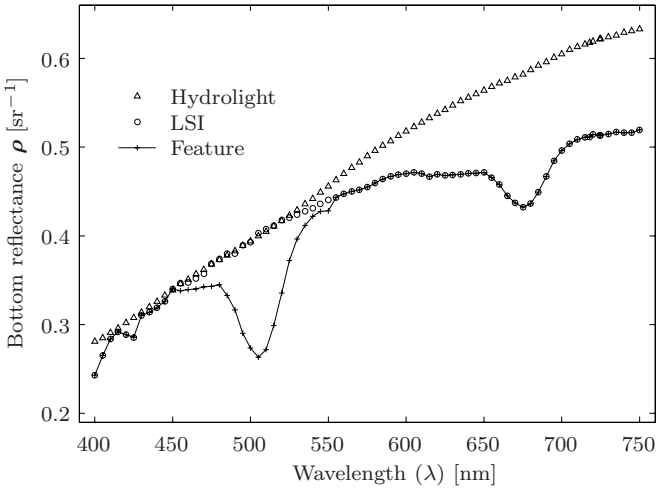


Figure 2.10: Different sand reflectances used in various studies. Reflectance of sand used in Hydrolight and that measured from a core sample during CoBOP field work off Lee Stocking Island (LSI), with an added artificial spectral feature between 450–550nm, are shown in the plot.

light is:

$$\tau(\theta_i \rightarrow \theta_i') = 1 - \left\{ 0.5 \left[ \frac{\sin(\theta_i - \theta_i')}{\sin(\theta_i + \theta_i')} \right]^2 + 0.5 \left[ \frac{\tan(\theta_i - \theta_i')}{\tan(\theta_i + \theta_i')} \right]^2 \right\} . \tag{2.29}$$

We show that the limit of this transmission function exists in a proof given in Appendix C.1. The transmission directions are independent of azimuth angle, so the representation of azimuthal dependence is omitted here. Planar facets are idealized from the normals of the reference points along the bottom surface. Given the relative scale of the surface with its depth, we can safely assume that the spectral wavelengths considered are much smaller than the surface facets so that

$$\lambda^2 \ll a_{sj} \ll A_s \ , \tag{2.30}$$

where $a_{sj}$ [m$^2$] is the area of facet $j$. For each of the facets, the impinging radiance is determined by the backward tracing already mentioned earlier in this section. From each of the facets, interreflections from the primary reflections make their

way to other facets on the bottom. The combined secondary reflections from each bottom facet then find their way to the detector and contribute to the final perceived brightness.

The process imagined here is similar to the approach used by Hapke (1993). However, we bring it further by taking into account the reflectance of the surface, the absorption in the underwater light field along the ray paths, and the relative directions of the incident and emergent paths with respect to the facet normals. Note that, for this simple case, the detector is looking straight down. With the bottom surface area discretized, the light from each planar facet can be added to simulate what a realistic detector would perceive.

While multiple scattering within a waveform can be studied using a triangular wave, the effect of shadowing and obscuration are too abrupt when grazing incidence conditions are in effect. Before we go any further, we mention that a theoretical approach taken by Zaneveld & Boss (2003) (ignoring attenuation) provides an expression for radiances emerging from an underwater bottom surface modeled as a triangular wave for $i$ reflections and $j$ facets:

$$L_{\mathrm{TSRB}}(\theta_{\mathrm{u}i}, \phi_{\mathrm{u}i}) = \sum_{a_{\mathrm{s}j} \in A_{\mathrm{s}}} \frac{L(\theta_{ij}{}', \phi_{ij}{}')\ (d)^2\ a_{\mathrm{s}j} \cos\left|\theta_{ij}{}' - \xi_{ij}\right| \cos\left|\theta_{\mathrm{u}ij} - \xi_{\mathrm{u}i}\right|}{(d_{ij}{}')^2 A_{\mathrm{s}} \cos\theta_{\mathrm{w}} \cos\theta_{\mathrm{s}}} \ , \quad (2.31)$$

where

$$d = z - \max\left|\zeta_{ij}\right| - \min\left|\zeta_{\mathrm{u}i}\right| - z' \ , \quad (2.32)$$

$\theta_{\mathrm{w}}$ is the detector viewing angle, and $\theta_{\mathrm{s}}$ is the normal of the bottom projected surface with area $A_{\mathrm{s}}$. The water surface is assumed to be flat and the average bottom surface is perpendicular to the global normal so that $\cos\theta_{\mathrm{w}} = \cos\theta_{\mathrm{s}} = 1$.

Notice that if shadowing exists it is accounted for by the condition imposed in Eqs. 2.7 and 2.22 for radiances just leaving the surface facets, while any facet for

which obscuration is in effect would be eliminated by the limit in the summation ($a_{sj} \in A_s$) in Eq. 2.31. Due to the geometric setup of the bottom used by Zaneveld & Boss (2003), the detected radiance expression is further simplified by assuming that the angular terms approach unity and that the difference between the average distance from the projected bottom to the detector and that of each facet to the detector is negligible. We suspect, however, that the angular terms and the distances light travels in the medium can be brought to bear in a sinusoidal model and use these same concepts to highlight the geometric effects of our model. Furthermore, in our model each of the rays from the facets is attenuated through the path length of light as incorporated in the radiance function, $L(\theta_{ij}', \phi_{ij}')$, for all reflections $i$ and facets $j$, that is given in Eqs. 2.10 or 2.17.

## 2.7 Spectral considerations for marine optics

Bottom roughness can affect both the magnitude and spectral quality of the observed reflectance. In order to understand how spectral changes may arise from higher order reflections due to multiple interactions of the light with the bottom, initial results for first and second order reflectance are presented separately. The first order reflectance is indicative of the overall change in magnitude as the bottom roughness changes, while the second order reflectance should be more sensitive to changes in the spectral distribution.

### 2.7.1 Changes in magnitude

We consider only first order and second order reflections from an underwater sinusoidal surface at wavelength $\lambda = 550$nm. Assuming that the water surface is flat and there are no other light sources in the medium, the rays of interest fall

within Snell's cone ($\theta_1 \lesssim 48^\circ$ underwater incidence angles, $0^\circ$ being zenith incidence). For a flat bottom, where $a/l = 0$, the first order radiance decrease behaves Lambertian-like (Fig. 2.11), with a falloff proportional to the cosine of the incidence angle. Because the situation is in the near-field, the redistributed emergent directions contribute to an overall non-Lambertian effect. As roughness increases, the zenith return radiances drop, implying that the radiance has been redirected into other directions, making the reflectance less Lambertian. When the surface becomes sufficiently rough the radiance drops abruptly (e.g., the drop between $a/l = 0.24$ and 0.3 for an incidence angle of $30^\circ$), and with increasing roughness this abrupt drop occurs at smaller incidence angles. This is due to the effects of either shadowing or obscuration, or both. (Note that the curves in the figure are not smooth due to the wide sampling intervals taken for the roughness ratio.) Although the underlying surface reflectance is essentially Lambertian, the effects of roughness on the overall return quickly alters the distribution of reflected light. Interestingly enough, however, the decrease in radiance relative to a flat surface is the same regardless of incidence angle except when shadowing or obscuration takes place, then the subsequent decrease is the same. For the setup here, and as expected we conclude that: (1) the brightest surface is a flat surface; and, (2) when the roughness increases, the brightest overall return from primary reflections is at an incidence angle parallel to the zenith direction.

There are no secondary reflections from a flat surface (Fig. 2.12). The second order radiances initially increase and eventually decrease as roughness sets in. Changing the amplitude-to-period ratio of a surface changes the incidence angle at which the surface produces its greatest second order reflectance. As the roughness increases the radiances peak at this maximum ratio and then begin to decrease.

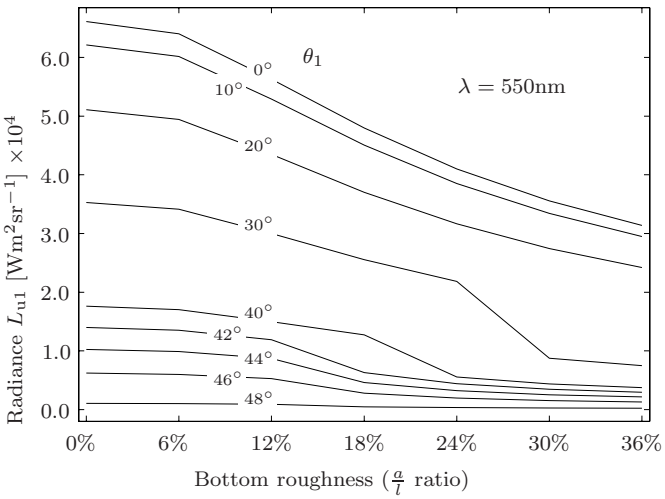


Figure 2.11: First order radiances at $\lambda = 550$nm as the $a/l$ ratio increases, for different incidence directions, $\theta_1$, but with a fixed viewing direction at $\theta_u = 0°$. In the first order, the reflectance is highest when the surface is flat and decreases as the surface becomes rougher. An abrupt drop is observed when the bottom roughness causes either shadowing or obscuration, or both.

As with the first order radiances, a more pronounced decrease is expected when the effects of either shadowing or obscuration, or both, set in. At its maximum (at $a/l = 0.12$ for this viewing distance) second order radiance is only about 2% of the first order radiance and is nearly constant for any viewing angle. Recall that only the diffuse component of the secondary reflections have been considered. The contribution of the second order is greatest at some intermediate roughness where focusing occurs (see also Ivanov & Prikhach 1976). The brightest secondary reflections come from a surface that has an amplitude-to-period ratio of $a/l = 0.12$ but similar to first order radiances regardless of roughness. The brightest overall return results when the light source is at zenith. Even so, the contribution of the second order reflections are small—almost two orders of magnitude smaller—relative to the overall reflected radiance.

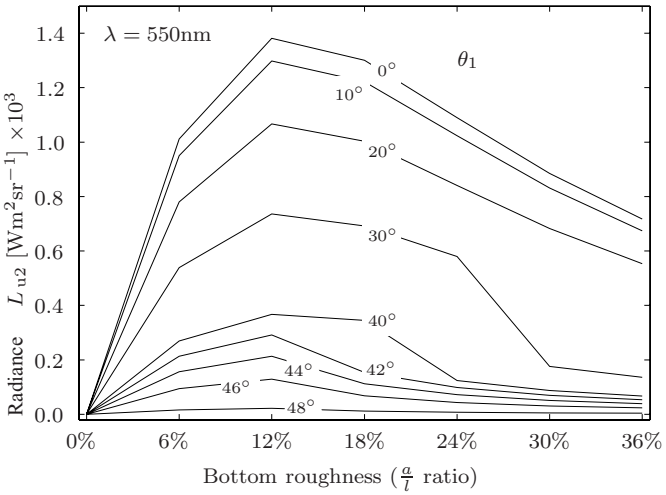


Figure 2.12: Second order radiances at $\lambda = 550$nm as the $a/l$ ratio increases, with incidence directions, $\theta_1$, matching those in Fig. 2.11, and with a fixed viewing direction, $\theta_u = 0°$. There are no second order reflections when the surface is flat. Again, either shadowing or obscuration, or both, cause a sudden drop in the reflectances when the surface becomes rough enough.

### 2.7.2 Spectral effects

For the following discussion the bottom reflectance is modeled using the reflectance measurements for sand collected off Lee Stocking Island (LSI) in the Bahamas, with a strong, but artificial, spectral absorption feature added that is centered near $\lambda = 500$nm. The composite spectral reflectance is shown in Fig. 2.10. We ask, therefore, what are the spectral changes that may be expected when a surface changes from being flat? Using a bottom surface reflectance that is different from a Hydrolight curve (Fig. 2.10), and incorporating both the LSI and the arbitrary feature introduced here we find that the spectral reflectance is remarkably insensitive to the surface roughness (Fig. 2.13). Normalizing the spectral reflectance for all roughness values considered (Fig. 2.14), it is apparent that the bulk of the rather subtle change in the spectra seem to have little to do with bottom reflectance and

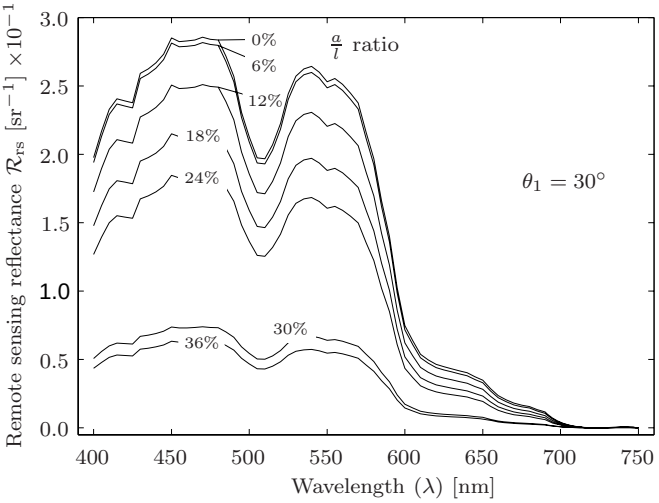


Figure 2.13: Effects on the remote sensing reflectance. The spectral remote sensing reflectance, $R_{\mathrm{RS}}$, is given here from the total upwelling spectral radiance (at the detector below the water surface) over downwelling irradiance (just above the water surface) for a bottom incidence direction of $\theta_1 = 30°$ and a viewing direction $\theta_{\mathrm{u}} = 0°$, considering transmission and attenuation effects as well as the wavelength-dependent reflectance of a sandy bottom.

can be explained almost entirely by the increase in absorption by water due to the increase in the effective optical path lengths as the roughness increases. Even the strong absorption feature inserted into the bottom reflectance spectrum failed to induce significant effects as the roughness increased.

## 2.8 Summary

The change in reflectance of an undulating underwater surface that is locally Lambertian has been modeled. The model, formulated to be very general, includes first and second order reflectances and is designed to include shadowing and obscuration effects. Results for the specific case of a nadir-viewing detector indicate that the first order reflectance decreases significantly as the amplitude of the bottom

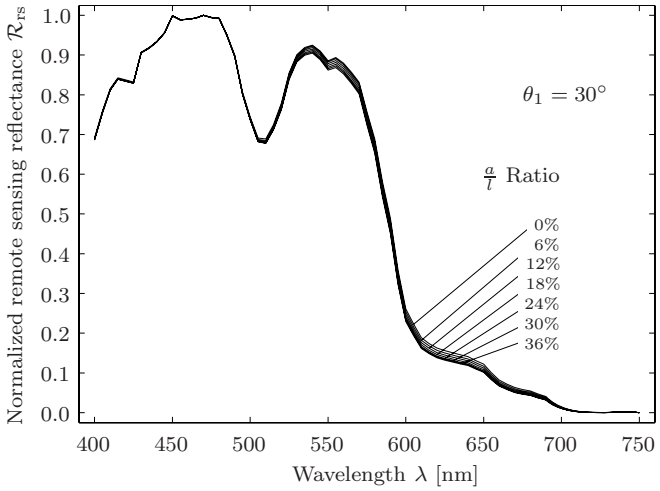


Figure 2.14: Normalized first order radiances across wavelengths. The small change in "color" is driven by an increase in water absorption as the path lengths in the water increase, although the difference as the roughness changes is almost insignificant. Note that there is almost no change in the artificial absorption feature near 500nm.

waveform increases. The change in the overall reflectance is only slightly altered due to the increasing contributions from second order reflections with increasing roughness.

The modeled conditions considered here are simple, but serve to illustrate the general problem. There are many issues to consider, however. For the near-field case presented here (a variation of the far-field case is left for the next chapter), the second order reflections were only as high as 2.5% of the first-order reflectance and its overall effect on the spectral reflectance is marginal even where water absorption is weakest. Given the assumptions made on the reflectance of the surface and the absorption in the water, there is very little spectral difference coming from the change in roughness except for a decrease in the overall reflectance across all wavelengths. It is possible that spectral reflectance factors would play a more significant role in extremely rough surfaces (e.g., corals, seagrass beds) where

radiance from multiple reflections becomes more significant, but such cases are not addressed here.

As described, the model here is capable of handling any degree of surface roughness, provided that it can be represented as a single-valued function (i.e., there are no overhangs or cavities along the bottom surface; discontinuous derivatives are inadmissible). While definitions of roughness abound, we simply use the amplitude-to-period ratio of the defining sinusoidal function of the surface as a roughness metric.

We have shown that geometrical effects, more than anything else, contribute to the non-Lambertian behavior of the resulting reflectance of a rough surface. However, the model setup is restricted in the sense that all the light captured by the FOV of the imaging system at any one time arises from a single surface waveform, irrespective of the surface roughness. This restriction provides a convenient basis for comparing surfaces with different roughness ratios. In general this need not be the case, and it becomes necessary to allow for multiple waveforms in order to consider multiple viewing angles. Finally, while the results here only include contributions up to second order reflections, but with shadowing and obscuration effects, the analytical expression presented is written for the $n$th order.

CHAPTER 3

# PART II. ESTIMATION OF THE VARIABILITY IN THE REFLECTANCE OF A THREE-DIMENSIONAL ROUGH SURFACE

## 3.1 Introduction

The two-dimensional geometrical model presented by Zaneveld & Boss (2003) was useful for describing the range of variability in reflected radiation due to roughness. However, a full three-dimensional model is needed to examine the effect of bottom morphology and the implications for remote sensing since actual observations are rarely confined to the solar plane. Thus, the two-dimensional model of Zaneveld & Boss (2003) is extended here into three dimensions using a periodic surface to show changes in reflectance that might be expected for near-field and far-field remote sensing. Using a simple periodic surface function, the derivation that follows offers an approach that is applicable for any locally Lambertian surface that can be expressed as a single-valued function (see Koenderink et al. 1999 for "pitted" surfaces that affect its apparent texture) . The analysis results in a far-field "correction" factor for a three-dimensional surface that is analogous to that found by Zaneveld & Boss (2003).

## 3.2 Objective and assumptions

For this brief exposition, we want to derive an effective reflectance function as a substitute for the usual Lambertian assumption using a three-dimensional egg-carton (sinusoidal) surface. Oren & Nayar (1995) provide a solution to reflectance change by a locally Lambertian surface due to roughness that agrees well with their measurements. Viewing straight on, they suggest that as surface roughness

decreases, the apparent surface reflectance approaches that of a flat surface. We show, however, that it approaches a "far-field" value that is the ratio of the effective reflectance and the inherent Lambertian reflectance (so do Zaneveld & Boss 2003 for a two-dimensional triangular wave). Their model includes isotropic and anisotropic surface roughnesses. The simplification made here to a surface that has an underlying sinusoidal function imposes a directionality to the surface roughness. The importance of the sinusoid as a model for rough surfaces in providing analytical solutions is discussed in, for example, Millar (1973) and Waterman (1975) (for light waves incident on a surface) and references therein; in particular, Lord Rayleigh (1910) finds that either the amplitude or the period of the surface affects the effective reflectance of a rough surface. While a surface function may be described statistically (e.g., Bass & Fuks 1979, Beckmann & Spizzichino 1987), an analytical function allows for the simplicity in deriving the generalized integral equation. Another simplifying assumption is that the roughness dimensions of the surface in question is much larger than the incident wavelength of light. This way, the theory of geometric optics applies and we can treat the light being transferred in the system as rays and ignore interference effects. For a similar treatment of periodic structures with amplitude and period in transverse and electromagnetic waves see Zaki & Neureuther (1971a,b). They find that the power of the specularly reflected wave from a rough surface at normal incidence is equal in amplitude to that of a flat surface (Zaki & Neureuther 1971a). They also find that as surface roughness increases, the reflectance drops for any given incidence angle. Furthermore, they observe, at least for light treated as waves, that a Brewster angle effect occurs for a particular amplitude-to-period ratio relative to wavelength.

For our purpose here, we assume that measurements are taken at scales where the roughness dimension could be smaller than or larger than the width of the detector footprint. Fig. 3.1 shows an idealization of a detector FOV over a rippled surface, one closer and one farther from the surface viewing straight down. In any case, the detector height is constrained so that its footprint sees at least one full ripple. With a detector viewing along nadir (i.e., straight down), the reflectance of the surface is at its maximum and no shadowing nor any obscuration can occur (increased effects due to shadowing occur when the light is treated as waves, see Zaki & Neureuther 1971b). Multiple reflections from the surface are ignored. Furthermore, we assume that the light source is assumed to be at zenith.

## 3.3 Defining reflectance

Radiance is defined as the intensity of light emerging from or incident onto a surface at certain directions per unit solid angle (Watts per unit area per unit steradian). Irradiance, on the other hand, is light that is incident onto a surface from *all* directions and emergent into *all* directions (Watts per unit area). A steradian is the area *subtended* by the source or projected onto the receiver along the path of light propagation. It is, in fact, a three-dimension angular measure (see Part I). If the light from a source of finite area can be measured in all its emanating directions (a full hemisphere for an infinitesimally small area), then the quantity measured is irradiance. Further nuances to these concepts and other assumptions are added as needed.

In general, because a surface has inherent optical properties, an efficient way to deduce these properties is to study the reflectance of a surface in different directions and with different wavelengths of light. Reflectance then is just the ratio of the

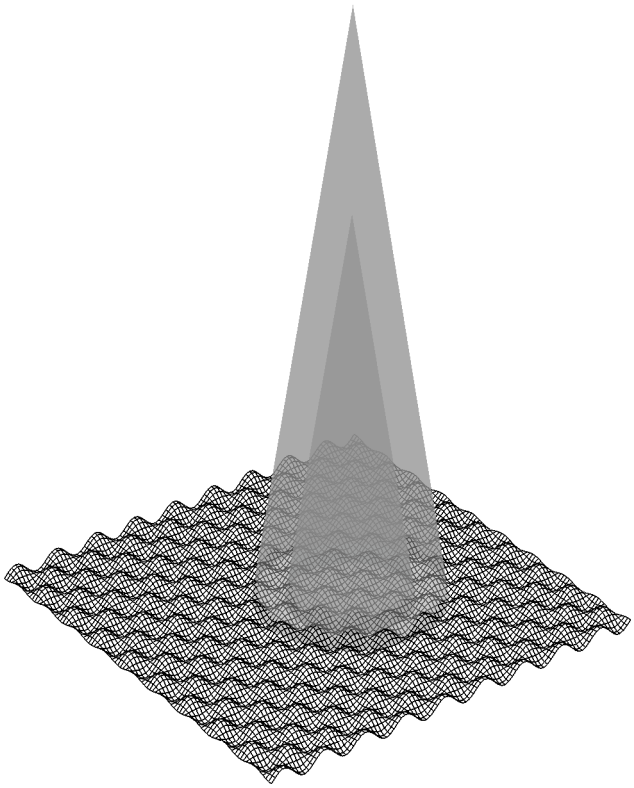

Figure 3.1: Moving the view from the near-field to the far-field case. With the field of view of a detector remaining constant but the detector moving farther away from the surface, its footprint increases and includes reflectance effects from more parts of the extended surface.

amount of light leaving a surface to the amount it receives. For remote sensing purposes, since the usual available light in the natural environment comes from the sun and skylight, the incoming radiation is measured as irradiance: the light available to a surface of interest. The light leaving a surface, for practical purposes, is measured only from one particular direction in the given hemisphere above this surface. So, reflectance is thus a ratio of radiance over irradiance and carries units per steradian. In the rest of the discussion for this part, the units of SI are utilized.

Now, more formally, the radiance *at* a surface $L\left[\mathrm{Wm^2sr^{-1}}\right]$ is defined as the radiant flux $\Phi\,[\mathrm{W}]$ per unit projected surface area per unit solid angle $\Omega\,[\mathrm{sr}]$ (compare to previous definition in Eq. 1.3). By the principle of reciprocity, the radiance at the detector is equal to the radiance at the surface

$$L = \frac{\Phi}{A_s \cos\theta_s \Omega_s} = \frac{\Phi}{A_d \cos\theta_d \Omega_d}\ , \tag{3.1}$$

where

$$\Omega_s = \frac{A_d \cos\theta_d}{r^2}\ , \tag{3.2}$$

and

$$\Omega_d = \frac{A_s \cos\theta_s}{r^2}\ , \tag{3.3}$$

and $r$ is the distance between the surface (or source) and the detector. Assuming there is no loss of light or attenuation along the path in the intervening medium, the flux at the source, $\Phi$, is exactly equal to the flux at the detector. This assumption facilitates the isolation of the effect of surface roughness. $\theta_s$ and $\theta_d$ are the angles between zenith and the normals to the surface and the light path, respectively. If we assume that both surface and detector areas are homogeneous, so that any small "patch" might represent the wider surface, then we can assume that the areas of the surface and the detector, $A_s$ and $A_d$, respectively, are infinitesimally

small. Furthermore, say that the surface material is perfectly diffuse, that is, it has the property of reflecting light incident on it equally into all possible emergent directions. The surface is then said to be Lambertian; and if the infinitesimally small areas, or facets, regardless of their tilts, obey this law, the surface can be treated as locally Lambertian. As a simplification, the radiance at a point on this Lambertian surface is defined as

$$L = \rho \frac{E}{\pi} \; . \tag{3.4}$$

$\rho$ is the inherent reflectance coefficient of the surface and $E$ is the irradiance at the surface. In fact, $\rho$ is more formally the irradiance reflectance function (proof provided, for example, in Mobley 1994, p. 234), which is the ratio of the emergent irradiance to the incident irradiance. (For a different expression of diffuse reflectance that uses a Fresnel term to modify the Lambertian equation, see Wolff 1994.) This is the reflectance we want to find a substitute for when the surface is no longer flat. The coefficient provides the measure of the error of assuming that a surface, albeit inherently Lambertian, is flat when it can have a roughness that affects its *apparent* optical property. To be able to separate out the effect of surface roughness—the variation of its tilts away from vertical—we want this "effective" reflectance to be entirely dependent on roughness.

## 3.4 Extending into three dimensions

Let a beam of light be incident at a point on the surface (as represented by a plane facet) in the direction of the *unit* vector $\vec{r}_0$, given in polar coordinates as $(\theta_0, \phi_0)$ or in vector components as

$$\vec{r}_0 = (\sin\theta_0 \cos\phi_0)\ \vec{\mathrm{i}} + (\sin\theta_0 \sin\phi_0)\ \vec{\mathrm{j}} + (\cos\theta_0)\ \vec{\mathrm{k}} \; . \tag{3.5}$$

Furthermore, let the surface be defined as a two-dimensional sinusoid (much like an egg carton) with an amplitude $a$ and a period $l$ referenced on a Cartesian coordinate system. The roughness then can be dependent on a surface shape of this sinusoid:

$$g(x, y) = a \sin kx \cos ky \ , \tag{3.6}$$

where

$$k = \frac{2\pi}{l} \ . \tag{3.7}$$

By the cosine law of irradiance, the irradiance at a point anywhere on the surface produces an irradiance that is proportional to the cosine of the angle between the incident direction and the normal at this point, thus,

$$E = E_s \cos \Big| \, (\theta_0, \phi_0) - (\theta_n, \phi_n) \, \Big| = E_s \left| \vec{r}_0 \cdot \vec{r}_n \right| \ , \tag{3.8}$$

where the polar angle pair $(\theta_n, \phi_n)$ represents the normals to the facets. Recall that $\vec{r}_0 \cdot \vec{r}_n$ is the dot product of the two vectors and gives the angular distance between them. More explicitly, in vector notation, the *unit* normal vectors are expressed as

$$\vec{r}_n = \frac{1}{\sqrt{1 + {g_x}^2 + {g_y}^2}} \left[ (-g_x) \, \vec{\mathrm{i}} + (-g_y) \, \vec{\mathrm{j}} + \vec{\mathrm{k}} \right] \ , \tag{3.9}$$

where

$$g_x = \frac{\partial g}{\partial x} \tag{3.10}$$

and

$$g_y = \frac{\partial g}{\partial y} \tag{3.11}$$

are the partial derivatives of the surface function in the $x$- and $y$-directions, respectively (the fractional factor normalizes the vector to unit length). In fact, the

ratio of the reflectance of a rough Lambertian surface to that of a flat one is simply the average cosine of the facet normals (proof in Hapke 1993).

By definition, the irradiance at a surface is the integral of the radiance on it from all incident directions, taking into account the effect of the cosine of the incidence angle makes for each direction:

$$E_s = \int_{\Omega_0} L(\theta_0, \phi_0) \left| \cos\theta_0 \right| d\Omega_0 \ . \tag{3.12}$$

Translating into Cartesian coordinates (necessary for referencing the location $(x, y)$ of the surface projected onto the $xy$-plane) where $g(x, y) \in S$ and using the normal vectors to express the facet tilts, the irradiance at the surface can be expressed as

$$E_s(x, y) = \int_S L(x, y, \theta_0, \phi_0) \left| \vec{r}_0 \cdot \vec{r}_n \right| dS \ . \tag{3.13}$$

If it can be assumed that the reflected radiance is collimated, then substituting Eq. 3.8 into Eq. 3.4 the radiance of a surface that is not flat can be expressed as

$$L = \rho \frac{E_s}{\pi} \left| \vec{r}_0 \cdot \vec{r}_n \right| \ . \tag{3.14}$$

Recall that $\rho$ is the reflectance coefficient of the material, i.e., it is a property inherent to the surface material that is locally Lambertian at any point. Taking the ratio of the surface radiance to the incident irradiance from Eq. 3.14 gives us an effective reflectance for a Lambertian facet:

$$\rho_{\mathrm{f}} = \frac{L}{E_s} = \rho \left| \vec{r}_0 \cdot \vec{r}_n \right| \ , \tag{3.15}$$

This gives the ratio of the material reflectance to the apparent reflectance as

$$\frac{\rho_{\mathrm{f}}}{\rho} = \left| \vec{r}_0 \cdot \vec{r}_n \right| \ , \tag{3.16}$$

being just the cosine of the tilt angle of the facet with respect to its local normal.

## 3.5 Far-field effects

As the detector moves away from the surface, many more points and thus many more facets fall within the detector field of view. Let the area of this surface be $A_S$. It turns out that reflectance ratio is the average of the cosines of the angles between the incident direction and surface normals. For the far-field case, Eq. 3.16 is integrated over the surface domain to get

$$\frac{\rho_{\text{ff}}}{\rho} = \frac{1}{A_S} \iint \left| \vec{r}_0 \cdot \vec{r}_n \right| dx\, dy \; . \tag{3.17}$$

Specifically, for the egg-carton surface (Eq. 3.6) this becomes (the MATLAB function is provided in Appendix B.1)

$$\begin{aligned} \frac{\rho_{\text{ff}}}{\rho} = & \frac{1}{A_S} \int_S \left[ 1 + (ka \cos kx \cos ky)^2 + (ka \sin kx \sin ky)^2 \right] \\ & \Big( - ka \cos kx \cos ky \sin\theta_s \cos\phi_s \\ & + ka \sin kx \sin ky \sin\theta_s \sin\phi_s + \cos\theta_s \Big)\, dS \; . \end{aligned} \tag{3.18}$$

For a zenith sun and a surface roughness of $a/l = 0.1$ the reflectance ratio drops 8% (not shown in figures); at $a/l = 0.2$, 24%, and $a/l = 0.5$, 55% (Fig. 3.2). In the absence of any shadowing or obscuration, the reflectance drop is independent of incidence direction and absolute length of the period of the defining waveform. For the same defining waveform as the egg-carton above, Zaneveld & Boss (2003) show that a two-dimensional sinusoidal wave with $a/l = 0.1$ gives a drop in the reflectance ratio of 8%; $a/l = 0.2$, a drop of 22%; and $a/l = 0.5$, a drop of 49%. To compare, the Zaneveld & Boss (2003) solution for a triangular wave has the reflectance ratio drop by 7%, 21.9%, and 55%, respectively.

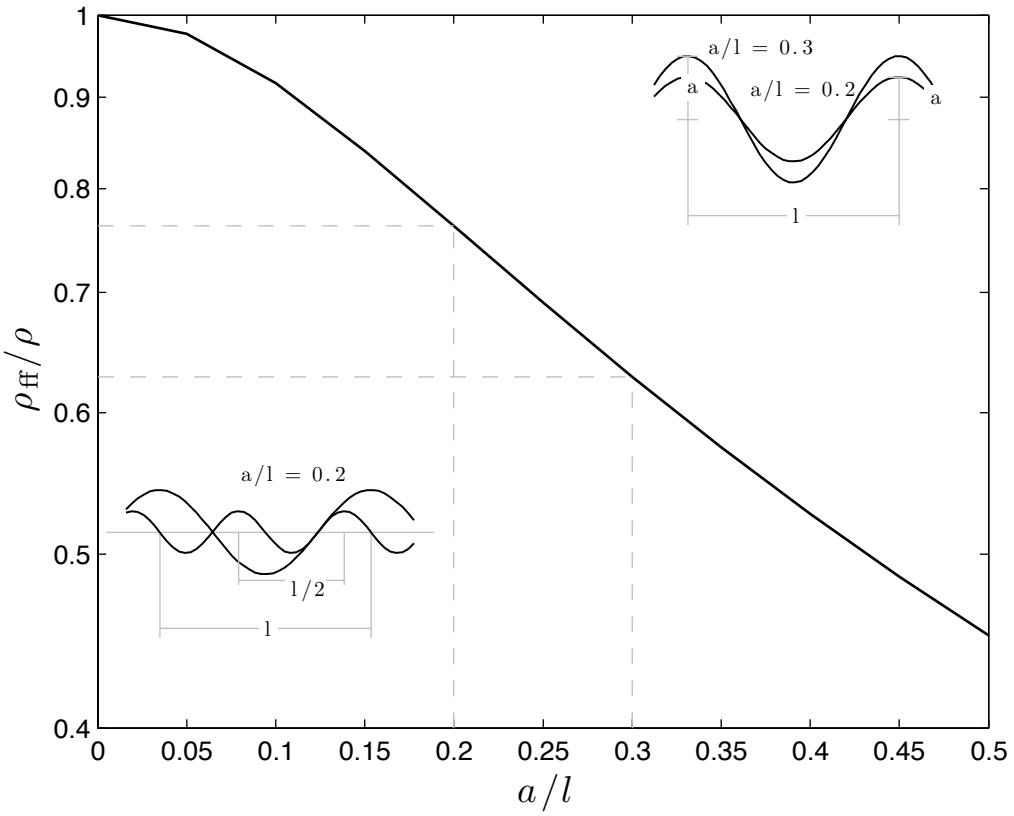


Figure 3.2: Ratio of far-field reflectance of a periodic surface relative to that of a flat surface at nadir viewing. The reflectance ratio remains the same regardless of the absolute length of the defining period of the sinusoidal function. The detector is looking straight down and sees enough waveforms so that the reflectance measured is the far-field value. The top inset shows a scale model of a change in $a/l$ keeping the period constant; the lower inset shows a constant $a/l$ but with the period halved.

## 3.6 Near-field solution

A part of the egg-carton surface that can be considered to represent any other area on the surface is a section that would have all possible facet normals and all possible surface heights contained in it. One full "period" in three dimensions would have a vertical projected area (i.e., a domain defined on the $xy$-plane) of a rectangle connecting any four proximal peaks, Fig. 3.3. A detector that sees through a right circular cone has an elliptic footprint. However, a detector positioned to look straight down has a circular footprint (Fig. 3.3). We consider now the effects on the reflectance for a detector in the near-field, i.e., one that sees only part of a full period.

For the realization here, we assume a hypothetical detector with a half-angle $\theta_d = 5^\circ$ located at a point $(r_x, r_y, r_z)$ oriented downwards, so that at the reference plane, $z = 0$, the detector looking straight down has a circular footprint radius of $r = r_z \tan\theta_d$. Assuming that the boundary of the intersection of the detector field of view and the surface is this same projection, and using similar arguments in Eqs. 3.15-3.18, the ratio of the effective reflectance of the rough surface to that of a flat one with the same projected area is (the MATLAB function is provided in Appendix B.2)

$$\begin{aligned}\frac{\rho_{\text{eff}}}{\rho} =& \frac{1}{\pi r^2}\int_{r_x-r}^{r_x+r}\int_{r_y-\sqrt{r^2-(x-r_x)}}^{r_y+\sqrt{r^2-(x-r_x)}} \Big\{1+\Big[ka\,\cos kx\,\cos ky\Big]^2 \\ &+\Big[ka\,\sin kx\,\sin ky\Big]^2\Big\}\Big[-ka\,\cos kx\,\cos ky\sin\theta_s\cos\phi_s \\ &+ka\,\sin kx\,\sin ky\sin\theta_s\sin\phi_s+\cos\theta_s\Big]dx\,dy\,. \end{aligned} \tag{3.19}$$

As the relative detector distance, $r_z/l$, increases away from the surface, the near-field values approach the far-field limit, Fig. 3.4. The error oscillates around

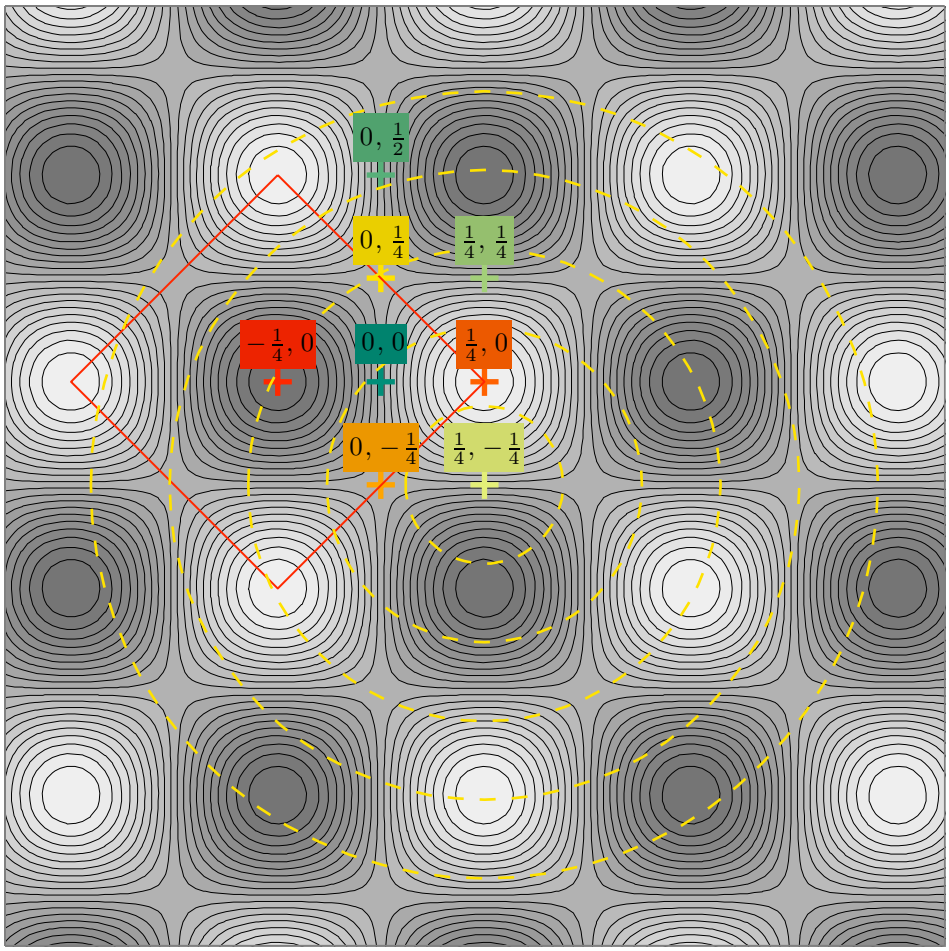


Figure 3.3: Schematic of an egg-carton surface viewing straight down. The point $(0, 0)$ is at the origin of the function domain and sits at the average level, right between a trough $(-\frac{1}{4}, 0)$ (darker area) and a peak $(\frac{1}{4}, 0)$ (lighter area), looking from left to right. The scale is normalized: one unit (from peak to peak in the horizontal or vertical directions) is equivalent to the length $l$ of the defining waveform. The point $(0, \frac{1}{2})$ is the reverse in orientation of $(0, 0)$: it is between a peak and a trough. The points $(\frac{1}{4}, \frac{1}{4})$ and $(\frac{1}{4}, -\frac{1}{4})$ have the same orientations but one rotated 90° from the other. The points $(0, \frac{1}{4})$ and $(0, -\frac{1}{4})$ sit at the center of local extrema. The square around $(-\frac{1}{4}, 0)$ shows what would be considered to be a "unit" surface area that would contain all the possible orientations of normal vectors and all possible heights. As the detector moves away from $(\frac{1}{4}, -\frac{1}{4})$ the size of its footprint increases, as indicated by the enlarging circles centered around it.

the far-field value and starts to create a clear envelope that is evident beyond $r_z/l \approx 10$ for the cases considered. The dashed lines on the plots are mirror graphs along the far-field value and are only used to illustrate an envelope of minimum and maximum values that can be expected. The rougher the surface (see change in roughness in top inset of Fig. 3.2), the sooner the envelope narrows and the quicker the reflectance ratios approach the far-field values. This means that measurements can be made at a certain distance from the surface so that the far-field value can be used to correct the reflectance for roughness effects if the roughness can be known. However, shallow water environments are typically less than a few meters deep and the air-water interface further complicates the surface reflectance.

Another way to look at the results is to normalize the data by the far-field values for each specific $a/l$, see Fig. 3.5. These plots include black dashed lines showing an upper and lower 0.5% change away from the far-field values. As before, in Fig. 3.4, values approach the far-field values much more quickly when the roughness is greater. In Fig. 3.5, however, the normalization shows that the outer envelope of values reach the 0.5% margin at the same depth regardless of roughness for the same absolute period length. Furthermore, the smaller the dimensions of the roughness, the sooner the reflectance errors diminish, compare Fig. 3.5(a,b) with (c,d). For distances of a few meters, reflectance errors due to roughness effects alone can be as high as approximately 20%. If, however, numerous measurements can be made directly above different points on the surface of interest (similar to the idea of taking pairs of points in Snyder 1998) and an average apparent reflectance can be deduced, then with an assumption of the "real" reflectance, $\rho$, of the surface, a correction can be made and a roughness approximated. Alternatively, reflectance

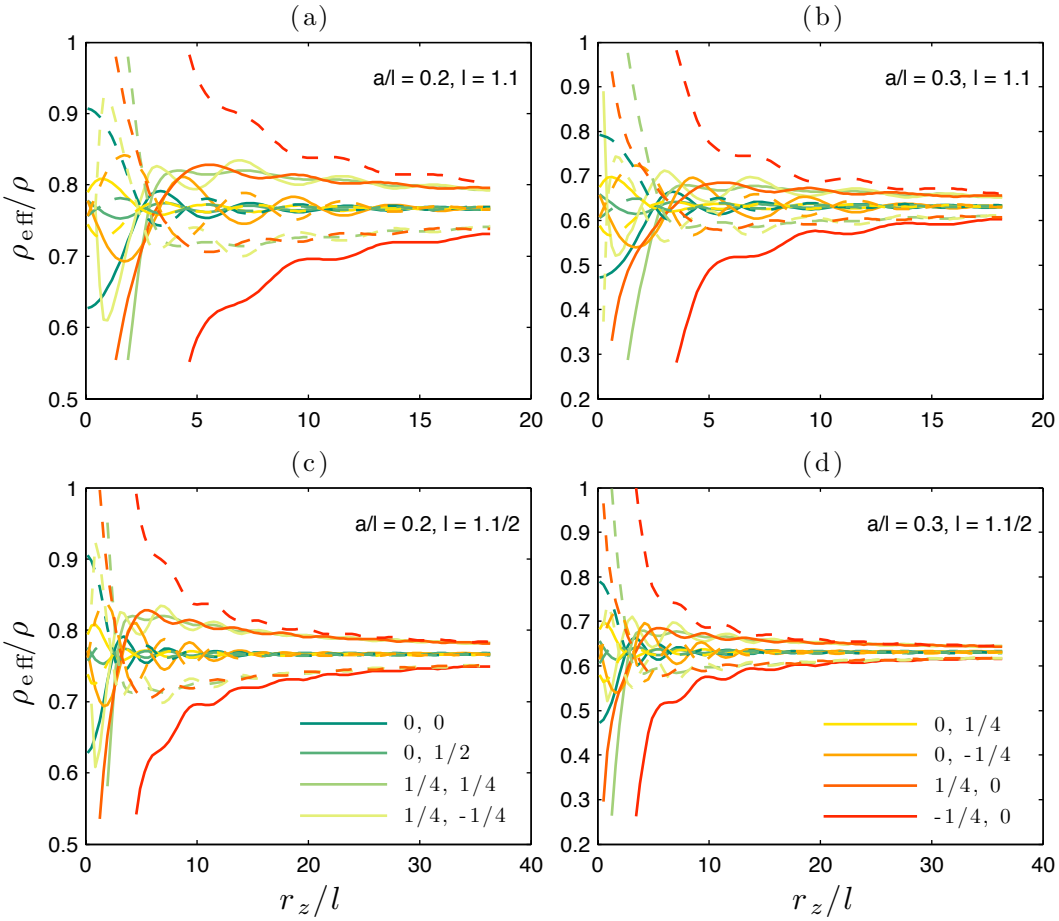


Figure 3.4: Effective reflectance of a periodic surface relative to that of a flat surface. For this exposition we consider roughnesses of $a/l = 0.2$ (a,c) and 0.3 (b,d) for surfaces with periods of 1.1m (a,b) and 1.1/2m (c,d). A distance normalized by the period of the relevant waveform is on the $x$-axis. The dashed lines are the reflectance ratios mirrored along the far-field values for each $a/l$ (Fig. 3.2) showing the minimum and maximum values that can be expected within an envelope that narrows as the relative detector distance, $r_z/l$, increases. The dark green lines are reflectance ratios with a detector looking straight down at the surface origin ($(0,0)$ in Fig. 3.3). The outermost lines represent the values for when the detector is directly above the middle of a trough.

distributions for two or more different incidence directions may be made to infer surface roughness (see Levin et al. 2004).

## 3.7 Summary and limitations

An extension of the concept and two-dimensional model of Zaneveld & Boss (2003) into three dimensions has been provided. As surface roughness increases, the reflectance approaches that of a flat Lambertian surface, with a "correction" factor for a far-field value that is (made) dependent only on the amplitude-to-period ratio of the defining surface waveform. When the detector is close enough to the surface and it sees only part of what would be considered an area that represents the full variation of surface slopes and heights, the reflectance variation is greater and care must be taken when taking measurements in such situations. A future consideration would be to see how measurements from different points above the surface could provide a way to determine how much reflectance variation there is and deduce what the underlying reflectance might be. Finally, regardless of surface roughness the envelope enclosing the roughness variation approaches the 0.5% (arbitrary value) variation at the same detector distance, but for a waveform of constant period.

While the results only consider a detector at nadir (a single direction), insight into the effects of a change in surface roughness is developed. Furthermore, an analytic periodic surface is used to simplify further roughness comparisons (and solutions) as well as provide a clear measure of surface roughness (the amplitude-to-period ratio, $a/l$). Effects of shadowing are included indirectly: these produce the open-ended envelopes for smaller detector distances in Figs. 3.4 and 3.5. No interference effects are included in the theory of geometrical optics (otherwise, strong

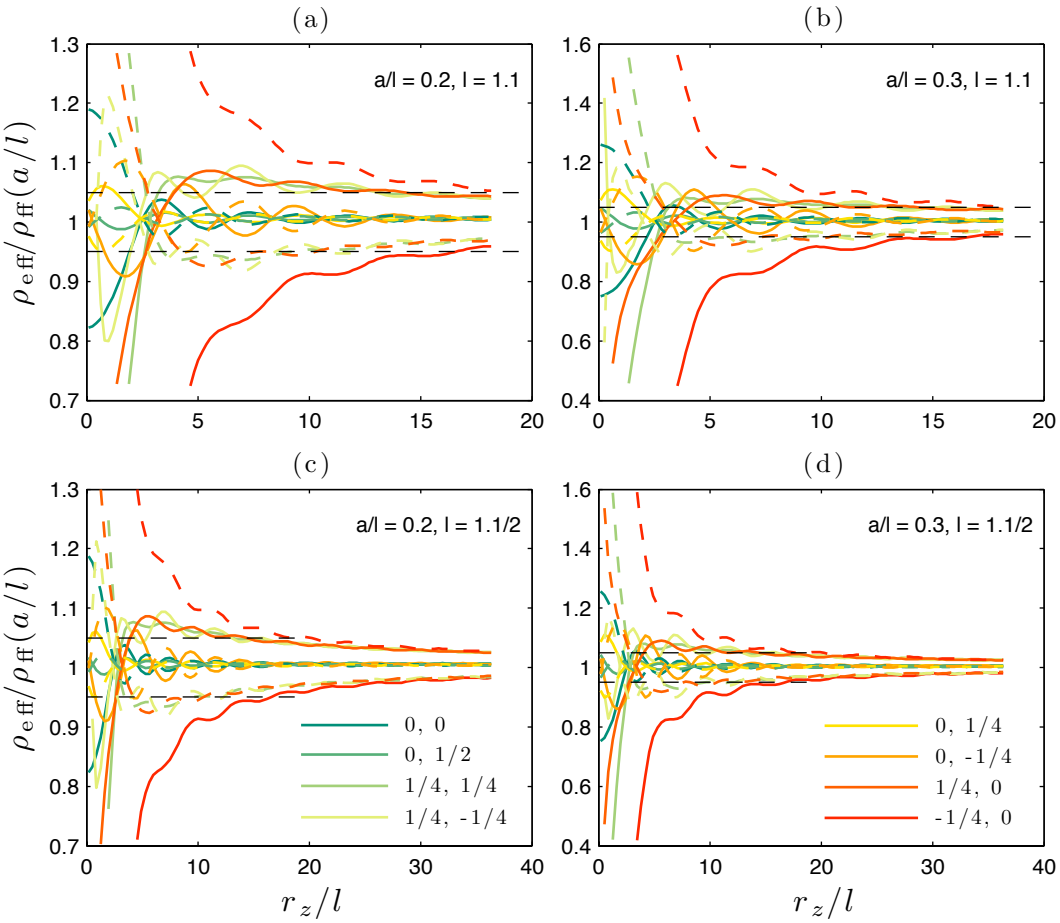


Figure 3.5: Reflectance ratios normalized to the far-field values given particular roughness ratios, $a/l$. The results are the same as in Fig. 3.4 except that the values are normalized by the far-field values, $\rho_{\mathrm{ff}}/\rho$, as given in Fig. 3.2 for each $a/l$. The $y$-axis thus becomes $\rho_{\mathrm{eff}}/\rho_{\mathrm{ff}}(a/l)$. Black dashed lines indicate the 0.5% change away from the far-field value for each set.

resonances in the magnetic field is expected to be apparent for rough surfaces, see Zaki & Neureuther 1971b). The surface is assumed to have infinite lateral extent so that edge effects are avoided (for a treatment of surfaces with boundaries, see the wave solution by Millar 1973). Oren & Nayar (1995) show that for diffuse surfaces, the apparent reflectance is lower than the Lambertian value of a flat surface (or facet) in the forward scattering region (around the specular direction). Only the nadir viewing results are provided here but are in agreement with their observation. Furthermore, Oren & Nayar (1995) expect the apparent reflectance to increase outward in the side scattering region. Diffuse surfaces are expected to have a strong backscattering component (see, e.g., Oren & Nayar 1995), so that coupled with the detector looking straight down at a surface, one measures the strongest possible return and provide the effects of an extreme case with convenient simplifying assumptions. Only Lambertian reflectance is considered, Part III (Chap. 4) inspects the behavior of specular reflections (adopting the model which was popularized by Torrance & Sparrow 1967).

CHAPTER 4

# PART III. THE BIDIRECTIONAL REFLECTANCE DISTRIBUTION FUNCTION OF A ROUGH AIR-WATER-BOTTOM SYSTEM: THE SPECULAR COMPONENT

## 4.1 Introduction

Surfaces scatter light differently in different directions: a purely mirror-like surface scatters light in the direction opposite the incident light at an equal angle away from the surface normal, i.e., the specular direction; a diffuse surface scatters light equally in all directions away from the surface. Most natural surfaces have both a specular and a diffuse property. Surfaces are classified as one or the other based on which one component dominates the overall effect. Most are considered to be diffuse, e.g., Zhang et al. (2003a) and Maignan et al. (2004) for ooid sand, Sandmeier et al. (1998b,a) and Sandmeier (2000) for grass, and van Ginneken et al. (1998), Govaerts & Verstraete (1998) and Hu et al. (1999) for plant canopies. The specular component is responsible for the reflectance peak around the specular direction (e.g., for snow and sea ice, see Jin & Simpson 1999). We wish to capture the qualitative aspects of separating out the behavior and effects of the specular component from a rough surface and so be able to study it independently. For specular reflection from a rough surface, each surface element reflects light into a single direction and the distribution of surface slopes results in a distribution of reflected light. The method chosen is computationally efficient for specular reflection but is inefficient for diffuse reflection since it would require running the calculations for all possible directions, i.e., to allow for the integration of the diffuse reflectance into all directions for each possible slope.

Reflection is the process whereby light impinging upon a boundary is redirected away from this boundary (on a path back into the original medium). Transmission is when light goes through the boundary whereby its direction is affected. Light is "absorbed" when it is transformed into another form of energy when its intensity decreases as it travels through a medium. In the current treatment we ignore absorption in the water. Nevertheless, we later point out that to affect the resulting polarization of the system absorption needs to be taken into account. Only elastic scattering—where there is a change in the direction of light propagation but a retention of its energy—is considered.

Many studies on surface scattering assume that the reflectance distribution of a surface is azimuthally symmetric along the principal plane, the plane defined by the normal to the surface of interest and the direction of the light source (e.g., an ooid sand surface in Mobley et al. 2003). If the roughness is isotropic (i.e., independent of direction) or when it is aligned along the principal plane, the resulting symmetry can be useful in studying the optical properties of the surface. In such a situation, the reflectance peak lies along the principal plane. In the natural environment, however, the surface roughness may be anisotropic (directionally dependent), and the sun (the dominant light source) and detector may not be aligned with the orientation of the physical roughness pattern. Note that when skylight contributes significantly to the light source of a system, there is not one source direction. Aas & Høkedal (1999) argue that the distribution of reflected radiance off the sea surface is more a function of the sky radiance distribution than it is of the roughness of the sea surface. In this study, we use the Mueller matrix approach to the problem allowing for anisotropic roughness that is not aligned along the principal plane to be included but leave further analyses that takes this into account for another time

and focus the discussion only on surface roughness orientations that are aligned along the principal plane.

The scattering problem from Parts I (Chap. 2) and II (Chap. 3) are extended here into full hemispherical reflectance distributions for light traveling in and out of water with a wind-roughened surface and an optically bright underwater bottom surface with statistical roughness. To simplify the problem, let the underwater surface be homogeneous, highly reflective, and covered with sand, having an average reflectance of 0.4 in the visible range (Louchard et al. 2003). We employ the statistical distribution of water surface normals as determined by Cox & Munk (1954, 1956) (realizing that improvements to their method and results have been proposed elsewhere, e.g., Wentz 1976). A similar approach is used to quantify the distribution of normals of the underwater surface that expresses the surface roughness. Both these steps allow us to handle the system as if the surface were spatially averaged (the two other important considerations are taken care of by other means: the time averaging operating under the geometric optics assumption and the linearization of the problem through the Mueller matrix approach). Vector transformations are similar to standard techniques, e.g., Mullamaa (1962), as well as Yang et al. (2003) who analyze the resulting polarization, as do Kattawar & Adams (1989).

## 4.2 Angles and vectors in three dimensions

There is a symmetry expected along the plane of the sun in the light interactions of reflection, refraction and transmission in the natural environment, suggesting that the reflectances are isotropic. To take advantage of this, we choose a coordinate system that is arbitrarily aligned with the sun: the global reference frame is where

the sun location falls along the horizontal $y$-axis at an azimuth of $\phi_s = 90°$. We assume that the predominant wind direction is aligned along the $y$-axis and the bottom surface roughness is aligned perpendicular to it. When the solar reference plane and the wind and bottom reference planes are not aligned, we expect the symmetry of the interactions to be lost (loss of symmetry is also expected when the underwater light field is asymmetric, see Timofeeva 1962). The current formulation allows for this and we show a few results, but most of the analyses deal with the symmetric case since the maximum reflectance change in response to variations in the viewing and illumination directions occur with symmetric conditions. For reflectances outside the principal plane, a model in three dimensions is shown by Zhu & Zhang (2004) to work better than one dimension fewer, especially for surfaces with non-Gaussian slope distributions.

Let the angular pair $(\theta_s, \phi_s)$ indicate the sun location in the sky dome above a reference point on the sea surface, a location which can also be expressed as a linear combination of the unit directional vectors $\vec{\mathrm{i}}$, $\vec{\mathrm{j}}$ and $\vec{\mathrm{k}}$ in the Cartesian coordinate system along the $x$-, $y$- and $z$-directions, respectively, so the angular pair also represents the unit vector in component form as

$$(\theta_s, \phi_s) \qquad \text{or} \qquad \vec{r_s} = r_{sx}\,\vec{\mathrm{i}} + r_{sy}\,\vec{\mathrm{j}} + r_{sz}\,\vec{\mathrm{k}}\,. \tag{4.1}$$

Similarly, a point in the sky is represented as

$$(\theta_0, \phi_0) \qquad \text{or} \qquad \vec{r_0} = r_{0x}\,\vec{\mathrm{i}} + r_{0y}\,\vec{\mathrm{j}} + r_{0z}\,\vec{\mathrm{k}}\,. \tag{4.2}$$

The transformation is such that given any angular pair $(\theta, \phi)$ and a vector length $r \geq 0$ the $x$-, $y$- and $z$- components, are respectively given by

$$r_x = r \sin\theta \cos\phi \tag{4.3}$$

$$r_y = r \sin\theta \sin\phi \tag{4.4}$$

and

$$r_z = r\cos\theta\ . \tag{4.5}$$

By definition, $|\vec{r}| = 1$ for a vector of unit length. The reference to the directions in the coordinate space depends on whether the spherical coordinates or the vector components are appropriate to facilitate the calculations. Similarly, a reflected direction is denoted by

$$(\theta_1, \phi_1) \qquad \text{or} \qquad \vec{r_1} = r_{1x}\,\vec{\mathrm{i}} + r_{1y}\,\vec{\mathrm{j}} + r_{1z}\,\vec{\mathrm{k}}\ , \tag{4.6}$$

$$(\theta_2, \phi_2) \qquad \text{or} \qquad \vec{r_2} = r_{2x}\,\vec{\mathrm{i}} + r_{2y}\,\vec{\mathrm{j}} + r_{2z}\,\vec{\mathrm{k}}\ , \tag{4.7}$$

as appropriate, and so on.

## 4.3 Sun irradiance and sky luminance distribution

In this section we describe the source of light for the model. Seen at the mean distance on the surface of the earth from the sun, the solar disk subtends a diameter of approximately 0.535° or a radius of 0.2675° (e.g., Cox & Munk 1954, 1956, McCluney 1994, Mobley 1994, p. 35, Walker 1994). Thus, in unit radians, the sun has an angular radius of

$$\varepsilon \approx 0.2675^\circ \left(\frac{\pi[\mathrm{rad}]}{180^\circ}\right) = 0.0045\ [\mathrm{rad}] \tag{4.8}$$

so that it subtends a solid angle at a point on the earth of approximately

$$\Omega_s = 2\pi\big(1 - \cos\varepsilon\big) = 6.85 \times 10^{-5}\ [\mathrm{sr}]\,. \tag{4.9}$$

This is a specific application of the concept of a steradian measure, which is best illustrated using Fig. 1.2 and presented here again as Fig. 4.1. A source that is

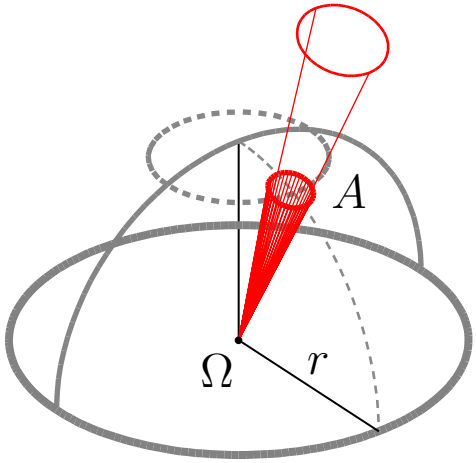


Figure 4.1: The concept of a spherical cap as an extension of the concept of the projected area that helps define the measure steradian: the cap here is the surface with area $A$ in the figure.

approximately a disk in the sky is projected onto a spherical cap with area $A$ on a unit hemisphere ($r = 1$) above the point of interest on a surface. Let the arc length along the meridian plane that defines a radius for this area be some angle $\theta'$, then in general the solid angle of this spherical cap is given by

$$\Omega = \int_0^{2\pi} \int_0^{\theta'} \sin\theta \, d\theta \, d\phi = 2\pi\big(1 - \cos\theta'\big) \text{ [sr]} \, . \tag{4.10}$$

Notice that the spherical cap has full azimuthal variation; only the zenith angle is changed from the full hemisphere, see Eq. 2.6 for the differential form (definition provided in any standard photometry or radiometry text, e.g., McCluney 1994, Mobley 1994, Walker 1994).

In the treatment here we initially limit the input irradiance to the sun and assume that the sky is "black". However, in general, the light from the sky is not uniform and, although it is only roughly 10% of the intensity from the sun at its

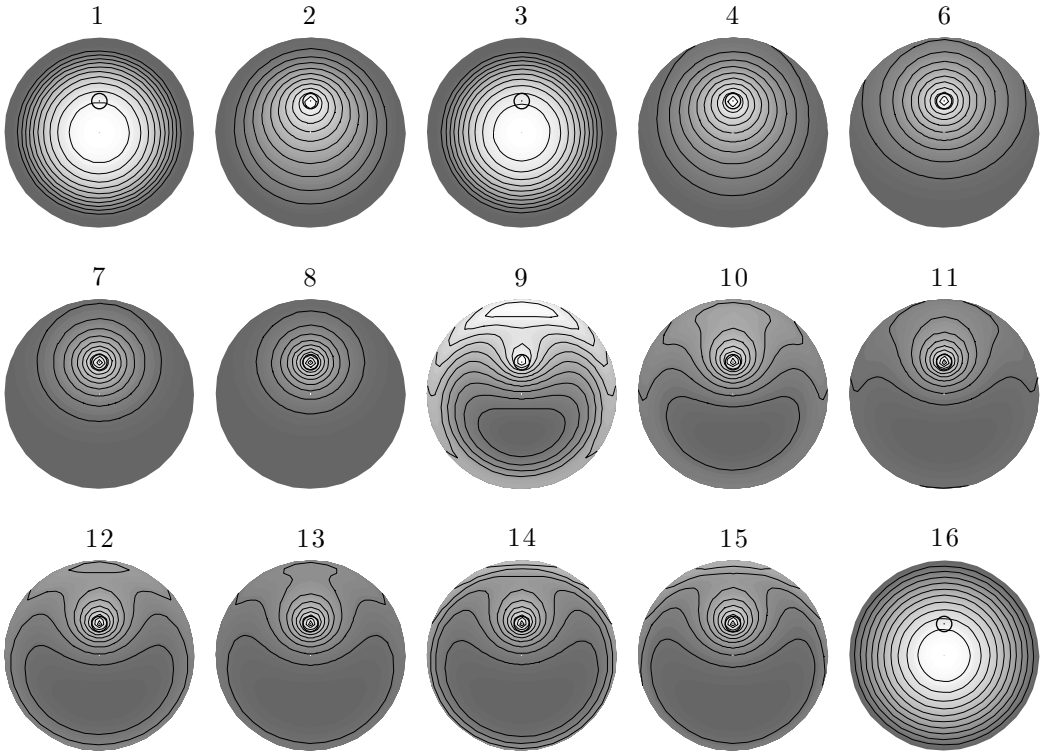


Figure 4.2: ISO standard (2004) sky types for the sun at an angle of $\theta_s = 30°$ from zenith (equal radial measure from the center out to 90°) and an azimuth $\phi_s = 90°$ (pointing straight up), as indicated by the circle-dot in each panel. Sky Type 5, being that for a uniform sky, is not included in this figure.

strongest, it can affect the pattern of the light reflected from the water surface. When we do consider a diffuse sky, we use the set of theoretical hemispherical sky *luminance* distributions from the ISO standard (ISO 2004) to represent variations to this input distribution and call it $L_{\text{sky}}(\theta_s, \phi_s)$. Luminance is radiance that is limited to the visible range of radiation, i.e., radiance integrated over only the visible range to get the irradiance (thus implying wavelength dependence). The theoretical distributions are presented in Fig. 4.2 for a sun angle of $\theta_s = 30°$ from zenith (the sun is located along the positive $y$-axis at $\phi_s = 90°$). The symbol (circle-dot) in each plot indicates the position of the sun.

These are theoretical plots and conditions in the natural environment affect the symmetry along the solar plane (see Liu & Voss 1997). The brightness gradient represents the ratio of the brightness anywhere in the sky to that of the brightest point in the sky. The unit measure from the ISO standard has been normalized here, which is given as the ratio of the brightness to that *at zenith*; to obtain absolute values of the distribution, the brightness at zenith needs to be known. These distributions are defined by smooth continuous functions and are best for representing cloudless skies or a more homogeneous sky cover. When the cloud cover is broken, these distributions are approximate at best. Types 1-4 present an overcast sky; with steep gradations for Types 1 and 2, moderate for Types 3 and 4. Type 5 is for a uniform sky and is not included in Fig. 4.2. Partly cloudy skies are presented as Types 6-10. Type 11 is for a "white-blue" sky. A clear sky with low turbidity is Type 12 and a clear sky with a polluted atmosphere Type 13. Types 14 and 15 are for turbid skies. Finally, Type 16 is for a "general sky" representing the traditional overcast sky formula used in many lighting simulations. The distributions are symmetric along the solar plane with most skies having the brightest spot in the sun direction, except for overcast skies (Types 1, 3 and 16) where it is brightest at zenith. Note that the irradiance from the sun is considered of a separate source and is not included in these distributions. Given the location of the sun in the sky and a sky type, a MATLAB program is used to determine the sky luminance distribution as presented in the ISO standard and is provided in Appendix B.3.

In the calculations, when the sun is not the only source of illumination, we use Sky Type 9, which represents a sky that is "partly cloudy, with the sun obscured" simply for its perceptibly more interesting patterns of variation. For all sky types,

two underlying functions help determine the brightness distribution. One is dependent on the distance of a sky element from zenith and the other is its distance from the sun in the sky. The gradation functions for Types 9-15 describe the brightening of the sky toward the horizon. The standard specifies the luminance distribution as the brightness ratio of a part of the sky relative to that at zenith. We modify that here to have its brightest spot in the direction of the sun, normalizing the distribution in that direction and calling it $\bar{L}_{\text{sky}}$. This simplifies the assignment of radiance values later for integration.

## 4.4 Roughness, surface characteristics and projected areas

Assume that the measure of physical roughness of the surface is much greater than the electromagnetic wavelength used so that geometric optics can be applied. The theory of geometric optics utilizes the ray nature of light that describes its gross behavior when the physical dimensions of the interacting material is much larger than its wavelength. Recall that two surfaces are of interest here: the water surface that is wind-ruffled and the underwater bottom surface. The water surface roughness is dependent on the prevailing wind direction. Although it is meant to be locally random as in the Oren & Nayar (1995) model, it is essentially directional (wind-ruffled) in the macro scale. This function is dependent on wind speed and direction and is based on empirical observations by Cox & Munk (1954, 1956) who looked at sun glint (see Walker 1994, p. 413, for sun glint resolution) and the speckle pattern from aerial photographs of the ocean. The roughness of the underwater bottom is also considered to be anisotropic. However, it is modeled using a sinusoidal function, much like an egg-carton surface (another possibility is to use the function of a trochoid to model the surface "shape" as in

Fuks 2002). Only the *physical* roughness of the surfaces are analyzed. Optical roughness is a different measure: a smooth surface has ${r_\perp}^2/r_\parallel = 1.0$ ($r_\perp$ and $r_\parallel$ are the perpendicular and parallel reflection coefficients) at $\theta_0 = 45°$ (e.g., Stagg & Charalampopoulos 1991).

Let the underwater bottom surface be represented by the function

$$f_b(x, y) = a \sin kx \cos ky \ , \tag{4.11}$$

(also Eq. 3.6), where

$$k = \frac{2\pi}{l} \ , \tag{4.12}$$

$a$ is the amplitude of the defining waveform, which is aligned along the $x$-axis, and $l$ is its period. When the defining waveform of the bottom surface is not aligned with the $x$-axis but is rotated about the global normal an angle $\phi_{b'}$, then the surface function becomes

$$f_{b'}(x, y) = a \sin \big(kx \cos \phi_{b'} + ky \sin \phi_{b'}\big) \cos \big( - kx \sin \phi_{b'} + ky \cos \phi_{b'}\big) \ . \tag{4.13}$$

Note that when $\phi_{b'} = 0$, Eq. 4.13 reverts to Eq. 4.11. There is no slope to this surface, i.e., the average height is constant throughout. Mobley & Sundman (2003) consider the effects of a sloping bottom and find that for surface slopes less than 20° from the horizontal the errors in the upwelling radiances are less than 10%. For a treatment that consider "blocks" rather than points as causing the variation in surface roughness such as for forested canopies see, for example, the work done by Meerkoetter (1990) (another approach is presented by Liang & Strahler 1993).

Given the assumption of no absorption either in air or in water, we may ignore the distance each ray travels in the system. We also consider only a time average of illumination, meaning that the illumination is the same at every point on the bottom. Furthermore, illumination from the entire water surface at any point on

the bottom can be represented by the illumination provided from one point on the water surface over a sufficiently long time span. This allows us to replace the water surface with a probability density function for the slopes applied at a single point (the ergodic hypothesis, or spatial averaging as discussed by, e.g., Walker 1994, Snyder 2002, and used to eliminate "glitter" by Plass et al. 1975).

The water surface is described by a distribution function giving the probabilities that slope values representing surface facet normals will occur. The normal vector to the bottom surface function $z = f(x, y)$ (oriented in the positive $z$ direction) at a point $(x_0, y_0)$ is represented by

$$\vec{n}_{(x_0,y_0)} = -f_x\,\vec{\mathrm{i}} - f_y\,\vec{\mathrm{j}} + \vec{\mathrm{k}}\,, \tag{4.14}$$

where $f_x$ and $f_y$ are the partial derivatives of $z = f(x, y)$ at $(x_0, y_0)$ with respect to $x$ and $y$, respectively. A *unit* normal vector represents the direction of $\vec{n}_{(x_0,y_0)}$ by

$$\vec{r}_n = \frac{-z_x}{\sqrt{{z_x}^2 + {z_y}^2 + 1}}\,\vec{\mathrm{i}} + \frac{-z_y}{\sqrt{{z_x}^2 + {z_y}^2 + 1}}\,\vec{\mathrm{j}} + \frac{1}{\sqrt{{z_x}^2 + {z_y}^2 + 1}}\,\vec{\mathrm{k}}\,, \tag{4.15}$$

the length of the normal vector being given by

$$\left\|\vec{n}\right\| = \sqrt{{z_x}^2 + {z_y}^2 + 1}\,. \tag{4.16}$$

If the unit normal vector at $(x_0, y_0)$ is defined to be at an angle $\theta_n$ from zenith and an azimuth $\phi_n$ (from the global $x$-axis) in Fig. 4.3, then in vector-component form the unit normal vector is represented by

$$\vec{r}_n = \sin\theta_n \cos\phi_n\,\vec{\mathrm{i}} + \sin\theta_n \sin\phi_n\,\vec{\mathrm{j}} + \cos\theta_n\,\vec{\mathrm{k}}\,. \tag{4.17}$$

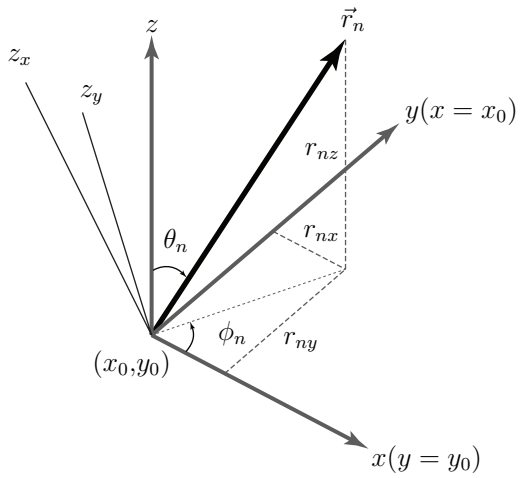


Figure 4.3: A unit normal vector $\vec{r}_n$ on the bottom surface at a point $(x_0, y_0)$ can be described by specifying the angle it makes from zenith $\theta_n$ and its azimuth $\phi_n$ from the $x$-axis. The $x$-, $y$- and $z$-vector component lengths are indicated by $r_{nx}$, $r_{ny}$ and $r_{nz}$, respectively. The slope of the surface tangent to the facet at $(x_0, y_0)$ on a plane parallel to the $x$-axis is given by the partial derivative $f_x$ at that point ($f_x$ moves along $z_x$). Similarly, the partial derivative $f_y$ gives the slope of the surface tangent to the facet that is parallel to the $y$-axis ($f_y$ moves along $z_y$). Both the lines $z_x$ and $z_y$ define the plane tangent to the facet at $(x_0, y_0)$.

Equating the components of Eqs. 4.15 and 4.17 we have

$$r_{nx} = \frac{-z_x}{\sqrt{{z_x}^2 + {z_y}^2 + 1}} = \sin\theta_n \cos\phi_n \tag{4.18}$$

$$r_{ny} = \frac{-z_y}{\sqrt{{z_x}^2 + {z_y}^2 + 1}} = \sin\theta_n \sin\phi_n \ , \tag{4.19}$$

and

$$r_{nz} = \frac{1}{\sqrt{{z_x}^2 + {z_y}^2 + 1}} = \cos\theta_n \ . \tag{4.20}$$

By substituting Eq. 4.20 into Eqs. 4.18 and 4.19, the slope of the tangent lines to a surface facet at the point $(x_0, y_0)$ in the plane $y = y_0$ and $x = x_0$ are given by the partial derivatives of the function at the point along these planes, respectively, and are given by

$$f_x = -\cos\phi_n \tan\theta_n \tag{4.21}$$

and

$$f_y = -\sin\phi_n \tan\theta_n \ . \tag{4.22}$$

Furthermore, we know that the observed distribution of facet slopes as measured by Cox & Munk (1954) were made in relation to the predominant wind direction. Let this wind direction be at an azimuth angle $\phi_w$, a distance $\phi_w - \phi_s$ away from the solar direction. Rotating the solar reference frame $(x, y)$ to align with the wind reference frame $(x', y')$ in Fig. 4.4, the projected angles become

$$f_{x'} = -\cos(\phi_n - \phi_w)\tan\theta_n \tag{4.23}$$

and

$$f_{y'} = -\sin(\phi_n - \phi_w)\tan\theta_n \ . \tag{4.24}$$

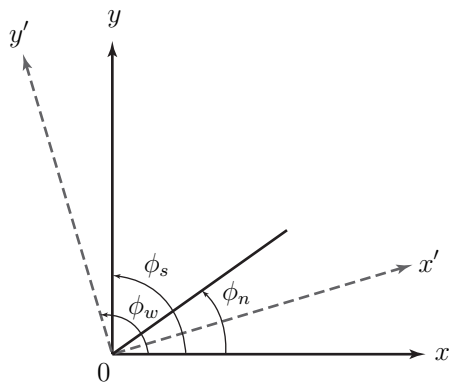


Figure 4.4: Rotating the sun reference frame to align with the wind reference frame aligned along an azimuth $\phi_w$, assuming that the solar plane, $\phi_s$, is oriented along the $y$-axis of the global reference frame. The facet tilt direction (of greatest ascent) is $\phi_n$. The angle of rotation is given by $\phi_w - \phi_s$.

The probability *density* function of normals to the water surface facets is

$$\begin{aligned} p(f_{x'}, f_{y'}) =& \frac{1}{2\sigma_{x'}\sigma_{y'}} \exp\left[-\frac{1}{2}\left(\xi^2+\eta^2\right)\right]\left\{1 - \frac{1}{2}c_{21}\left(\xi^2-1\right)\eta\right. \\ & - \frac{1}{6}c_{03}\left(\eta^3-3\eta\right) + \frac{1}{24}c_{40}\left(\xi^4-6\xi^2+3\right) \\ & \left. + \frac{1}{4}c_{22}\left(\xi^2-1\right)\left(\eta^2-1\right) + \frac{1}{24}c_{04}\left(\eta^4-6\eta^2+3\right)\right\} , \end{aligned} \tag{4.25}$$

empirically determined by Cox & Munk (1954, 1956, Eq. 6.2-8), where

$$\xi = \frac{f_{x'}}{\sigma_{x'}} \tag{4.26}$$

and

$$\eta = \frac{f_{y'}}{\sigma_{y'}} \, . \tag{4.27}$$

The skewness coefficients of the distribution are $c_{21}$ and $c_{03}$; the peakedness coefficients are $c_{40}$, $c_{22}$ and $c_{04}$ and are empirically derived from photographs of the sea surface; $\sigma_{x'}$ and $\sigma_{y'}$ are the variances (root mean square slopes) in the $x'$- and $y'$-directions, respectively. Explicitly, the coefficients of the distribution for a clean

water surface (e.g., no oil slicks) are functions of the wind speed $v$ [ms$^{-1}$] :

$$\sigma_{x'} = \sqrt{0.003 + 1.92 \times 10^{-3} v} \tag{4.28}$$

$$\sigma_{y'} = \sqrt{0.000 + 3.16 \times 10^{-3} v} \tag{4.29}$$

$$c_{21} = 0.01 - 0.0086 v \tag{4.30}$$

$$c_{03} = 0.04 - 0.0330 v \tag{4.31}$$

$$c_{40} = 0.40 \tag{4.32}$$

$$c_{22} = 0.12 \tag{4.33}$$

and

$$c_{04} = 0.23 \; . \tag{4.34}$$

We use this set of values in the current investigation; parametric values for other water types can be found in Cox & Munk (1956).

The probability density function is subject to the following constraint, which includes all possible slopes:

$$\iint_{-\infty}^{+\infty} p(f_{x'}, f_{y'}) \, df_{x'} \, df_{y'} = 1 \; . \tag{4.35}$$

A transformation of variables produces an integral with respect to $(\theta_n, \phi_n)$

$$\iint_{-\infty}^{+\infty} p(f_{x'}, f_{y'}) \, df_{x'} \, df_{y'} = \int_0^{2\pi} \int_0^{\frac{\pi}{2}} p\big(g(\theta_n, \phi_n), h(\theta_n, \phi_n)\big) \left| \frac{\partial(f_{x'}, f_{y'})}{\partial(\theta_n, \phi_n)} \right| d\theta_n \, d\phi_n \; , \tag{4.36}$$

with

$$\left| \frac{\partial(f_{x'}, f_{y'})}{\partial(\theta_n, \phi_n)} \right| \tag{4.37}$$

being the Jacobian of the transformation.

Any point on the surface viewed directly along the facet normal has an area of projection on the unit sphere of

$$p(\theta_n, \phi_n)\, d\Omega_n \tag{4.38}$$

corresponding to the specified solid angle, where $p(\theta_n, \phi_n)$ is the probability of the normal $(\theta_n, \phi_n)$ occurring. This area, which when seen directly from above, is projected onto the plane perpendicular to the global normal and the area of that facet is

$$p(\theta_n, \phi_n) \sec\theta_n\, d\Omega_n\ . \tag{4.39}$$

Note that by definition the differential solid angle is $d\Omega_n = \sin\theta_n\, d\theta_n\, d\phi_n$. At reflection, when this area is projected onto the plane perpendicular to the direction of propagation, the area is altered by a secant factor and thus

$$\sec\theta_1\, p(\theta_n, \phi_n) \sec\theta_n\, d\Omega_n\ . \tag{4.40}$$

To match the distribution function for the water surface and utilize the approach of using slope probabilities in the calculations, we define the bottom analytically and take a random sample of the normals to the surface to get the parameters of the distribution, assuming that the surface normals co-vary for this direction-dependent surface. Similar to the definitions in Eqs. 4.21-4.24 but for the underwater bottom surface with the facet normals represented by $\vec{r}_b = (\theta_b, \phi_b)$, the slopes of the tangent lines on the surface at a point on the bottom are given by the partial derivatives of the bottom surface function on the planes parallel to the $x$- and $y$-axes, respectively, and are given by

$$f_{bx} = -\cos\phi_b \tan\theta_b \tag{4.41}$$

and

$$f_{by} = -\sin\phi_b \tan\theta_b \ . \tag{4.42}$$

Let the orientation of the defining sinusoid of the bottom surface be at an azimuth $\phi_{b'}$ from the $x$-axis on the global reference frame. If the orientation of the defining sinusoid of the function $f_b(x, y)$ (Eq. 4.11) is not along the $x$-axis of the global reference frame, i.e., $\phi_{b'} \neq 0$, and instead is given by $f_{b'}(x, y)$ (Eq. 4.13) a rotation (providing similar arguments in Fig. 4.4) is required and the appropriate partial derivatives are

$$f_{b'x} = -\cos(\phi_{b'} - \phi_b) \tan\theta_b \tag{4.43}$$

and

$$f_{b'y} = -\sin(\phi_{b'} - \phi_b) \tan\theta_b \ . \tag{4.44}$$

Note that if $\phi_{b'}$ were aligned with the $y$-axis of the global reference frame then $f_{bx} = f_{b'x}$ and $f_{by} = f_{b'y}$. If the normal vectors of bottom surface facets can be assumed to have a bivariate Gaussian distribution (similar to the argument in He et al. 1991), then the following describes the probability density function of the bottom surface normals:

$$\begin{aligned} p(f_{b'x}, f_{b'y}) = & \frac{1}{2\pi\sigma_{f_{b'x}}\sigma_{f_{b'y}}\sqrt{1-{\rho_{b'}}^2}} \exp\left[-\frac{1}{2\left(1-{\rho_{b'}}^2\right)}\right] \left\{ \frac{\left(f_{b'x}-\mu_{b'x}\right)^2}{{\sigma_{f_{b'x}}}^2} \right. \\ & \left. - \frac{2\rho_{b'}}{\sigma_{f_{b'x}}\sigma_{f_{b'y}}} \left(f_{b'x}-\mu_{b'x}\right)\left(f_{b'y}-\mu_{b'y}\right) + \frac{\left(f_{b'y}-\mu_{b'y}\right)^2}{{\sigma_{f_{b'y}}}^2} \right\} , \end{aligned} \tag{4.45}$$

where $\mu_{b'x}$ and $\mu_{b'y}$ are the means of the $b'x$- and $b'y$-components of the surface normals, respectively, ${\sigma_{f_{b'x}}}^2$ and ${\sigma_{f_{b'y}}}^2$ their variances, and $\rho_{b'}$ the covariance between the two.

Only the specular components of the reflectance of the water surface and the underwater bottom are considered here. This simplifies the general reflectance

problem, the specular component being a special case of diffuse reflectance. For a statistical treatment of a randomly rough surface with both diffuse *and* specular reflectance properties, the reader is referred to a paper by van Ginneken et al. (1998). Most natural surfaces have both specular and diffuse characteristics, being described either as glossy or matte, respectively, depending on whichever component dominates the reflectance pattern. A specular surface reflects light obeying the Fresnel law of reflection: the emergent angle of light in relation to the surface normal is equal to the incident angle but in the opposite direction along the reflection plane. Specular reflection is thought to cause the brightness peaks observed in some surfaces (e.g., Torrance & Sparrow 1967; in particular for the ocean, Plass et al. 1975).

Light transmitted out of the water contributes the greatest in directions where the radiance is the smallest: the direct sun beam dominates the radiances around the specular direction, and skylight contributes the greatest amount when the sun is low in the sky. If indeed a surface has a specular component, the magnitude of the total flux would be half the specular contribution in the direction of specular reflection. The dependence on incidence angle is weaker for more diffuse surfaces. But as we have shown in Part II (Chap. 3), it may be significant depending on the roughness of the surface. Furthermore, as the roughness becomes large and for larger viewing angles, the approach that we take here begins to fall apart and shadowing needs to be taken into account (statistical studies of shadowing by rough surfaces was spurred in the 1960s, e.g., Beckmann 1965, Smith 1967, Torrance & Sparrow 1967, Barrick 1968; some recently, e.g., Fuks 2002). For our model, the underwater angles are within Snell's cone (see, e.g., Sabbah et al. 2006) and the

water surface roughness is not significant although the boundary of the cone is blurred by the ruffles on the water surface (Plass et al. 1975).

## 4.5 Irradiance on a tilted facet from a diffuse sky

The unit vector representing an azimuthal direction $\phi$ from a point $(x_0, y_0)$ (in the $xy$-plane) on a surface is

$$\vec{u} = \cos\phi\,\vec{\mathrm{i}} + \sin\phi\,\vec{\mathrm{j}} + 0\,\vec{\mathrm{k}} \tag{4.46}$$

(see Fig. 4.3, but for a vector of unit length). This vector lies on the $xy$-plane and for convenience we drop the $z$-component and express the vector in component form as

$$\vec{u} = \big\langle \cos\phi, \sin\phi \big\rangle\ . \tag{4.47}$$

The slope of the tangent surface in the direction of $\vec{u}$ at a point on the water surface representing a facet with a local normal $\vec{r}_n$ is simply the directional derivative of the surface function $z = f(x, y)$ in that direction. Using the expressions in Eqs. 4.21 and 4.22 for the partial derivatives of $f$, we find that

$$\begin{aligned} f_u &= \nabla f(x,y) \cdot \vec{u} \\ &= \langle f_x, f_y \rangle \cdot \vec{u} \\ &= \big\langle -\cos\phi_n \tan\theta_n, -\sin\phi_n \tan\theta_n \big\rangle \cdot \big\langle \cos\phi, \sin\phi \big\rangle \\ &= -\cos\phi_n \tan\theta_n \cos\phi - \sin\phi_n \tan\theta_n \sin\phi\,. \end{aligned} \tag{4.48}$$

$\nabla f(x, y)$ is the gradient of the function $f$ and is, by definition, the vector field that points in the direction where there is a maximum increase in $f$ at any given point $(x, y)$. The operation indicated by $(\cdot)$ is the dot product. It can be shown that in

fact $f_x = f_{x'}$ and $f_y = f_{y'}$ (see Eqs. 4.23 and 4.24). Thus the angle of tilt from horizontal of the tangent surface in the direction $\phi$ for all azimuth angles is

$$\alpha = \tan^{-1} f_u \ . \tag{4.49}$$

Given the normalized luminance distribution of the sky $\bar{L}_{\text{sky}}$ (see Appendix B.3) and integrating over all source directions $(\theta_0, \phi_0)$ from the sky dome, we get the illuminance (i.e., irradiance integrated over the visible wavelength range) impinging at a point on the global *horizontal* surface:

$$E_{\text{sky}} = \int_0^{2\pi} \int_0^{\frac{\pi}{2}} \bar{L}_{\text{sky}}(\theta_0, \phi_0) \cos\theta_0 \sin\theta_0 \ d\theta_0 \, d\phi_0 \ . \tag{4.50}$$

The area of sky *projected* onto the unit hemisphere above the surface facet and visible to the tilted facet is given by

$$\text{Area}_{\text{sky}}(\theta_0, \phi_0) = \int_0^{2\pi} \int_0^{G(\phi_0)} \sin\theta_0 \ d\theta_0 \ d\phi_0 \tag{4.51}$$

where

$$G(\phi_0) = \frac{\pi}{2} - \alpha \tag{4.52}$$

represents the boundary in terms of the zenith angle of the visible part of the sky.

A tilted facet with a normal $(\theta_n, \phi_n)$ only sees a portion of the sky dome and the irradiance impinging on it is reduced to

$$E^*_{\text{sky}}(\theta_0, \phi_0) = \int_0^{2\pi} \int_0^{G(\phi_0)} \bar{L}_{\text{sky}}(\theta_0, \phi_0) \cos\chi(\theta_0, \phi_0) \sin\theta_0 \ d\theta_0 \ d\phi_0 \tag{4.53}$$

where

$$\begin{aligned} \chi(\theta_0, \phi_0) = \cos^{-1} \Big[ & \sin\theta_n \cos\phi_n \sin\theta_0 \cos\phi_0 \\ & + \sin\theta_n \sin\phi_n \sin\theta_0 \sin\phi_0 + \cos\theta_n \cos\theta_0 \Big] \end{aligned} \tag{4.54}$$

is the incidence angle of light from the facet normal as measured on the reflection or transmission plane. The same arguments apply to the underwater bottom surface seeing a portion of an "underwater sky" dome.

In comparison, the irradiance from the sun given a black sky impinging at a point on the surface is

$$E_{\text{sun}}(\theta_s, \phi_s) = \int_0^{2\pi} \int_0^{\frac{\pi}{2}} L_{\text{sun}}\big(\theta_s, \phi_s\big) \cos\theta_s \, \delta\big(\theta_0 - \theta_s\big) \, \delta\big(\phi_0 - \phi_s\big) \, d\theta_0 \, d\phi_0 \ , \quad (4.55)$$

where the Dirac delta function (e.g., Mobley 1994) is defined here as

$$\delta\big(\theta_0 - \theta_s\big) \, \delta\big(\phi_0 - \phi_s\big) \equiv 0, \quad \text{if} \quad \theta_0 \neq \theta_s \quad \text{and} \quad \phi_0 \neq \phi_s \ . \quad (4.56)$$

An approximation of the delta function by a Gaussian expression is used by Meister et al. (1998).

## 4.6 Model description

The coordinate system used in this chapter is described; it includes the successive determination of the scattering angles as used in the model. This approach mainly follows Mullamaa (1964), see also Kattawar & Adams (1989) and Yang et al. (2003). It is a "forward" model in that the light paths are followed from the source to the detector, except the scattering angles from the bottom that allow a full hemisphere of out-of-water emergent directions (more later). As such, the surface model is deterministic in nature: as the incident and scattered directions are specified throughout the system the orientation of the local normals both of the water and underwater surfaces are fully determined (similar to that in Priest & Germer 2000).

### 4.6.1 The coordinate system and solid angles

Let the angle pair $(\theta_s, \phi_s)$ be the spherical coordinates representing the location of the sun in the sky (see Fig. 4.5), $\theta_s$ being its zenith distance and $\phi_s$ its azimuth from the axis perpendicular to the direction of the prevailing wind direction. The sun (or source) direction is also represented by the unit vector $\vec{r}_s$ centered on the differential solid angle $d\Omega_s$. Some of the incident light is reflected off the water surface in directions $\vec{r}_1 \rightarrow (\theta_1, \phi_1)$ while some of it is transmitted through the water surface in directions $\vec{r}_2 \rightarrow (\theta_2, \phi_2)$. According to the law of reflection, we know that the angle of reflection equals the angle of incidence: $\theta_s = \theta_1$ but in the opposite azimuthal direction. From Snell's law, the angle of refraction is

$$\theta_2 = \sin^{-1}\left(\frac{n_1}{n_2}\sin\theta_1\right) , \tag{4.57}$$

lying on the scattering plane that is defined by either the incident, reflected or transmitted directions with the local surface normal, $\vec{r}_n$.

### 4.6.2 Determining the directions in the system: reflection

In a simple model, where internal reflections, multiple reflections, and absorption by the air and the water media are ignored, there are only four scattering events of interest. Fig. 4.6 is a sketch of the air-water-bottom system. The term "scattering" is used here to represent either reflection or transmission. Light is incident on the water surface in the direction $\vec{r}_0$ (we further distinguish the subscript 0 representing any point in the sky while $s$ denoting the direction of the sun at a point in the sky). The first event in the model is reflection upward from the water surface along the direction $\vec{r}_1$; the second is transmission downward through the air-water interface along $\vec{r}_2$; the third is the reflection back upward through the water along

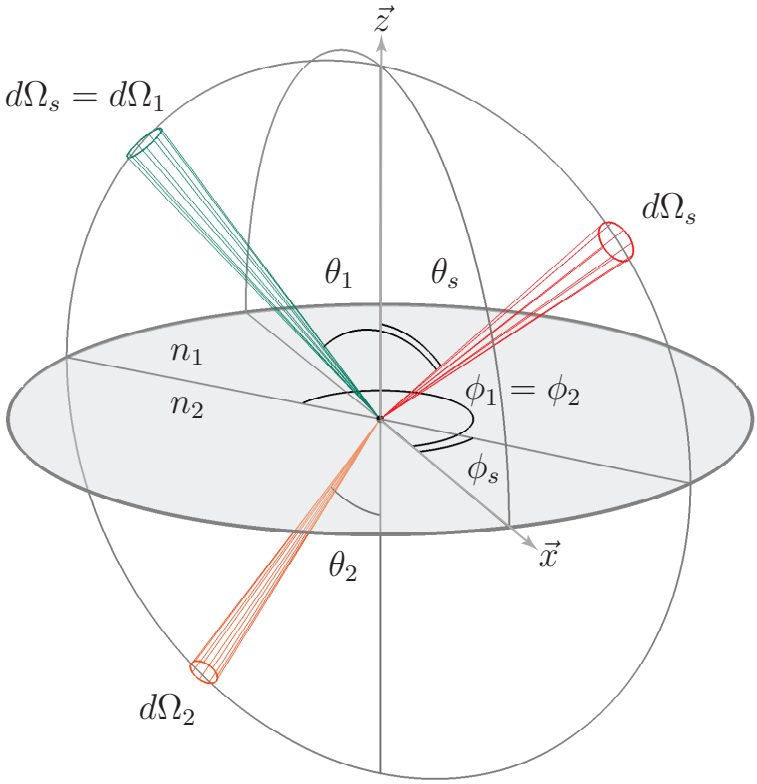


Figure 4.5: Coordinate system for water surface reflection and transmission. In this diagram we show a surface that is flat to simplify the descriptions of the vectors, angles and solid angles. The normal vector at a point on the surface points directly straight up so that it is parallel to the global normal, $\vec{z}$. The sun location is in the direction $(\theta_s, \phi_s)$ and subtends a solid angle $d\Omega_s$ on the surface. The reflection direction is oriented away from the sun at an azimuth $\phi_1 = \phi_s + \pi$. Because there is no change in the index of refraction $n_1$ at reflection, the solid angle at reflection is $d\Omega_1 = d\Omega_s$. At transmission it becomes $d\Omega_2$ given a medium with index of refraction $n_2$. By convention the zenith angles are measured from either the positive or negative $z$-axis. (Template for sketch borrowed from Hébert 2006.)

$\vec{r}_3$; and finally the transmission upward through the water-air interface along $\vec{r}_4$. The indices of refraction of air, water and the bottom surface are denoted by $n_1$, $n_2$ and $n_3$, respectively.

The direction vectors are specified in relation to a global normal denoted by $\vec{z}$, which is oriented toward zenith at any point in the system. The surface facet normals along the water surface and underwater bottom are denoted by $\vec{r}_n$ or $\vec{r}_w$ and $\vec{r}_b$ (Fig. 4.6), respectively.

To aide in determining the distribution of the reflected and transmitted light, we partition the upper and lower unit hemispheres of a point of interest by incrementing the polar angles. We employ vector calculus whenever possible and only use spherical trigonometric formulae when these do not cause ambiguities in expressing explicit vector directions.

The model is set up so that the initial inputs include the specification of a global normal, an incident angle and a grid representing reflection directions in the "sky". Given these directions and from the law of reflection, we know that the angle between the incidence and reflection directions (Fig. 4.7), $\vec{r}_s$ and $\vec{r}_1$, respectively, is $2\chi_1$. The incidence angle in the scattering plane is

$$\chi_1 = \frac{1}{2}\cos^{-1}\left[\frac{\vec{r}_s \cdot \vec{r}_1}{\|\vec{r}_s\|\|\vec{r}_1\|}\right] . \tag{4.58}$$

From Snell's law, $n_1 \sin\chi_1 = n_2 \sin\chi_2$, so the transmission direction is

$$\chi_2 = \sin^{-1}\left[\frac{n_1}{n_2}\sin\chi_1\right] , \tag{4.59}$$

where $n_1 = 1.0$ is the index of refraction of the first medium, in this case air, and $n_2 = 1.338$ is that of the second medium, water, and $n_3 \approx 1.5$ for sand (e.g., Clark et al. 2004).

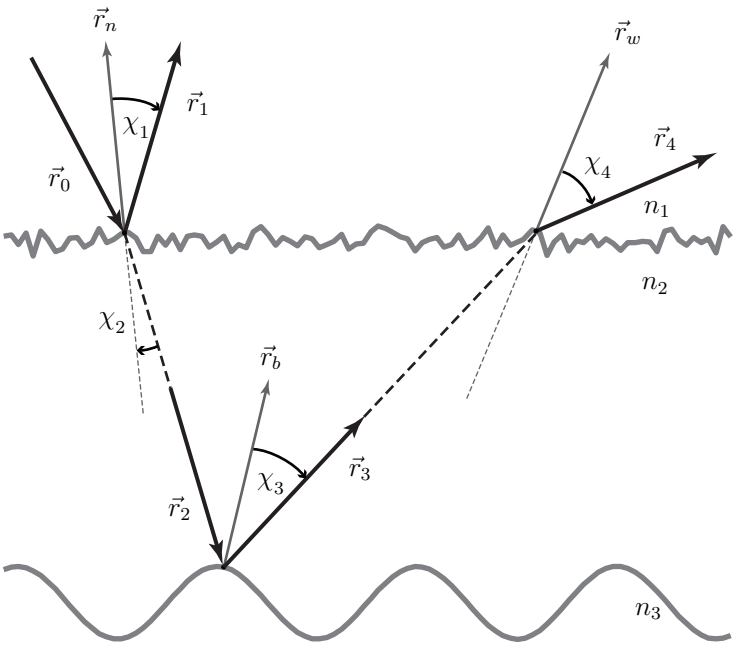


Figure 4.6: Sketch of reflection and transmission events in the model. For illustration, the diagram presents the light paths in two dimensions as it traverses the air-water-bottom system, even when the calculations are based on three-dimensional surfaces taken at points in space with varying slope conditions. The local surface normals are indicated by $\vec{r}_n$, $\vec{r}_b$ and $\vec{r}_w$ and the indices of refraction are $n_1$ for air, $n_2$ for water, and $n_3$ for the bottom surface. Vectors of unit length represent the directions of light propagation: $\vec{r}_0$ for incoming light from a point in the sky, $\vec{r}_1$ for light being reflected off the water surface, $\vec{r}_2$ transmitted through the water surface, $\vec{r}_3$ reflected off the bottom, and $\vec{r}_4$ transmitted back out of the water. The $\chi$'s indicate the angles these directions make in relation to the surface normals at the points of interaction ($\theta$'s are used to indicate angles relative to the global normal in the meridian plane, see Fig. 4.5.).

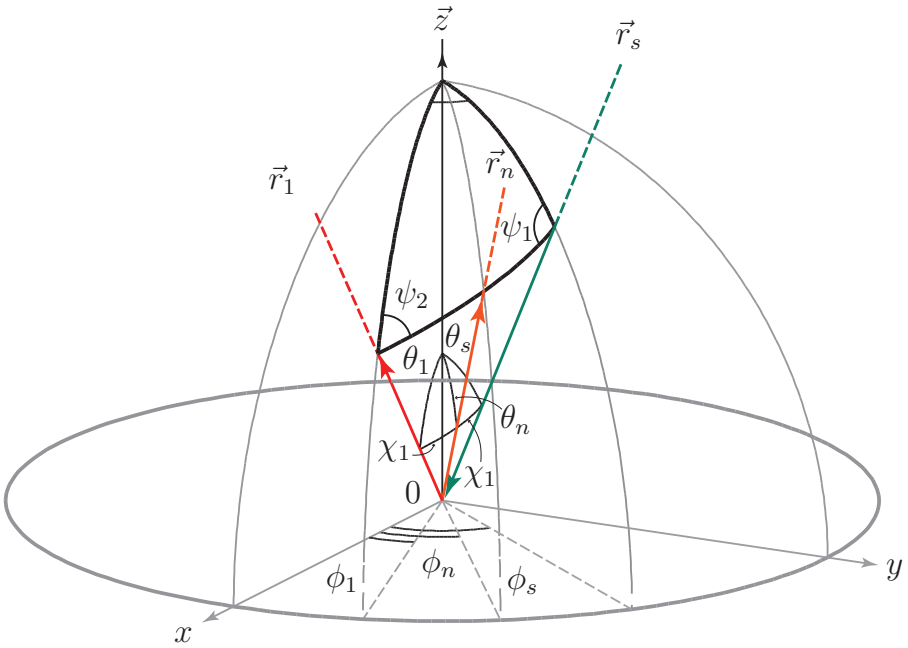


Figure 4.7: Incidence angle in scattering plane, $\chi_1$. The directional vectors $\vec{r}$ occur within a unit hemisphere centered around the global normal, $\vec{z}$, with the vector tips tracing the surface of the hemisphere. In this figure the vectors are lengthened for clarity. The scattering plane is defined by the incidence and normal vectors, $\vec{r}_s$ and $\vec{r}_n$, respectively. From the law of reflection the vector $\vec{r}_1$ lies on the scattering plane. (Template for drawing borrowed from Mullamaa 1964.)

Specifying an incident direction and partitioning the sky into reflection directions the facet normals can be determined for each of these directions. To do this, we use the take the cross product of the vectors, thus

$$\frac{\vec{r}_s \times \vec{r}_n}{\left\|\vec{r}_s\right\|\left\|\vec{r}_n\right\| \sin\chi_1} = \frac{\vec{r}_s \times \vec{r}_1}{\left\|\vec{r}_s\right\|\left\|\vec{r}_1\right\| \sin 2\chi_1} \ . \tag{4.60}$$

Recalling that the direction vectors are of unit length, and using an extension of the vector triple product (see Appendix A.4):

$$\frac{1}{\sin\chi_1}\Big[\vec{r}_1 \times \big(\vec{r}_s \times \vec{r}_n\big)\Big] = \frac{1}{\sin 2\chi_1}\Big[\vec{r}_1 \times \big(\vec{r}_s \times \vec{r}_1\big)\Big] \tag{4.61}$$

The rest determines $\vec{r}_n$:

$$\sin 2\chi_1\Big[\big(\vec{r}_1 \cdot \vec{r}_n\big)\vec{r}_s - \big(\vec{r}_1 \cdot \vec{r}_s\big)\vec{r}_n\Big] = \sin\chi_1\Big[\big(\vec{r}_1 \cdot \vec{r}_1\big)\vec{r}_s - \big(\vec{r}_1 \cdot \vec{r}_s\big)\vec{r}_1\Big] \tag{4.62}$$

$$\Big[\sin 2\chi_1 \cos\chi_1\Big]\vec{r}_s - \Big[\sin 2\chi_1 \cos 2\chi_1\Big]\vec{r}_n = \Big[\sin\chi_1\Big]\vec{r}_s - \Big[\sin\chi_1 \cos 2\chi_1\Big]\vec{r}_1 \tag{4.63}$$

$$\vec{r}_n = \frac{\big(\sin 2\chi_1 \cos\chi_1\big)\vec{r}_s - \big(\sin\chi_1\big)\vec{r}_s + \big(\sin\chi_1 \cos 2\chi_1\big)\vec{r}_1}{\sin 2\chi_1 \cos 2\chi_1} \ . \tag{4.64}$$

With this definition in mind, the angle between the scattering plane and the plane defined by the incidence direction and the global normal (Fig. 4.8) is given by

$$\psi_1 = \cos^{-1}\left[\frac{(\vec{z} - \vec{r}_s) \cdot (\vec{r}_1 - \vec{r}_s)}{\left\|\vec{z} - \vec{r}_s\right\|\left\|\vec{r}_1 - \vec{r}_s\right\|}\right] \ . \tag{4.65}$$

Similarly, the angle between the scattering plane and the meridional plane of the reflection direction (Fig. 4.9, also Fig. 4.7) is

$$\psi_2 = \cos^{-1}\left[\frac{(\vec{z} - \vec{r}_1) \cdot (\vec{r}_n - \vec{r}_1)}{\left\|\vec{z} - \vec{r}_1\right\|\left\|\vec{r}_n - \vec{r}_1\right\|}\right] \ . \tag{4.66}$$

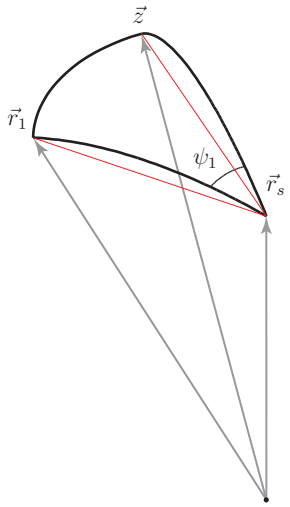


Figure 4.8: Angle between the incidence meridional plane and the scattering plane, $\psi_1$.

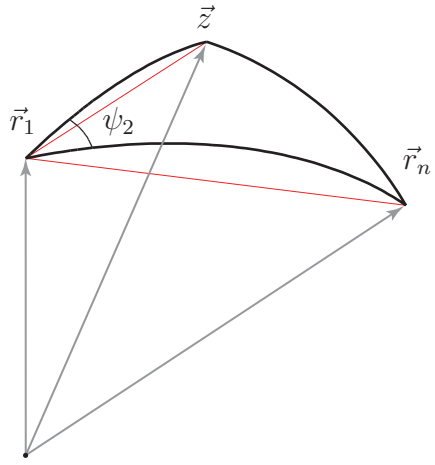


Figure 4.9: Angle between scattering plane and reflection meridional plane, $\psi_2$.

### 4.6.3 Determining the directions in the system: transmission

Given the direction of the sun and specifying underwater transmission directions, the angle between the incidence and transmission directions, $\vec{r}_s$ and $\vec{r}_2$, respectively, in the scattering plane (Fig. 4.10) is determined by

$$\chi_{12} = \cos^{-1}\left[\frac{\vec{r}_2 \cdot \vec{r}_s}{\left\|\vec{r}_2\right\|\left\|\vec{r}_s\right\|}\right] . \tag{4.67}$$

We can find a vector that lies on the meridional plane by determining the angle between the vectors $\vec{z} - \vec{r}_2$ and $\vec{r}_s - \vec{r}_2$, where $\vec{z} = \langle 0, 0, 1\rangle$. The distance between the two planes (Fig. 4.11) is then

$$\psi_3 = \cos^{-1}\left[\frac{(\vec{z} - \vec{r}_2) \cdot (\vec{r}_s - \vec{r}_2)}{\left\|\vec{z} - \vec{r}_2\right\|\left\|\vec{r}_s - \vec{r}_2\right\|}\right] \tag{4.68}$$

From Fig. 4.10 we know that

$$\chi_{12} = \chi_1 - \chi_2 \tag{4.69}$$

and so

$$\chi_1 - \chi_{12} = \sin^{-1}\left[\frac{n_1}{n_2}\sin\chi_1\right] \tag{4.70}$$

$$\chi_{12} = \chi_1 - \sin^{-1}\left[\frac{n_1}{n_2}\sin\chi_1\right] . \tag{4.71}$$

Rearranging as follows to solve for $\chi_1$:

$$\sin^{-1}\left[\frac{n_1}{n_2}\sin\chi_1\right] = \chi_1 - \chi_{12} \tag{4.72}$$

$$\frac{n_1}{n_2}\sin\chi_1 = \sin\left[\chi_1 - \chi_{12}\right] \tag{4.73}$$

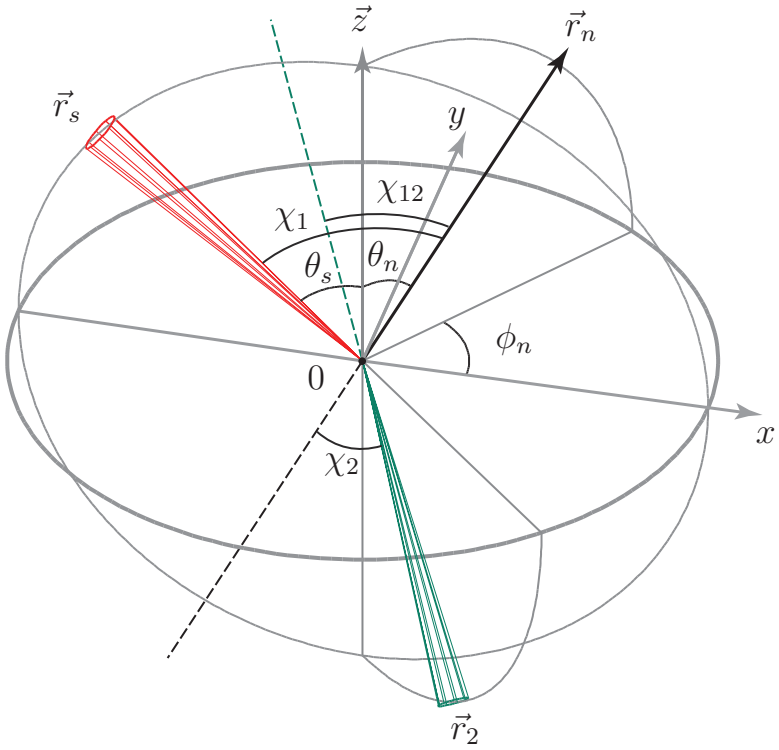


Figure 4.10: Defining $\chi_{12}$. Let the incidence direction be $\vec{r}_s$ and a local normal be $\vec{r}_n$ in the upper hemisphere (defined by the positive $\vec{z}$ direction). The angle between $\vec{r}_s$ and $\vec{r}_n$ is denoted by $\chi_1$. Transmitted light travels in the lower hemisphere in the direction $\vec{r}_2$ making an angle $\chi_2$ from the local normal $\vec{r}_n$ (in the negative direction). For convenience, however, the transmission direction is extended (in the opposite direction into the upper hemisphere), which makes an angle $\chi_{12} = \chi_1 - \chi_2$ from the local normal, $\vec{r}_n$. (Sketch revised from Ivanov & Toporets 1956.)

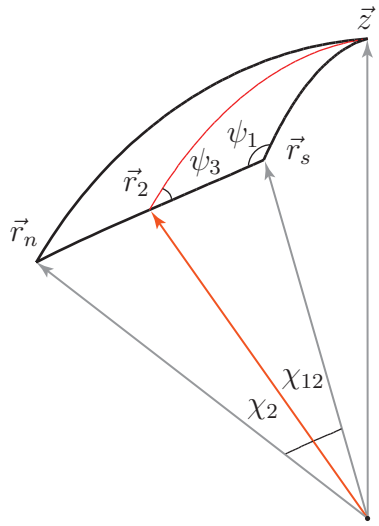


Figure 4.11: Determining the angle $\psi_3$.

$$\frac{n_1}{n_2}\sin\chi_1 = \sin\chi_1\cos\chi_{12} - \cos\chi_1\sin\chi_{12} \tag{4.74}$$

$$\cos\chi_1\sin\chi_{12} = \sin\chi_1\cos\chi_{12} - \frac{n_1}{n_2}\sin\chi_1 \tag{4.75}$$

$$\cos\chi_1\sin\chi_{12} = \sin\chi_1\left[\cos\chi_{12} - \frac{n_1}{n_2}\right] \tag{4.76}$$

$$\tan\chi_1 = \frac{\sin\chi_{12}}{\left[\dfrac{n_2\cos\chi_{12} - n_1}{n_2}\right]} \tag{4.77}$$

$$\chi_1 = \tan^{-1}\left[\frac{n_2\sin\chi_{12}}{n_2\cos\chi_{12} - n_1}\right] . \tag{4.78}$$

Furthermore, from Snell's law we can determine the transmission directions in the scattering plane:

$$\chi_2 = \sin^{-1}\left[\frac{n_1}{n_2}\sin\chi_1\right] . \tag{4.79}$$

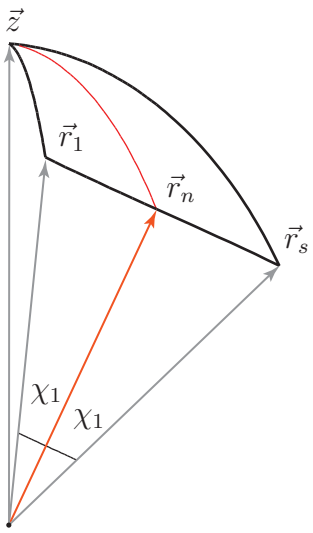


Figure 4.12: Illustrating $2\chi_1$ (sometimes referred to as the "scattering angle") and using it for the determination of $\chi_1$.

To determine the facet normals of the water surface, we use the unit normal vector of the plane defined by the incident and surface normal vectors and equate this with the unit normal vector of the plane defined by the transmitted and the surface normal vectors, respectively (Fig. 4.12, also Fig. 4.7):

$$\frac{\vec{r}_n \times \vec{r}_s}{\left\|\vec{r}_n\right\|\left\|\vec{r}_s\right\| \sin\chi_1} = \frac{\vec{r}_n \times \vec{r}_2}{\left\|\vec{r}_n\right\|\left\|\vec{r}_2\right\| \sin\chi_2} \,. \tag{4.80}$$

The direction vectors are of unit length, thus we have

$$\frac{1}{\sin\chi_1}\left[\vec{r}_s \times (\vec{r}_n \times \vec{r}_s)\right] = \frac{1}{\sin\chi_2}\left[\vec{r}_s \times (\vec{r}_n \times \vec{r}_2)\right] \,. \tag{4.81}$$

The rest determines $\vec{r}_n$:

$$\sin\chi_2\left[\,(\vec{r}_s \cdot \vec{r}_s)\,\vec{r}_n - (\vec{r}_s \cdot \vec{r}_n)\,\vec{r}_s\right] = \sin\chi_1\left[\,(\vec{r}_s \cdot \vec{r}_2)\,\vec{r}_n - (\vec{r}_s \cdot \vec{r}_n)\,\vec{r}_2\right] \tag{4.82}$$

$$\left(\sin\chi_2\left\|\vec{r}_s\right\|^2\right)\vec{r}_n - \left(\sin\chi_2\cos\chi_1\right)\vec{r}_s = \left[\sin\chi_1\cos\left(\chi_1 - \chi_2\right)\right]\vec{r}_n - \left(\sin\chi_1\cos\chi_1\right)\vec{r}_2 \tag{4.83}$$

$$\big(\sin\chi_2\big\|\vec{r}_s\big\|^2\big)\vec{r}_n - \big[\sin\chi_1\cos\left(\chi_1-\chi_2\right)\big]\vec{r}_n = \big(\sin\chi_2\cos\chi_1\big)\vec{r}_s - \big(\sin\chi_1\cos\chi_1\big)\vec{r}_2 \tag{4.84}$$

$$\vec{r}_n = \frac{\big(\sin\chi_2\cos\chi_1\big)\vec{r}_s - \big(\sin\chi_1\cos\chi_1\big)\vec{r}_2}{\sin\chi_2\big\|\vec{r}_s\big\|^2 - \sin\chi_2\cos\left(\chi_1-\chi_2\right)} \,. \tag{4.85}$$

Similarly, as above (Eq. 4.65), we determine the distance between the scattering and meridional incidence planes. The vector $\vec{z}-\vec{r}_s$ lies on the meridional plane and $\vec{r}_2-\vec{r}_s$ on the scattering plane. The distance between the two planes is

$$\psi_1 = \cos^{-1}\left[\frac{(\vec{z}-\vec{r}_s)\cdot(\vec{r}_2-\vec{r}_s)}{\big\|\vec{z}-\vec{r}_s\big\|\big\|\vec{r}_2-\vec{r}_s\big\|}\right] \tag{4.86}$$

In all the cases considered here, we limit the transmission direction to within Snell's cone (as if the water surface were flat) where it has been shown experimentally by Aas & Højerslev (1999) that the most significant variations in the downward radiance distribution in the ocean occurs within this cone; outside of the cone it decreases with increasing zenith angle. We recognize, however, that the boundary of the cone may be significantly blurred by increased water surface roughness (e.g., Plass et al. 1975).

## 4.7 Stokes parameters and the Mueller matrix

The full hemispherical treatment of surface reflectance is facilitated by the Mueller matrix approach, which necessarily requires the inclusion and handling of the polarization states of light. Using vector calculus in representing the magnitudes and directions of scattered light is a convenient way of keeping track of the transformations as the light is transferred within the system. Through the Stokes parameters, a four-element vector containing the intensity and polarization states of the light

field at any given moment is fully described. A Mueller matrix is the quantity that affects the Stokes parameters when an interaction occurs. It results in another Stokes vector and includes the change in the polarization state of the light.

### 4.7.1 Measuring light: as a vector

To take into account the intensity and polarization state of light, we employ the Stokes parameters (proof found in Chandrasekhar 1960, see also Goldstein 2003, Chap. 4). In general they are given by

$$\vec{S}(\vec{r},0) = \begin{bmatrix} I \\ Q \\ U \\ V \end{bmatrix} \tag{4.87}$$

where the "0" indicates that the direction of propagation is referenced on the meridional plane defined by the vector $\vec{r}$ and the global normal. $I$ represents the radiance (also denoted as $L$) of the light (see, e.g., Kattawar & Adams 1989), $\sqrt{Q^2+U^2+V^2}/I$ the degree of polarization of the light,

$$\frac{Q}{|Q|}\frac{\sqrt{Q^2+U^2}}{I} \tag{4.88}$$

the degree of linear polarization (e.g., Barkov et al. 1979, Eq. 6), and $V/I$ the degree of circular polarization, all in the same units. The Stokes parameters are related such that:

$$I^2 \geq Q^2 + U^2 + V^2 \tag{4.89}$$

and the preferential azimuth of the (polarization) vibration ellipse, $\psi$, of the light is determined from

$$\tan 2\psi = \frac{U}{Q}\,. \tag{4.90}$$

Let the Stokes parameters of the incident light be

$$\vec{S}(\vec{r}_s, 0) = \begin{bmatrix} I_s \\ Q_s \\ U_s \\ V_s \end{bmatrix} . \tag{4.91}$$

If the incident light from the sky can be assumed to be randomly polarized, then $Q = U = V = 0$ and the input Stokes parameters for a diffuse sky are

$$\vec{S}(\vec{r}_s, 0) = \begin{bmatrix} \bar{L}_{\text{sky}} \\ 0 \\ 0 \\ 0 \end{bmatrix} \tag{4.92}$$

(see Appendix B.3), or for the sun as a point source is

$$\vec{S}(\vec{r}_s, 0) = \begin{bmatrix} \frac{1}{\varepsilon^2} \\ 0 \\ 0 \\ 0 \end{bmatrix} . \tag{4.93}$$

Relative errors of 40% to the radiance reflectance involving the assumption of an unpolarized sky have been approximated by Aas & Høkedal (1999) and is expected to be greatest close to Brewster's angle. The errors are reduced to 2-5% for irradiance reflectance, however (Høkedal & Aas 1998, as quoted in Aas & Høkedal 1999). To include the linear polarization of skylight, the approach by Matchko & Gerhart (2005) is adapted here so that the normalized Stokes vector of the incoming light

is

$$\vec{S}(\vec{r}_0, 0) = \begin{bmatrix} 1 \\ P\cos 2\psi \\ P\sin 2\psi \\ 0 \end{bmatrix} . \tag{4.94}$$

$P$ is the polarization given by (e.g., Gershun & Popov 1955, Born & Wolf 1999)

$$P = \frac{\sin^2 \chi_1}{1 + \cos^2 \chi_1} , \tag{4.95}$$

where $\chi_1$ is the reflection angle referenced on the scattering plane, and

$$\psi = \cos^{-1} \frac{\cos\theta_0 \sin\theta_1 - \cos\theta_1 \sin\theta_0 \cos(\phi_1 - \phi_0)}{\pm\sqrt{1 - \left[\cos\theta_0 \cos\theta_1 + \sin\theta_1 \sin\theta_0 \cos(\phi_1 - \phi_0)\right]^2}} , \tag{4.96}$$

is the orientation of the polarization ellipse, which gives $\psi$ as would be calculated from Eq. 4.90 but instead is dependent on the directions of incidence and observation, denoted as $(\theta_0, \phi_0)$ and $(\theta_1, \phi_1)$, respectively.

### 4.7.2 Affecting light: an inherent property of a surface

The index of refraction is an inherent optical property of a surface or the surface material. It determines the amount of light reflected, transmitted and absorbed by the surface and the angle at which light is redirected through its interface. Given an incidence direction, the way a surface affects light is determined by the values of its Mueller matrix that are dependent on the index of refraction.

The Mueller matrix of a material describes how light interacts with that material; it describes the relation between the incident Stokes parameters and the scattered Stokes parameters (foundational work for the calculus is credited to a series of publications by Jones 1941a, Hurwitz & Jones 1941, Jones 1941b, 1942,

1947a,b, 1948, 1956). In the case of scattering by reflection the matrix is given by

$$D_r = \begin{bmatrix} \alpha+\eta & \alpha-\eta & 0 & 0 \\ \alpha-\eta & \alpha+\eta & 0 & 0 \\ 0 & 0 & \gamma_{\mathrm{Re}} & 0 \\ 0 & 0 & 0 & \gamma_{\mathrm{Re}} \end{bmatrix} , \tag{4.97}$$

where

$$\alpha = \frac{1}{2}\left[\frac{\tan(\chi_i - \chi_t)}{\tan(\chi_i + \chi_t)}\right]^2 \tag{4.98}$$

$$\eta = \frac{1}{2}\left[\frac{\sin(\chi_i - \chi_t)}{\sin(\chi_i + \chi_t)}\right]^2 \tag{4.99}$$

$$\gamma_{\mathrm{Re}} = -\frac{\tan(\chi_i - \chi_t)\sin(\chi_i - \chi_t)}{\tan(\chi_i + \chi_t)\sin(\chi_i + \chi_t)} . \tag{4.100}$$

$\chi_i$ and $\chi_t$ are the reflection and transmission angles, respectively, with respect to the local surface normal $\vec{r}_n$ (all referenced and lying on the scattering plane). $2\alpha$ and $2\eta$ give the Fresnel equations for the light reflected at the sea surface polarized in the horizontal and vertical planes of the electric vector, respectively (e.g., Hulburt 1934), thus the reflectivity of the sea surface for randomly polarized incident light is $\alpha + \eta$. The transmission Mueller matrix (following the notation used by Kattawar & Adams 1989, typographical error corrected here) is:

$$D_t = \frac{1}{2}\frac{n_t \cos\chi_t}{n_i \cos\chi_i} \begin{bmatrix} \alpha'+\eta' & \alpha'-\eta' & 0 & 0 \\ \alpha'-\eta' & \alpha'+\eta' & 0 & 0 \\ 0 & 0 & \gamma'_{\mathrm{Re}} & 0 \\ 0 & 0 & 0 & \gamma'_{\mathrm{Re}} \end{bmatrix} \tag{4.101}$$

where

$$\alpha' = \frac{1}{2}\left[\frac{2\sin\chi_t \cos\chi_i}{\sin(\chi_i + \chi_t)\cos(\chi_i - \chi_t)}\right]^2 \tag{4.102}$$

$$\eta' = \frac{1}{2}\left[\frac{2\sin\chi_t\cos\chi_i}{\sin\left(\chi_i+\chi_t\right)}\right]^2 \tag{4.103}$$

$$\gamma'_{\mathrm{Re}} = \frac{4\sin^2\chi_t\cos^2\chi_i}{\sin^2\left(\chi_i+\chi_t\right)\cos^2\left(\chi_i-\chi_t\right)}\ . \tag{4.104}$$

### 4.7.3 Planes of reference: rotating bases

The transformation matrix that rotates the scattering plane to align with the meridional plane of incidence, reflection or transmission at an angle $\psi_i$, thus transforming the Stokes parameters, is given by

$$H(\psi_i) = \begin{bmatrix} 1 & 0 & 0 & 0 \\ 0 & \cos 2\psi_i & \sin 2\psi_i & 0 \\ 0 & -\sin 2\psi_i & \cos 2\psi_i & 0 \\ 0 & 0 & 0 & 1 \end{bmatrix}\ . \tag{4.105}$$

## 4.8 The transfer equations

As described in Fig. 4.6, this section determines the Stokes parameters of the light as it is transferred in the system, following the scattering events in order.

### 4.8.1 Event 1: Reflection off the water surface

The incident light field is most easily described in reference to a global coordinate system. However, when considering the interaction of light with the water surface, the natural coordinate system is determined by the direction of the incident light and the normal to the water surface at a particular point. Thus, a transformation is required to track a beam of light from one coordinate system to the other.

The source Stokes parameters in the meridional plane of incidence is given by $\vec{S}(\vec{r}_s, 0)$ for the sun or $\vec{S}(\vec{r}_0, 0)$ for any point in the sky. Recall that the"0" indicates that the Stokes vector is referenced on the meridional plane defined by the vector $\vec{r}_s$ (or $\vec{r}_0$) and the global normal, $\vec{z}$. In order to reference the Stokes vector on the scattering plane, the original basis vectors are transformed by $H(\psi_1)$ (Eq. 4.105), where $\psi_1$ is the angle between the scattering and meridional planes (Fig. 4.7). On the scattering plane, the optical property of the surface affects light as described by the reflection Mueller matrix of the water surface. For the current event we denote this matrix $D_1$, using Eq. 4.97 and assign as variables $\chi_i = \chi_s$ (or $\chi_0$) and $\chi_t = \chi_2$. For convenience, the reference frame of the viewer is oriented along the reflection meridian. The resulting light is measured in reference to the reflection meridional plane and is rotated by $H(-\psi_2)$ (Eq. 4.105; the negative angle referring to a reverse rotation using the right-hand rule from meridian to scattering plane). The *effective* reflection Mueller matrix for every point on the surface acting on the incident light $\vec{S}(\vec{r}_s, 0)$ is

$$\cos\chi_1 H(-\psi_2)\, D_1\, H(\psi_1)\ . \tag{4.106}$$

The cosine factor is a result of changing the reference solid angle from $\Omega_1$ to $\Omega_n$: it can be shown from Snell's law (also Straubel's invariant, see Appendix A.3) that

$$d\Omega_n = \cos\chi_1\, d\Omega_1\ . \tag{4.107}$$

The resulting reflected light emerging in the direction $\vec{r}_1$ (Fig. 4.7) is described by the Stokes parameters (recall that this is a four-element vector):

$$\vec{S}(\vec{r}_1, 0) = \sec\theta_1 \int_{\Omega_n} p(\theta_n, \phi_n) \sec\theta_n \cos\chi_1\, H(-\psi_2) D_1 H(\psi_1) \vec{S}(\vec{r}_s, 0)\, d\Omega_n\ , \tag{4.108}$$

where $p(\theta_n, \phi_n)$ is the probability density function of the normals to the water surface and the secant factors are effects of the area projections of the facets

(Eqs. 4.38-4.40) onto the direction of the facet normal, $\theta_n$, and the reflection direction angle, $\theta_1$. The relevant integral in Eq. 4.108 is

$$\int_{\Omega_n} p(\theta_n, \phi_n) \sec\theta_n \, d\Omega_n(\theta_n, \phi_n) \; . \tag{4.109}$$

Let the partial derivatives in the $x$- and $y$-directions be

$$g(\theta_n, \phi_n) = f_{x'} = -\cos(\phi_n - \phi_w) \tan\theta_n \tag{4.110}$$

and

$$h(\theta_n, \phi_n) = f_{y'} = -\sin(\phi_n - \phi_w) \tan\theta_n \; , \tag{4.111}$$

respectively, also Eqs. 4.23-4.24. The probability density function of the surface normals is given in Eq. 4.25 in terms of $(f_{x'}, f_{y'})$. The transformation of the coordinate systems between $(\theta_n, \phi_n)$ and $(f_{x'}, f_{y'})$ results in Eq. 4.109 becoming

$$\int_{\Omega_n} p(\theta_n, \phi_n) \sec\theta_n \, d\Omega_n(\theta_n, \phi_n) = \int_{\Omega_n} p\big(g(\theta_n, \phi_n), h(\theta_n, \phi_n)\big) \left| \frac{\partial(f_{x'}, f_{y'})}{\partial(\theta_n, \phi_n)} \right| \sec\theta_n \, d\Omega_n(\theta_n, \phi_n) \; . \tag{4.112}$$

The Jacobian determinant of the transformation is equal to

$$\left| \frac{\partial(f_{x'}, f_{y'})}{\partial(\theta_n, \phi_n)} \right| = \begin{vmatrix} \dfrac{\partial f_{x'}}{\partial\theta_n} & \dfrac{\partial f_{x'}}{\partial\phi_n} \\ \dfrac{\partial f_{y'}}{\partial\theta_n} & \dfrac{\partial f_{y'}}{\partial\phi_n} \end{vmatrix} = \frac{\partial f_{x'}}{\partial\theta_n}\frac{\partial f_{y'}}{\partial\phi_n} - \frac{\partial f_{y'}}{\partial\theta_n}\frac{\partial f_{x'}}{\partial\phi_n} = \frac{\sin\theta_n}{\cos^3\theta_n} \; , \tag{4.113}$$

and Eq. 4.109 becomes

$$\vec{S}(\vec{r}_1, 0) = \sec\theta_1 \int_{\Omega_n} p\big(g(\theta_n, \phi_n), h(\theta_n, \phi_n)\big) \frac{\sin\theta_n}{\cos^3\theta_n} \cos\chi_1 \, H(-\psi_2) \, D_1 \, H(\psi_1) \, \vec{S}(\vec{r}_s, 0) \, \sec\theta_n \, d\Omega_n(\theta_n, \phi_n) \; . \tag{4.114}$$

The integral area of sky (or the area of the sun's disk) that contributes to the incident irradiance at a point on the surface with normal $(\theta_n, \phi_n)$ is

$$\int_{\Omega_n} d\Omega_n(\theta_n, \phi_n) = \frac{\cos^3\theta_n}{\sin\theta_n} \frac{1}{4} \, \text{Area}_{\text{sky}} \, \sec\chi_1 \; . \tag{4.115}$$

Note that this is an approximation, the arguments of which are presented in Appendix C.2. Furthermore, assuming that because the normal to a surface facet is, by definition, indeed the center of the facet, and the mean value of any change in the location of the source point on the source disk can be assumed to be at the facet center then using the Mean Value Theorem (see Appendix A.2) an approximation of the Stokes parameters of the reflected light from the water surface, Eq. 4.114, is

$$\vec{S}'(\vec{r}_1, 0) = \sec\theta_1 \; p\big(g(\theta_n, \phi_n), h(\theta_n, \phi_n)\big) \sec\theta_n \\ H(-\psi_2)\, D_1\, H(\psi_1)\, \vec{S}(\vec{r}_s, 0)\, \frac{1}{4}\, \mathrm{Area}_{\mathrm{sky}}(\theta_n, \phi_n) \; . \tag{4.116}$$

The hemispherical distributions of the radiance, BRDFs and polarization values are presented in polar plots indicating zenith angles in equal radial measure out from the center of the plot and azimuthal variation in the clockwise direction. For a wind speed of $v = 5\mathrm{ms}^{-1}$, the peak in reflected radiance is displaced farther toward the horizon than the specular direction, see Fig. 4.13(a,c). This effect is expected to be exaggerated for stronger wind speeds. For purely specular reflection, Torrance & Sparrow (1967) suggest that this is due to greater shadowing and obscuration with increasing incidence angles that block portions of the reflecting facets that have higher reflected fluxes. A similar explanation is offered by Hoover & Gamiz (2006) in terms of the coherence solution to the BRDF and suggests that this shift is related to the functional form of the representative surface. Analytical models by Priest & Germer (2000, Fig. 1) and by Meister et al. (2001) show the same result. Therefore, in our exposition we keep the wind speed constant and vary only the solar incidence direction $\theta_s = 30°$ to $60°$. An increase in the incidence angle causes the reflectance peak to narrow but also brighten toward the horizon with a broadening spread at the rim of the sky that can be explained independent of inherent optical properties but dependent on geometrical varia-

tion (Simonot & Obein 2007, in fact, suggest a different approach to study the width of this peak). Interestingly enough, van Weiringen (1947), comparing with observations by Minnaert (1942, 1948) determined an analytic function using the sun-surface-sky geometry to describe the length and width of the elliptical area of sun reflections off the water surface. The results here only show the specular component of the reflectance in the specular direction of a flat surface. Had a diffuse component been included, there would be an added constant value of radiance in the solar plane in the direction of the sun (see van Ginneken et al. 1998, Fig. 2).

The narrowing of the reflectance peak and the movement toward the horizon have been observed by Cox & Munk (1956) (see also Walker 1994) and match similar calculations made by Mullamaa (1964). For highly specular rough surfaces, the width of the peak widens and vanishes as roughness increases (Jin & Simpson 1999 for snow and sea ice). Furthermore, Takashima & Masuda (1985) have modeled for a turbid ocean the increase in brightness toward the horizon as the incidence angle increases as well as the prominence of the reflection peak for small incidence angles and the fusing of the two as the incidence angle increases (both for effects including and excluding scattering from the water volume). Most significant are radiance measurements made by Brennan & Bandeen (1970) over the Pacific Ocean and by Davis & Cox (1982) on flights over the Arabian Sea. The scenes by Davis & Cox (1982) include effects by cumulus clouds but is considered to be "clear" as it is representative of fair weather conditions in the area. These observations show the shift in the peak toward the horizon as incidence angles increase, the lengthening of the peak as it moves away from zenith, its broadening at the rim of the sky as well as the increase in its intensity. Monte Carlo simulation results of a realistic atmosphere-ocean system by Plass et al. (1975, Fig. 5) show that for the

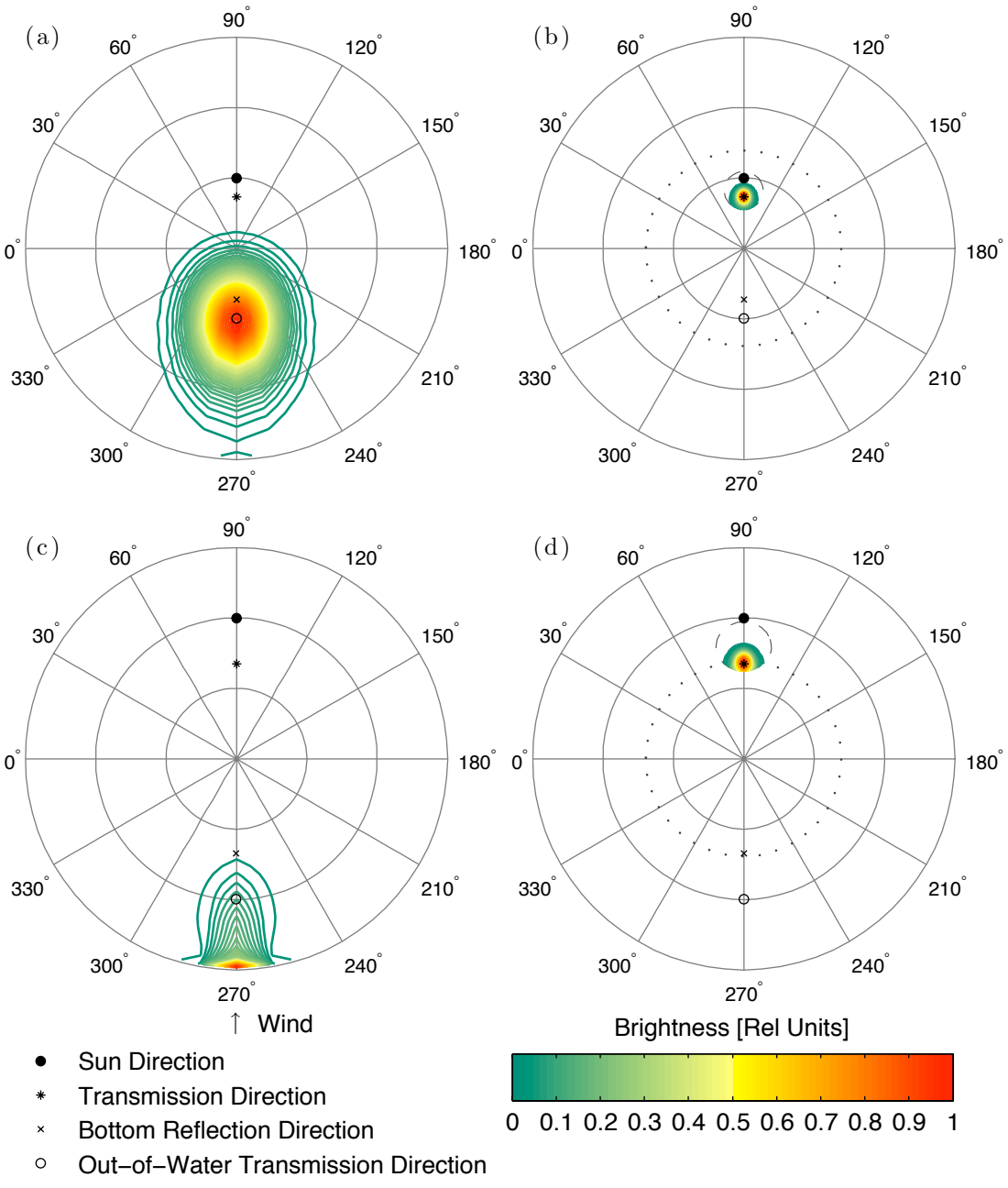


Figure 4.13: Normalized hemispherical radiance distribution after reflection (a,c) and transmission through the water surface (b,d) for different sun angles. (a) $\theta_s = 30°$, $a/l = 0.2$; (b) $\theta_s = 30°$, $a/l = 0.3$; (c) $\theta_s = 60°$, $a/l = 0.2$; (d) $\theta_s = 60°$, $a/l = 0.3$. Note the secondary peak emerging near the horizon, $\phi = 270°$, in (b).

sun at $\theta_s \approx 30°$ there are two peaks along the solar plane: one around the specular direction and one toward the horizon. Although it is not prominent, this effect is reproduced in Fig. 4.13(a) here. The peaks seem to fuse as the incidence direction increases away from zenith; the absolute radiance values are also higher compared to a flat surface viewing in the principal plane.

### 4.8.2 Event 2: Transmission through the water surface

The source Stokes parameters in the meridional plane of incidence are given by $\vec{S}(\vec{r}_s, 0)$, or $\vec{S}(\vec{r}_0, 0)$ from any point in the sky. It is necessary to rotate this vector to be referenced on the transmission plane (defined by the incidence direction and the facet normal): the transformation matrix required is $H(\psi_1)$ (Eq. 4.105), where $\psi_1$ is the angle between the meridian planes of scattering and incidence. Once on the scattering plane, the optical property of the surface affects the light as described by the transmission Mueller matrix. For the current event we denote this matrix as $D_2$ and replace in Eq. 4.101 $\chi_i = \chi_s$ (or $\chi_0$) and $\chi_t = \chi_2$. The final result is measured as referenced on the transmission meridional plane and thus rotated by $H(-\psi_3)$ (Eq. 4.105; the negative angle, again, referring to a reverse rotation using the right-hand rule from meridian to scattering plane). Furthermore, because there is a change in solid angle through transmission the resulting Stokes parameters are affected by the ratio of the indices of refraction of the second medium (water) to that of the first medium (air): $n = n_2/n_1$. This last result can be shown using Snell's law (Appendix A.3) and changing the solid angles (see Fig. 4.5 and Eq. 4.107) so that

$$d\Omega_1 = \left[\frac{n_2}{n_1}\right]^2 \frac{\cos\chi_2}{\cos\chi_1}\, d\Omega_2 \tag{4.117}$$

and

$$d\Omega_n = \left[\frac{n_2}{n_1}\right]^2 \cos\chi_2 \, d\Omega_2 \ . \tag{4.118}$$

The *effective* transmission Mueller matrix for every surface point acting on the incident light $\vec{S}(\vec{r}_s, 0)$ is

$$\cos\chi_2 \left[\frac{n_2}{n_1}\right]^2 H(-\psi_3)\, D_2\, H(\psi_1) \tag{4.119}$$

and the resulting transmitted light is described by the Stokes parameters

$$\vec{S}(\vec{r}_2, 0) = \sec\theta_2 \int_{\Omega_n} p(\theta_n, \phi_n) \sec\theta_n \cos\chi_2 \, n^2 \, H(-\psi_3)\, D_2\, H(\psi_1)\, \vec{S}(\vec{r}_s, 0)\ d\Omega_n \ , \tag{4.120}$$

where the secant factors are effects of the area projections of the facets (similar to the arguments made for Eqs. 4.38-4.40) onto the directions of the facet normal, $\theta_n$, and the transmission angle, $\theta_2$. Using Eqs. 4.110-4.113, the above equation becomes

$$\begin{aligned} \vec{S}(\vec{r}_2, 0) = &\sec\theta_2 \int_{\Omega_n} p\big(g(\theta_n, \phi_n), h(\theta_n, \phi_n)\big) \sec\theta_n \\ &\cos\chi_2 \, n^2 \, H(-\psi_3)\, D_2\, H(\psi_1)\, \vec{S}(\vec{r}_s, 0)\, d\Omega_n(\theta_n, \phi_n) \ . \end{aligned} \tag{4.121}$$

This can be further modified, using Eq. 4.114, as

$$\begin{aligned} \vec{S}'(\vec{r}_2, 0) = &\sec\theta_2 \ p\big(g(\theta_n, \phi_n), h(\theta_n, \phi_n)\big) \sec\theta_n \\ &\cos\chi_2 \, n^2 \, H(-\psi_3)\, D_2\, H(\psi_1)\, \vec{S}(\vec{r}_s, 0)\, \frac{1}{4}\mathrm{Area}_{\mathrm{sky}}(\theta_n, \phi_n)\ \sec\chi_1 \ . \end{aligned} \tag{4.122}$$

The peak in the transmitted radiance is centered around the transmission direction, as if the water surface were flat even for a wind-ruffled surface. This is shown in Fig. 4.13(b,d), all else held constant, even with varying incidence direction. We only consider the light in a small cone around the transmitted directions;

Smith (1974) estimates that the radiances around this point are at least two orders of magnitude lower (see reproduction in Fig. 4.14, also Tyler (1960)). There is, however, a widening in the width of the radiance peak as the incidence angle moves away from zenith and a corresponding increase in its intensity, not shown here (compare with Cox & Munk 1956, also Plass et al. 1975). This spreading of light, even with the same water surface characteristics, affects the incoming light field in the water such as to expand the area of bottom specular points, significantly affecting the light field impinging on the underwater bottom surface (Event 3, Sec. 4.8.3).

As the water surface gets rougher, the boundary of Snell's cone is blurred out so that for larger incidence angles Plass et al. (1975) show that the radiances are an order of magnitude higher than for a calm water surface in regions outside of this cone. As expected, the radiance at any azimuth angle is at a minimum around the boundary of Snell's cone.

### 4.8.3 Event 3: Reflection from the underwater bottom

The Stokes parameters of the light incident on the bottom surface underwater is, ignoring absorption in the water, simply the light transmitted through the air-water interface, $\vec{S}(\vec{r}_2, 0)$ (referenced on the transmission meridian plane). Let the transmission reference frame (from air to water in the previous section) be the underwater reference frame. The angle between the underwater meridional incidence and underwater reflection planes is $\psi_4$ (as in Fig. 4.8). $\psi_5$ is the angle between the underwater meridional reflection and underwater reflection plane (as in Fig. 4.9). $D_3$ (Eq. 4.97 with $r = 3$) is the reflection Mueller matrix of the underwater bottom surface. Substitute in Eq. 4.97 for the incidence angle $\chi_i =$

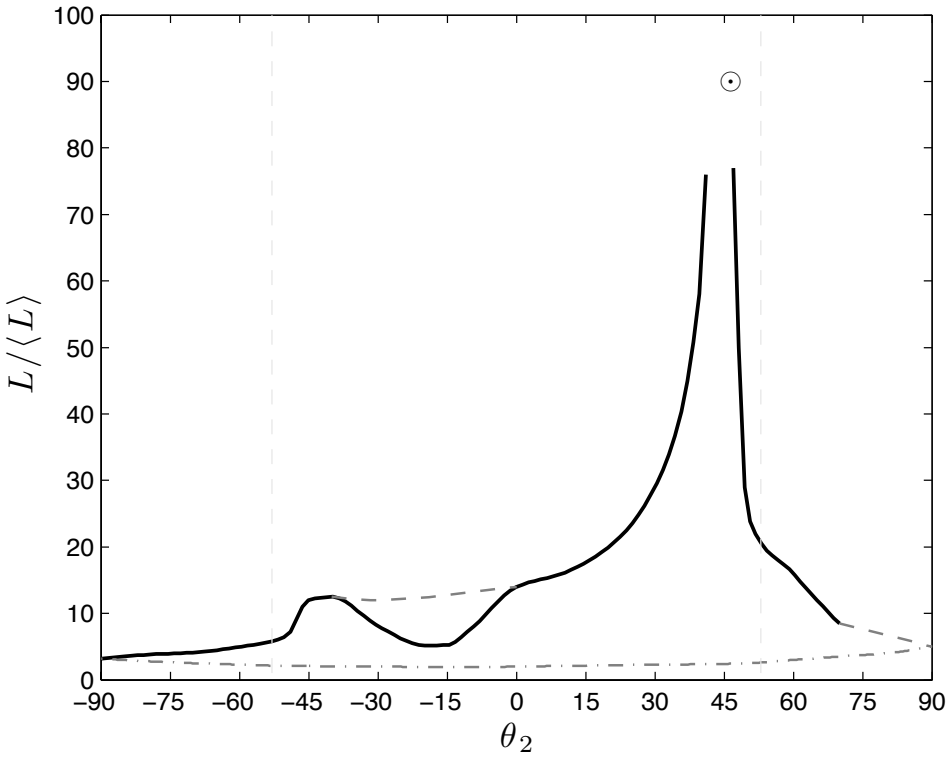


Figure 4.14: Relative radiance for transmitted light through an ocean surface in the solar plane at 20.4m depth and the sun at $\theta_s \approx 75°$ (above water), reproduced from Smith (1974, Fig. 7), corresponding to a photograph taken underwater viewing straight up. The measurement was made for a clear sky and a calm water surface in the Mediterranean Sea (08 July 1971). The dotted circle indicates the apparent sun underwater, $\theta_2 \approx 46°$. Vertical lines indicate the approximate boundary of Snell's window and a slight increase in radiance is observed as this boundary is approached. The dip in radiance at $\theta_2 = -20°$ is due to the shadow of the research vessel. The dot-dashed curve below represents the relative reflected radiance.

$\chi_2$, and the transmission angle $\chi_t = \chi_3$ (with reflection at $\chi_4$). The *effective* underwater reflection Mueller matrix for every point on the underwater surface acting on the underwater incident light $\vec{S}(\vec{r}_2, 0)$ (referenced on the underwater incidence meridional plane) is

$$\cos\chi_4 H(-\psi_5)\, D_3\, H(\psi_4)\ . \tag{4.123}$$

The cosine factor results from the projection of the underwater reflection solid angle $\Omega_4$ onto the solid angle centered around the bottom surface normal $\Omega_b$, which from Snell's law (Appendix A.3) is

$$d\Omega_b = \cos\chi_4 d\Omega_3\ . \tag{4.124}$$

The Stokes parameters of the reflected light from the bottom is then

$$\vec{S}(\vec{r}_3, 0) = \sec\theta_3 \int_{\Omega_b} p(\theta_b, \phi_b) \sec\theta_b \cos\chi_4\, H(-\psi_5)\, D_3\, H(\psi_4)\, \vec{S}(\vec{r}_2, 0)\, d\Omega_b\ , \tag{4.125}$$

where the secant factors are effects of the bottom area projections of the facets (Eqs. 4.38-4.40) onto the direction of the bottom facet normal, $\theta_b$, and the reflection direction, $\theta_3$. Notice this time that the integration is made over all solid angles, $d\Omega_b$, subtended by the underwater bottom surface.

The probability density function of normals of the bottom facet normals $(\theta_b, \phi_b)$ is described by $p(\theta_b, \phi_b)$ (Eq. 4.45). Let

$$g_b(\theta_b, \phi_b) = f_{b'x} = -\cos(\phi_b - \phi_{b'}) \tan\theta_b \tag{4.126}$$

and

$$h_b(\theta_b, \phi_b) = f_{b'y} = -\sin(\phi_b - \phi_{b'}) \tan\theta_b \tag{4.127}$$

(recalling Eqs. 4.43 and 4.44, respectively). The probability density function of bottom surface normals $p(f_{b'x}, f_{b'y})$ is given in Eq. 4.45. A transformation between

the coordinate systems produces

$$\int_{\Omega_b} p(\theta_b, \phi_b) \sec\theta_b \, d\Omega_b(\theta_b, \phi_b) = \int_{\Omega_b} p\big(g_b(\theta_b, \phi_b), h_b(\theta_b, \phi_b)\big) \left| \frac{\partial(f_{b'x}, f_{b'y})}{\partial(\theta_b, \phi_b)} \right| \sec\theta_b \, d\Omega_b(\theta_b, \phi_b) \ , \quad (4.128)$$

where

$$\left| \frac{\partial(f_{b'x}, f_{b'y})}{\partial(\theta_b, \phi_b)} \right| = \frac{\sin\theta_b}{\cos^3\theta_b} \ . \quad (4.129)$$

Thus we have

$$\vec{S}(\vec{r}_3, 0) = \sec\theta_3 \int_{\Omega_b} p\big(g_b(\theta_b, \phi_b), h_b(\theta_b, \phi_b)\big) \frac{\sin\theta_b}{\cos^3\theta_b} \cos\chi_4 \, H(-\psi_5) \, D_3 \, H(\psi_4) \, \vec{S}(\vec{r}_2, 0) \, \sec\theta_b \, d\Omega_b(\theta_b, \phi_b) \ . \quad (4.130)$$

An approximation to this (using similar arguments made in Appendix C.2) is

$$\vec{S}'(\vec{r}_3, 0) = \sec\theta_3 \, p\big(g_b(\theta_b, \phi_b), h_b(\theta_b, \phi_b)\big) \sec\theta_b \cos\chi_4 \, H(-\psi_5) \, D_3 \, H(\psi_4) \, \vec{S}(\vec{r}_2, 0) \, \frac{1}{4} \, \mathrm{Area}_{\mathrm{sky}}(\theta_b, \phi_b) \, \sec\chi_2 \ . \quad (4.131)$$

Before we compare a change in roughness, consider the change in the incidence direction of the source above water from $\theta_s = 30°$ to $60°$: comparing Fig. 4.15(a,b) to (c,d). Because a larger incidence angle spreads the transmitted light field (recall from results in Sec. 4.8.2), the reflected light carries that spread around the specular direction. Furthermore, the reflection peak approaches the horizon as the incidence angle increases from zenith, as if the surface were flat. Measurements of wet ooid sand by Zhang et al. (2003a,b) confirm the emergence of a specular peak, albeit not all too prominent. However, compared with results in Sec. 4.8.1 here, the reflected radiance peak of the bottom surface moves slower toward the horizon as the incidence angle increases.

Now consider a black sky with the sun at $\theta_s = 30°$ in Fig. 4.15(a,b). A bottom with any amount of roughness moves the peak of the reflected radiance away from the specular direction, also for $\theta_s = 60°$ in Fig. 4.15(c,d). The different facet orientations lengthen (i.e., expanding more frontal than lateral) the area of possible specular points. For a bottom surface with a roughness $a/l = 0.2$ (Fig. 4.15(a,c)), the peak is narrower and closer to the specular direction compared to a bottom with $a/l = 0.3$ (Fig. 4.15(b,d)). As the bottom roughness increases and the radiance distribution broadens around the rim of the underwater sky, a secondary peak at the rim becomes apparent in Fig. 4.15(b) (also found on the water surface, Sec. 4.8.1). This peak, however, is lost to the horizon as the sun incidence direction increases to $\theta_s = 60°$ (Fig. 4.15(d)).

Because we expect the radiance contribution by the direct beam of the sun to be greatest in the direction of specular reflection and the specular component of a surface to dominate the radiance distribution, this effect on the upwelling light field from a reflective underwater surface at shallow optical depths can be significant (e.g., Luchinin 1979). In any case, even as the radiance drops to about a three orders of magnitude for increased turbidity (Plass et al. 1975), the angular variation in the radiances remain essentially unchanged.

### 4.8.4 Event 4: Transmission of reflected light back out of the water

From the previous section, $\vec{S}(\vec{r}_3, 0)$ describes the underwater (upwelling) light field produced by the bottom surface. Let this be the impinging "sky" onto the underside of the water surface. The water surface has the same probability density function of normals, $p(f_x, f_y)$, as before (Eq. 4.25). The solid angles of light im-

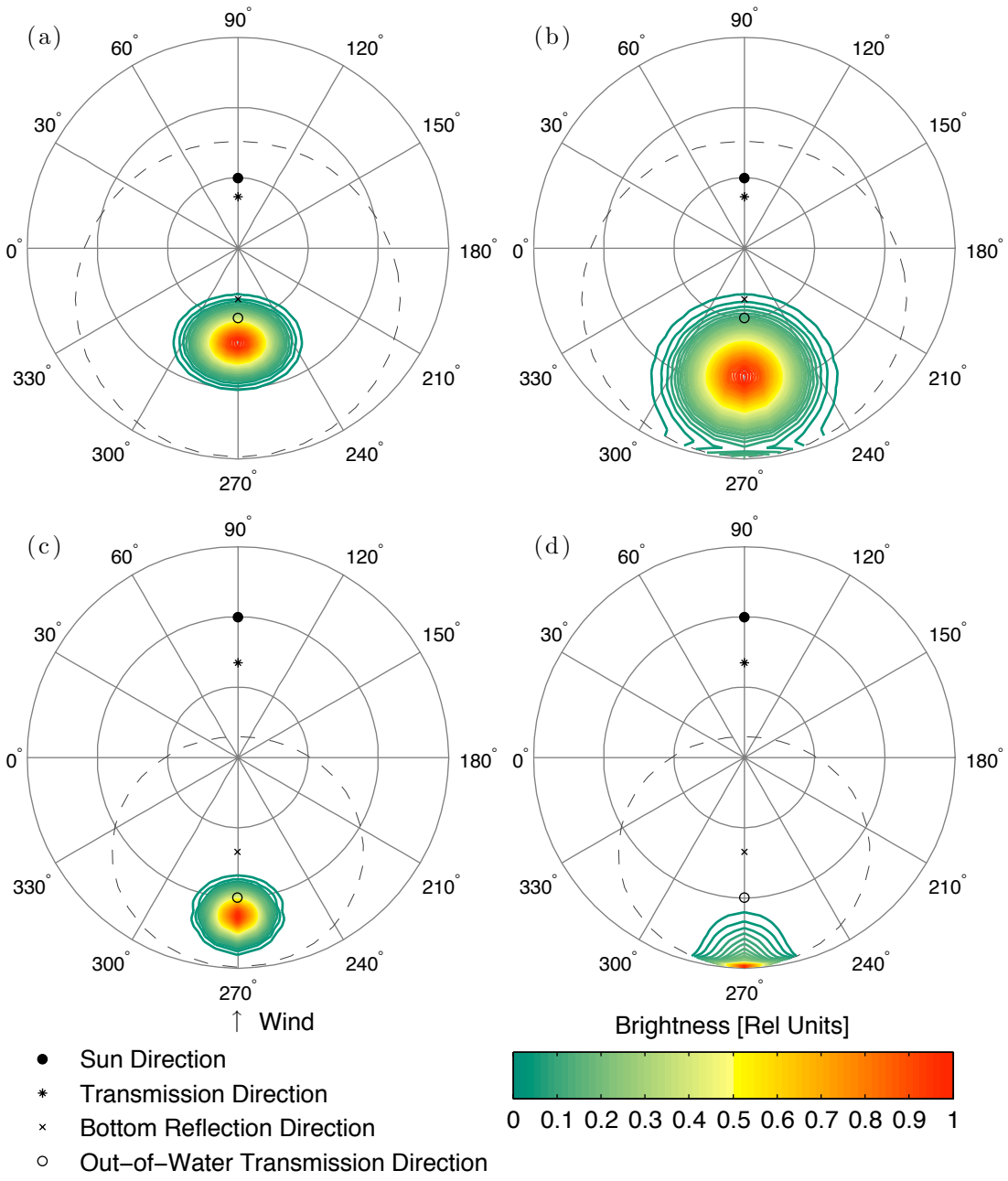


Figure 4.15: Normalized hemispherical radiance distribution after reflection off the underwater bottom surface for different sun angles. (a) $\theta_s = 30°$, $a/l = 0.2$; (b) $\theta_s = 30°$, $a/l = 0.3$; (c) $\theta_s = 60°$, $a/l = 0.2$; (d) $\theta_s = 60°$, $a/l = 0.3$.

pinging under the water surface and emerging out of the water surface are related by Snell's law (Appendix A.3):

$$n_2{}^2 \cos\chi_5 \, d\Omega_5 = n_1{}^2 \cos\chi_6 \, d\Omega_6 \ , \tag{4.132}$$

where again $n_2$ is the refractive index of water and $n_1$ that of air, $\chi_5$ is the incidence angle on a point on the water surface underwater and $\chi_6$ is the transmitted direction through the water surface into air, both relative to the local surface normal. In relation to the emergent angles in air, the solid angles are related by

$$d\Omega_n = \cos\chi_6 \, d\Omega_6 \ . \tag{4.133}$$

The angles between the meridional incidence and transmission planes and the scattering plane are $\psi_6$ and $\psi_7$, respectively. Given a transmission Mueller matrix $D_4$ (given in Eq. 4.101 for $t = 4$ and substituting $n_i = n_2$, $n_t = n_1$, $\chi_i = \chi_5$ and $\chi_t = \chi_6$) the *effective* transmission Mueller matrix acting on the Stokes parameters $\vec{S}(\vec{r}_3, 0)$ is

$$\cos\chi_6 \, H(-\psi_7) \, D_4 \, H(\psi_6) \ . \tag{4.134}$$

Following arguments in the previous sections, the Stokes parameters of the light transmitted back into air out of the water are determined from

$$\vec{S}(\vec{r}_4, 0) = \sec\theta_4 \int_{\Omega_n} p(\theta_n, \phi_n) \sec\theta_n \cos\chi_6 \, H(-\psi_7) \, D_4 \, H(\psi_6) \vec{S}(\vec{r}_3, 0) \, d\Omega_n \ . \tag{4.135}$$

Using the arguments in Eqs. 4.110-4.113, we have

$$\begin{aligned} \vec{S}(\vec{r}_4, 0) = & \sec\theta_4 \int_{\Omega_n} p\big(g(\theta_n, \phi_n), h(\theta_n, \phi_n)\big) \frac{\sin\theta_n}{\cos^3\theta_n} \\ & \cos\chi_6 \, H(-\psi_7) \, D_4 \, H(\psi_6) \, \vec{S}(\vec{r}_3, 0) \, \sec\theta_n \, d\Omega_n(\theta_n, \phi_n) \ . \end{aligned} \tag{4.136}$$

For incidence directions $\chi_5$, the approximation to this (again using arguments in Appendix C.2) is

$$\vec{S}'(\vec{r}_4, 0) = \sec\theta_4 \; p\big(g(\theta_n, \phi_n), h(\theta_n, \phi_n)\big) \sec\theta_n \\ \cos\chi_6 \, H(-\psi_7) \, D_4 \, H(\psi_6) \, \vec{S}(\vec{r}_3, 0) \frac{1}{4} \, \mathrm{Area}_{\mathrm{sky}}(\theta_n, \phi_n) \; \sec\chi_5 \; . \qquad (4.137)$$

The results for the radiance distribution that is transmitted out of the water carries with it the effects of the lengthening of the area of possible specular points by the bottom roughness and the shift in the radiance peak toward the horizon as well as further effects from the water surface. As expected, a rougher surface also pushes the peak out toward the horizon, compare Fig. 4.16(a) and (b). The (lateral) widening around the rim of the sky is apparent in Fig. 4.16(c,d) as the peak touches the horizon. As the underwater bottom gets rougher and the radiance peak broadens, the intensity conversely weakens.

Just to compare, in Monte Carlo simulations of a realistic atmosphere-ocean system for deep water Plass et al. (1975) show that radiances above the sea surface increase in the solar plane and the peak around the specular direction of $\theta_4 = 57°$ widens as the wind speed increases although very little changes in the side scattering directions. At stronger wind speeds (approximately $10\mathrm{ms}^{-1}$), the radiance increases exponentially from zenith. For large incidence angles, the specular peak is narrow and prominent for a calm ocean surface and widens as the water surface gets rougher. They also show that the contribution of the direct sun beam dominates the radiances above the ocean for slower wind speeds and while its influence is reduced for greater wind speeds it determines the shape of the distribution at different angles in the solar plane (Plass et al. 1975, Fig. 18). For a calm ocean the diffuse component has a relatively stronger influence. As the optical depth increases in deep water, the peak in the radiance distribution approaches zenith,

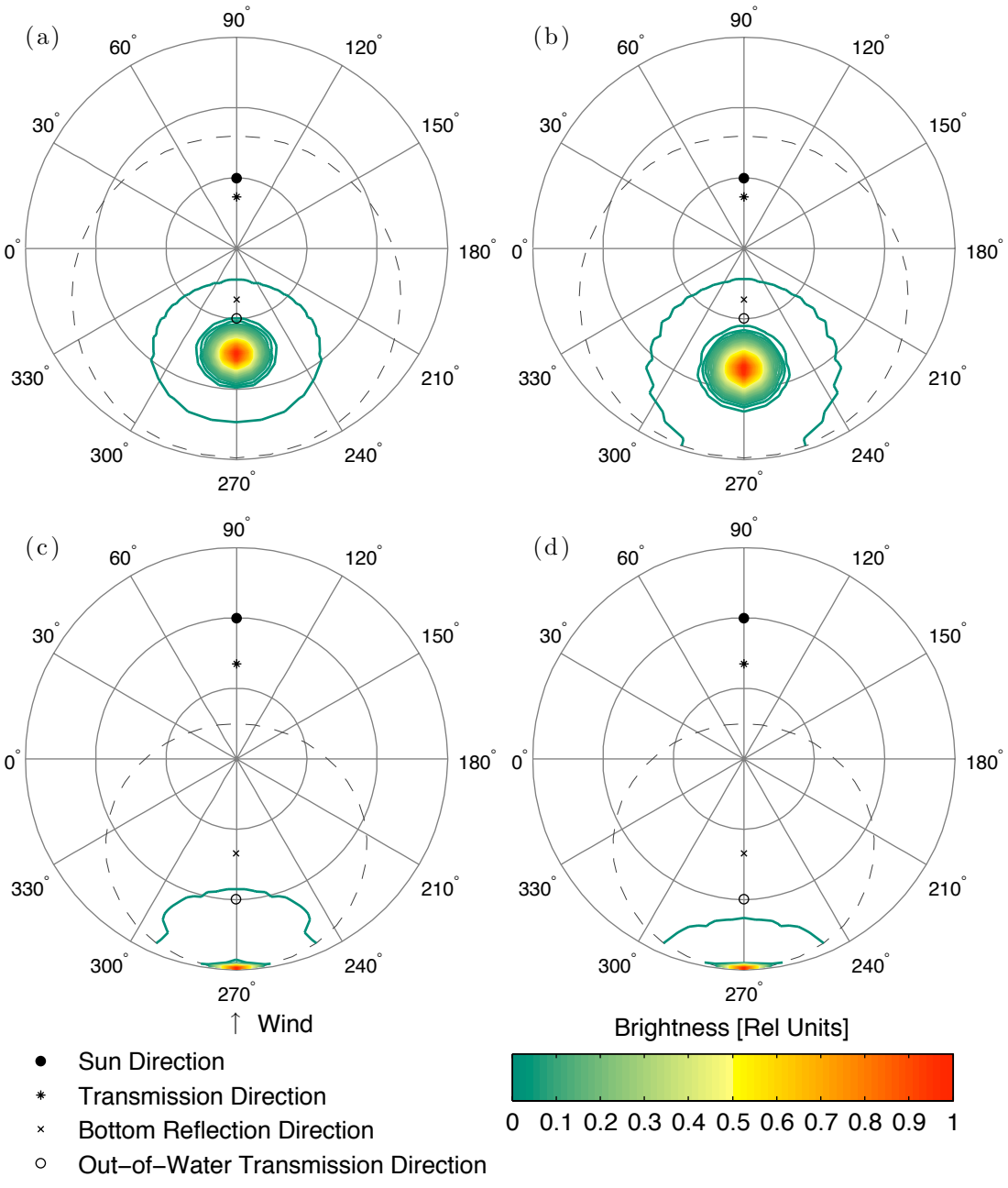


Figure 4.16: Normalized hemispherical radiance distribution after transmission out of the water through the air-water-bottom system for different sun angles and bottom roughnesses. (a) $\theta_s = 30°$, $a/l = 0.2$; (b) $\theta_s = 30°$, $a/l = 0.3$; (c) $\theta_s = 60°$, $a/l = 0.2$; (d) $\theta_s = 60°$, $a/l = 0.3$.

regardless of the roughness of the water surface. This peak is dominated by the contribution of the direct sun beam.

Note that measurements in the natural environment contain the reflected radiances off the water surface and that the reflected and transmitted radiance distributions are interdependent (Walker 1994, p. 547). As the water surface gets rougher the water surface looks darker especially at larger sun angles (Plass et al. 1975 at 460nm). However, as we have shown, considering only specular reflections, the direct beam of the sun contributes to a radiance peak at larger zenith angles for a large solar incidence angle (this is expected regardless of surface roughness with $v \neq 0\text{ms}^{-1}$).

## 4.9 Model BRDF

The bidirectional reflectance distribution function (BRDF) is a concept of light measure emerging from the assumption that reflectance is a geometric property of a surface. In the natural environment, the light incident on a representative surface (at any point) is measured from all directions assuming it is directionally the same throughout the surface. The light leaving the surface, however, is usually conveniently measured by a detector with a limited field of view centered around a single direction. Thus, the reflectance of a surface is measured as the ratio of this emerging light with radiance $L_r$ to the incident light with irradiance $E_i$. Without presenting the derivation here, the BRDF is defined by Nicodemus et al. (1977, Eq. 9) as

$$f_r(\theta_i, \phi_i; \theta_r, \phi_r) \equiv \frac{dL_r\left(\theta_i, \phi_i; \theta_r, \phi_r; E_i\right)}{dE_i\left(\theta_i, \phi_i\right)} \equiv \frac{dL_r\left(\theta_i, \phi_i; \theta_r, \phi_r; E_i\right)}{L_i\left(\theta_i, \phi_i\right) \cos\theta_i \, d\Omega_i} \left[\text{sr}^{-1}\right], \quad (4.138)$$

where $i$ and $r$ indicate the incident and emergent directions, respectively, and $d\Omega_i$ is the differential solid angle of incidence within which the light is confined. It is the derivative of instantaneous values and therefore cannot be measured directly. Actual measurements produce average quantities, so that the representation as a ratio is an extremely useful measure.

For *in situ* measurements in oceanographic applications, the in-water reflected radiance can be measured, but for long-term monitoring it is the water-leaving radiance that is measured in practice. A measure related to the BRDF is the remote sensing reflectance, defined in, e.g., Mobley et al. (2003) as the ratio of the water-leaving radiance (without the effects of water surface reflections) to the incident irradiance assuming a flat water surface:

$$R_{RS}(\theta_u, \phi_u) = \frac{L_u(\theta_u, \phi_u)}{E_d} \ , \tag{4.139}$$

where $u$ and $d$ refer to the light exiting from (upwelling) and incident on (downwelling) the system, respectively. In our results, because we consider the sun as the only source in an otherwise black sky, we can use this non-differential form of the BRDF (also Snyder 1998, Otremba 2003).

In our formulation, the contribution from water surface reflection and light emerging from the air-water-bottom surface are clearly distinguished. Although the reflection from the water surface are orders of magnitude higher than the values coming from below the surface, a bright bottom in optically shallow water can contribute to a significant increase in the intensity of the water-leaving radiance. Because we consider a sun-only source in a black sky, the denominator on the right-hand side of Eq. 4.138 reduces to just the sun irradiance, $E_s$, coming from a single direction. As such, the BRDF patterns are similar to the radiance distributions provided in Secs. 4.8.1-4.8.4. The importance, however, of this discussion is

to point out that if absorption in the water were taken into account, the radiance distribution in the numerator in Eq. 4.138 will be affected. Longer path lengths in the water will diminish light more than would shorter path lengths and would add a wavelength-dependent component to the problem. The errors related to this have been presented in Chap. 2. If the bottom is highly absorbing then polarization is higher than if the bottom is treated as reflective (Priest & Meier 2002). In general, the upwelling and downwelling underwater light field will brighten toward zenith, regardless of the roughness of the underwater surface. On average, this will depend on the brightness and optical depth of the bottom as well as its roughness dimension relative to depth (see Chap. 3). Variations in the probability distributions of path lengths related to water surface tilts and underwater bottom tilts will facilitate this analysis, but this is left for future investigations. Furthermore, with illumination contributions from skylight, we can expect a change in the BRDF patterns dependent on skylight distribution as well as the brightening toward zenith from the contribution of a rough bottom (see Voss et al. 2003).

Rough natural surfaces that are considered to be diffuse are known to exhibit non-Lambertian behavior in the retroreflection direction. This is purely a geometrical effect, all other things equal, owing to the distribution of the surface facets that increase the reflectance in the viewing direction. Given a material reflectance $\rho$, the measure of non-Lambertian behavior is how much the ratio of water-leaving radiance to incident irradiance, $L_u/E_d$, deviates away from $\rho/\pi$ at any given viewing direction. By our arguments in Chap. 3 here and as is shown in Zaneveld & Boss (2003), the apparent reflectance affects $\rho$ in the near-field and is thus important in the consideration of optically shallow environments. For incident angles $\theta > 35°$, the reflectance of ooid sand can be significantly non-Lambertian, exhibiting strong

retroreflection properties (Mobley et al. 2003). Nonetheless, Mobley et al. (2003) state that non-Lambertian effects are greatest for shallow waters and decrease with depth. In a shallow water environment the direct light from the sun dominates the light field incident on the underwater surface. For shallow benthic environments around the Bahamas, Louchard et al. (2003) measure the ratio $L_u/E_d$ to be as high as $0.08\text{sr}^{-1}$ at 500nm. Our model considers only the specular component so the "hot spot"' or retroreflectance peak, which is an effect of the diffuse component, is not evident; measurements by Zhang et al. (2003a,b) of Bahamian sediments exhibit this diffuse property.

## 4.10 Polarization effects

> The light from an object is of two kinds: (1) some of the light is scattered from the object after partial penetration; this light gives the true body color of an object, such as the red color of a brick, or the green of a leaf; (2) some of the light is genuinely reflected from the surface of the object, giving the object a sheen or a sparkle. The first sort of light is unpolarized; the second partially or completely polarized... .
>
> *E. O. Hulburt, 1934*

Surfaces and interfaces polarize light. Incident light that is polarized as it is reflected and transmitted through an interface is described simply by the Fresnel law of reflection (e.g., Tynes et al. 2001, Sabbah et al. 2006). In general, for a flat water surface, the degree of (linear) polarization of refracted light increases with the incidence angle of light that is randomly polarized (Horváth & Varjú 1995). For the simple realization of an air-water-bottom system presented here, there

are three opportunities for polarization, one for each surface interaction. Volume scattering is ignored in the system but even as light is scattered, it is surface scattered thrice before it emerges. This polarization however, in the absence of absorption is independent of surface roughness: the ratio $U/Q$ (the ratio of the third to the second Stokes parameters in Eq. 4.90) remains almost invariant (only acting to shift the phase of the light beam) through changes in the effective Mueller matrices, Eqs. 4.106 and 4.119. Thus, in the absorption-free condition, we do not show the results for change in surface roughness but only for a change in incidence direction (following figures).

Randomly polarized light that is incident on the water surface becomes polarized upon reflection and transmission, see Fig. 4.17. The degree of polarization of the light reflected off the water surface is lowest centered around the direction of the incoming light and is greatest approximately 90° from the sun in the solar plane, Fig. 4.17(a,c). This is as it is expected and is a surface effect (matching results and discussion by Horváth & Varjú 1995, Fig. 12). Recall that the wind roughness and bottom roughness planes are aligned along the solar plane. As these orientations change, even with no change in each of their roughnesses, some polarization effect can be expected. At transmission, minimal polarization happens due to the imposition of the transmission window (Brewster 1830), Fig. 4.17(b,d). However, Plass et al. (1975) show that an increase in the transmitted flux into the ocean can be expected with an increase in wind speed.

The peak in polarization is at Brewster's angle, $\tan^{-1}(n_2/n_1) \approx 53°$ from the sun, and is a surface effect. In theory without any other effects light is completely polarized by a flat surface. To compare, Takashima & Masuda (1985) include volume scattering and show at most a polarization of $\sim 80\%$ at the horizon for

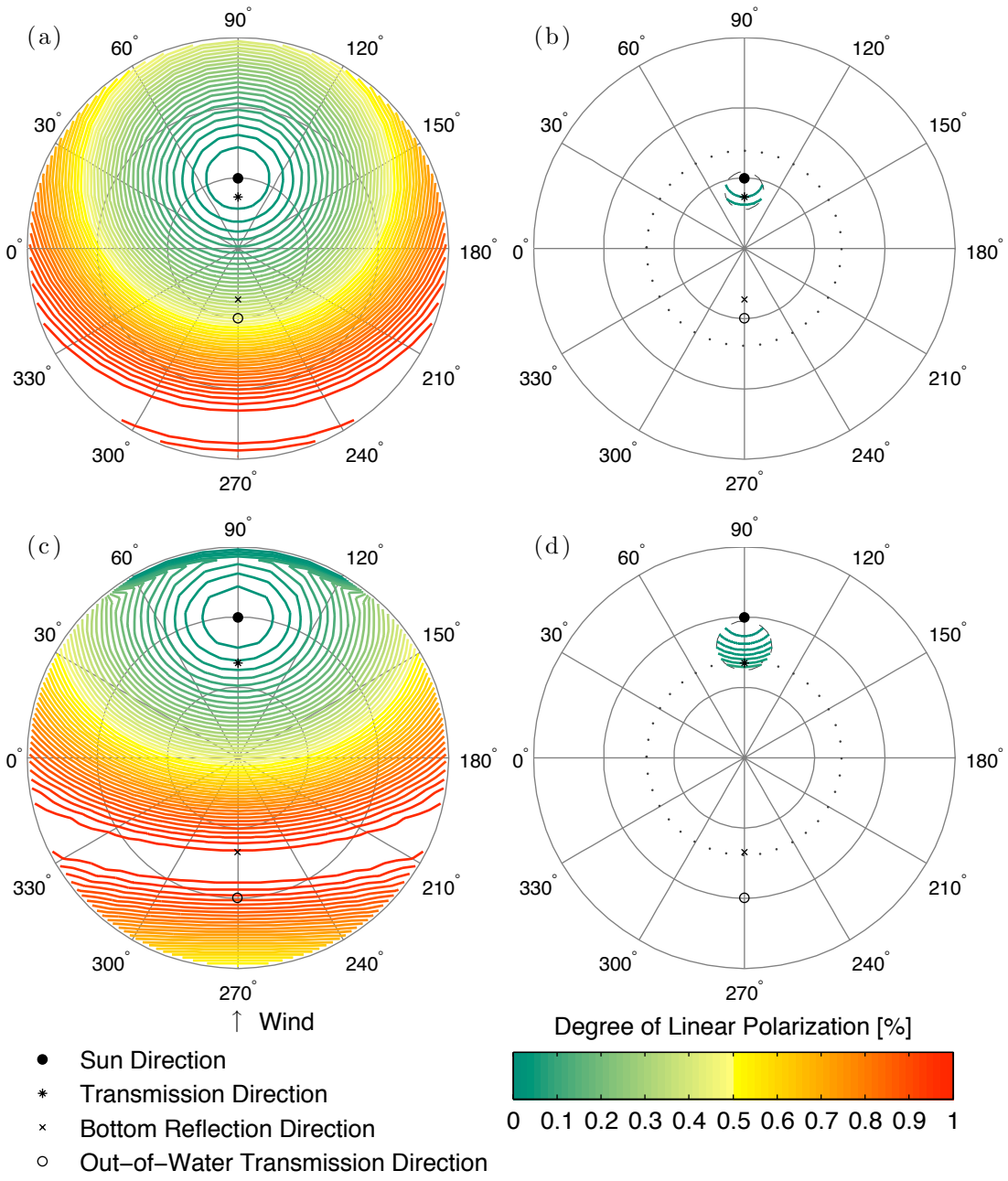


Figure 4.17: Hemispherical degree of polarization after reflection (a,c) and transmission (b,d) through the water surface for sun angles $\theta_s = 30°$ (a,b) and $60°$ (c,d).

a turbid ocean and a clear atmosphere. They show about a 17% decrease for a hazy atmosphere. The effect of a wind-ruffled sea surface is only a decrease of 0.2% in the polarization (for $2 \leq v \leq 8\text{ms}^{-1}$). In the results we present, we ignore any change in the wind speed and keep it constant so as to isolate the effects of the underwater bottom roughness. Any roughness change, however, still only causes a phase shift, which will not be apparent (or measurable in the time and space averaged intensity); also, its effective Mueller matrix acts only as a retarder, Fig. 4.18(a,c).

Actual measurements for polarization underwater by Cronin & Shashar (2001) produced values no greater than 50%. Their results corroborate the findings by Waterman (1954) that there is no considerable influence by skylight polarization at depths exceeding 15m although Horváth & Varjú (1995) suggest otherwise for shallow water. Recall that in our realization polarization is only "turned on" when light is incident on the water interface; light from the sky or the sun is assumed to be randomly polarized. Ivanoff & Waterman (1958) find that in-water polarization is almost insensitive to the wavelength of light (also Cronin & Shashar 2001), i.e., polarization mainly decreases with increasing scattering in the water, and suggest that the optimum wavelength to consider for polarization is that which produces the maximum amount of light to measure (425nm for clear ocean water, Waterman 1954). However, in the shorter wavelengths, where the sensitivity to polarization is weaker, it allows for distinguishing surface effects from volume effects (Ivanov & Toporets 1956 and Chowdhary et al. 2002).

To change the polarization of the system, absorption needs to be taken into account (e.g., Priest & Meier 2002). Neglecting polarization effects may introduce errors in the BRDF (e.g., Flynn & Alexander 1995, Eqs. 14 and 21, Snyder

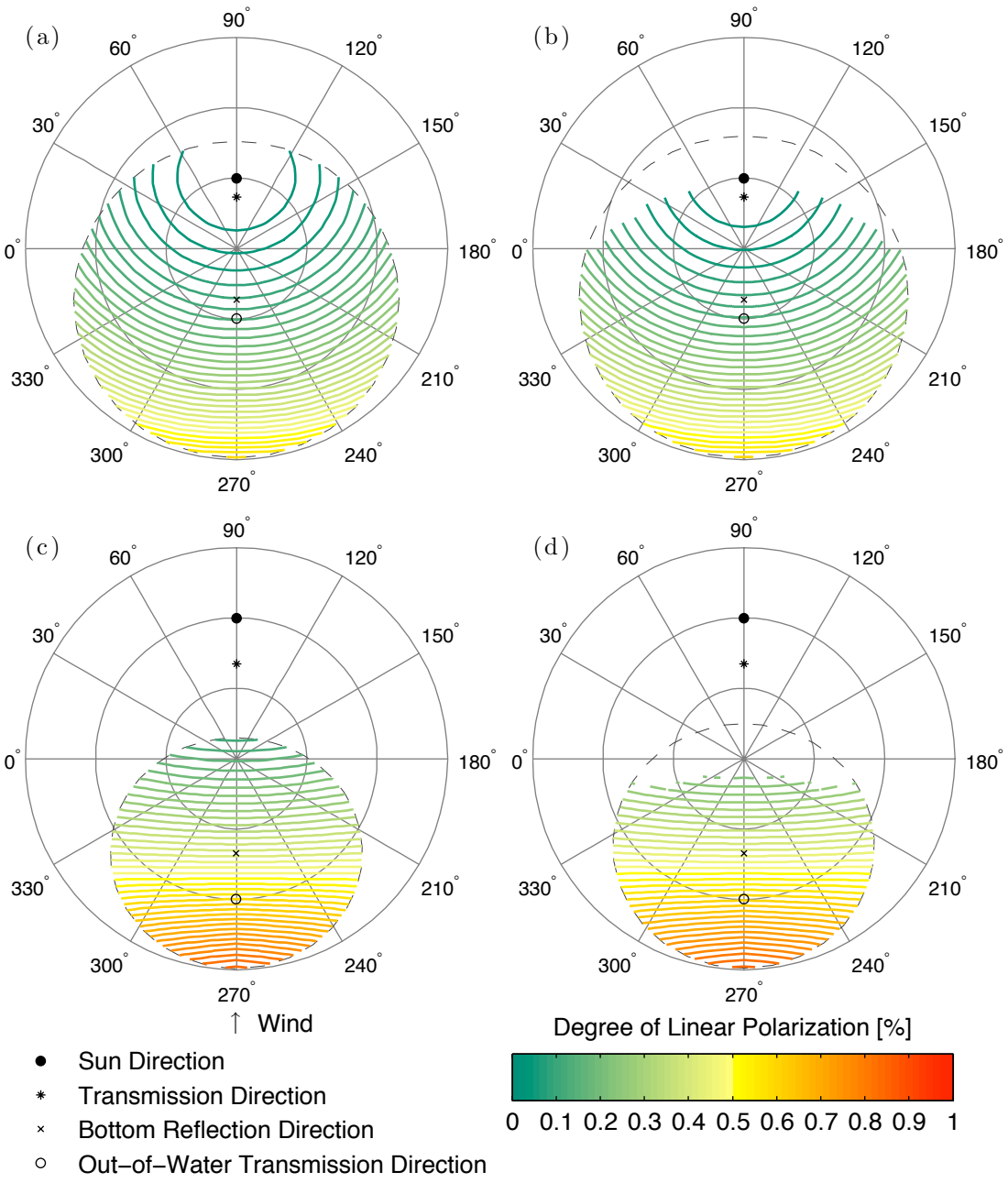


Figure 4.18: Hemispherical degree of polarization after reflection off the underwater bottom surface (a,c) and after transmission out of the water (b,d) through the air-water-bottom system for sun angles $\theta_s = 30°$ (a,b) and $60°$ (c,d).

1998). Aas & Højerslev (1999) suggest that there are significant variations in the radiance distributions transmitted into the water within and outside Snell's cone. Horváth & Varjú (1995) further suggest that there are two distinct underwater polarization patterns: again, one within Snell's cone and one outside it. Kattawar & Plass (1976) show from Monte Carlo simulations of optically thick media that polarization is dependent entirely on the medium in which light travels and while it approaches an asymptotic limit as depth increases, it cannot be ignored in areas closer to surface boundaries where the radiance distribution is significantly affected. As with the BRDF (see Sec. 4.9), the shallower the water depth, the greater the relative differences in the path lengths that light travels in the medium and the greater the variation in the Stokes parameters.

In actual measurements, the change in polarization comes from the variability within the scattering media rather than from the change in surface roughness. However, if the surface indeed induces any polarization effects and its roughness determines a variation in the path lengths of light reflected from it then the polarization is not independent of that roughness (although, indeed the effect is separable, Wellems et al. 2006). Polarization is still expected to be at a maximum around the anti-solar direction (Fig. 4.18(b,d)). With this in mind, direct effects from the scattering medium and indirect ones from the surface can be derived by looking at the polarization in the anti-solar direction above the water surface. Also, as the incidence angle increases, the region of maximum polarization is expected to move away from the specular peak and this is where any effect from in-water scattering is expected to be the most pronounced (Takashima & Masuda 1985, Kattawar & Adams 1989). Furthermore, polarization due to surface reflection or transmission has been observed by Wellems et al. (2006) to be reduced by surface roughness

at scales close to the wavelength of radiation. There are two sources of polarization: sunlight that is randomly polarized but polarized at first interaction with the air-water interface and polarization by scattering in the atmosphere and in the water volume. The first we have already discussed, the second we have ignored. A polarization peak at 90° from the direction of light propagation can be expected if Rayleigh scattering by atmospheric and oceanic particles were included (Waterman 1954). Skylight polarization underwater vanishes with increasing depth or turbidity. However, in optically shallow water, polarization has been observed to be similar to the pattern from the sky, except, of course, that it falls within Snell's window (Waterman 1954, Horváth & Varjú 1995). Ignoring skylight polarization is a limitation for this model if used for passive imaging systems that are viewing far enough away that the roughness effects are washed out.

If the incident radiation on the system is randomly polarized, as we assume, the polarization begins as the light interacts with the water surface and can be explained by looking at the orientation of the emerging polarization ellipse, which to recall from Eq. 4.90 is a function of the ratio of the third and second Stokes parameters of the light,

$$\psi = 0.5 \tan^{-1} \frac{U}{Q} \,, \tag{4.140}$$

see Fig. 4.19 for the reflected and transmitted distributions. It is the same way for the out-of-water polarization distribution in Fig. 4.20. The change in orientation of the polarization ellipse emerges entirely from light interacting with the surfaces (Kattawar & Adams 1989). At the point of transmission out of the water the orientation of the polarization ellipse can be expected to be at small angles to the horizontal with a local maximum in the direction of backscattering towards the in-water transmission direction (Fig. 4.20(b,d)). The reader is cautioned against

confusing the orientation of the polarization ellipse and the ellipticity of the Stokes parameters (e.g., Kattawar & Adams 1989, Meyers 2002, Tyo et al. 2006). We are referring here to the orientation of the ellipse with respect to a reference axis perpendicular to the plane of light propagation. To be useful to any observer, the current bases need to be transformed to align with the viewing axis (e.g., Matchko & Gerhart 2005). Again, the current results are limited by the fact that attenuation along the paths of light is ignored and so there are no roughness effects on polarization.

Matchko & Gerhart (2005) show that information on both the degree of polarization and the orientation of the polarization ellipse can drastically improve information extracted about surfaces and their curvature. Furthermore, Stagg & Charalampopoulos (1991) show that the components of the (complex) index of refraction of a material can be determined from the polarized radiance components. However, Wellems et al. (2006) show that this approach will be in error if the roughness of the surface affects its reflectance significantly, e.g., when the wavelength of radiation is close to the scale of the roughness.

From measurements made in the Californian coast, Fougnie et al. (1999) find that the optimal viewing direction that reduces water surface reflection effects is in the backscattering hemisphere off the solar plane, ideally at an azimuth distance from the sun of 45° and at zenith directions approaching Brewster's angle ($\sim 45°$), measuring with a vertical polarizer. However, water surface transmission effects that cause focusing of light onto the underwater surface (not a BRDF effect!) that may significantly affect the underwater upwelling light field (Timofeeva 1957, Ivanov & Prikhach 1976, Voss et al. 2003) is not eliminated by this viewing

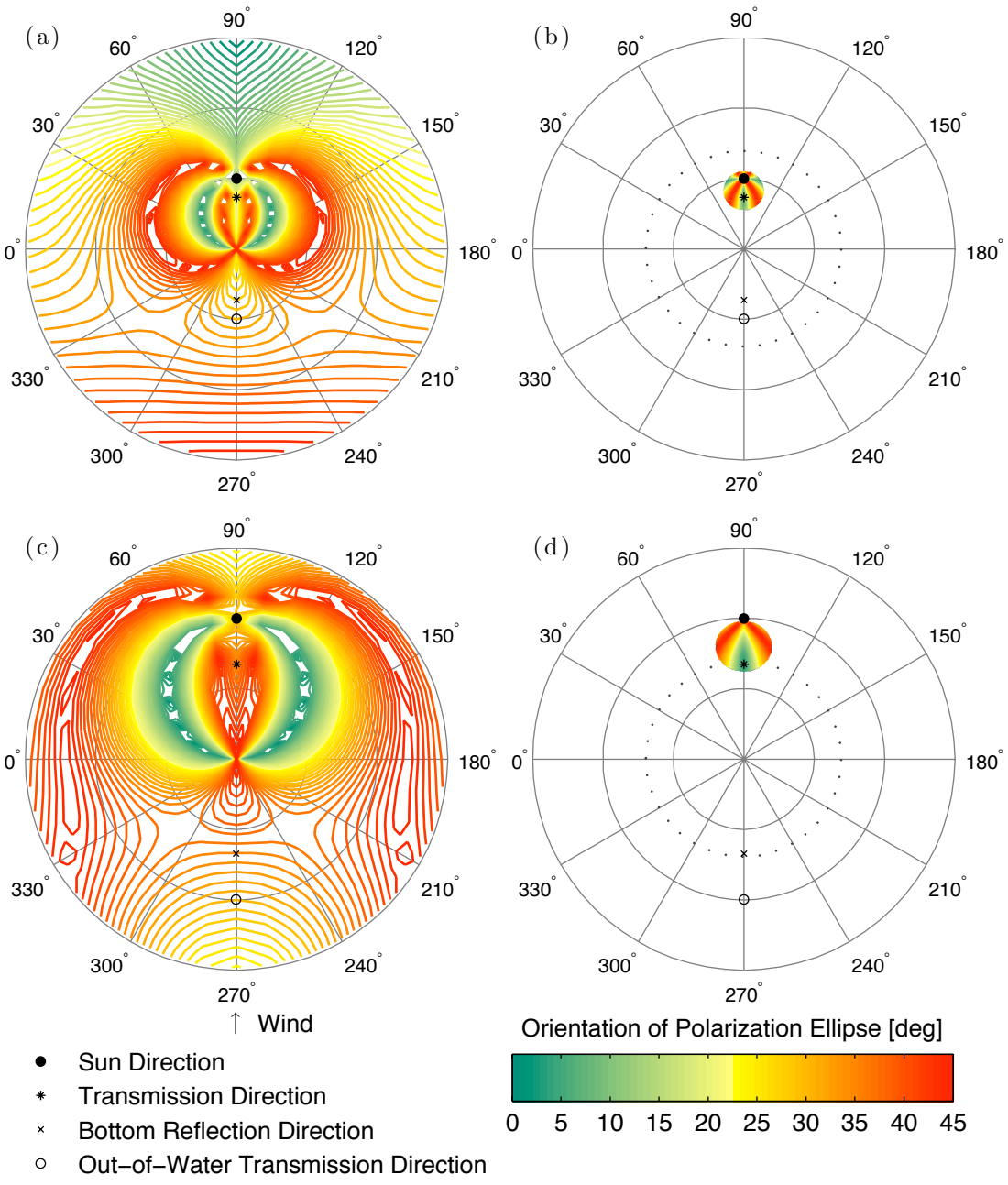


Figure 4.19: Orientation of the polarization ellipse after reflection off (a,c) and transmission through (b,d) the water surface for sun angles $\theta_s = 30°$ (a,b) and 60° (c,d).

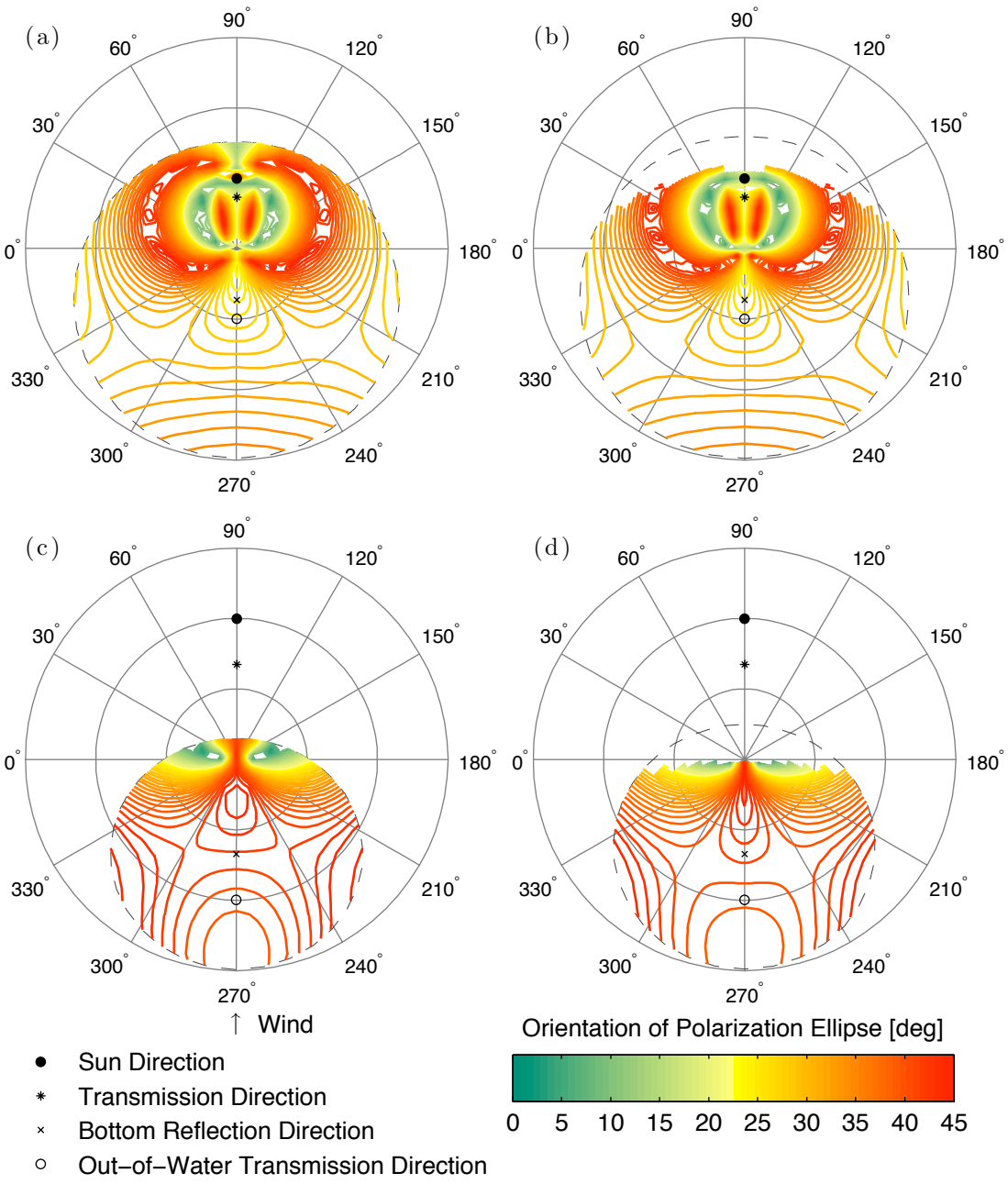


Figure 4.20: Orientation of the polarization ellipse after reflection off the underwater bottom surface (a,c) and after transmission out of the water (b,d) through the air-water-bottom system for sun angles $\theta_s = 30°$ (a,b) and $60°$ (c,d).

orientation but is averaged out for rough surfaces, see Chap. 3 and Zaneveld & Boss (2003).

## 4.11 Summary

We have studied the behavior of the specular component of reflection for an air-water-bottom system. The model includes specific alignment of the solar, wind roughness and bottom roughness planes along any azimuth. Geometric optics applies and the vector descriptions are described in detail. Instead of defining the surfaces analytically, they are expressed statistically. The water surface has a slope distribution that has been empirically derived elsewhere (Cox & Munk 1954, 1956) and the bottom surface is a statistical parametrization of the analytic surface expression. The radiance plots are purely of the specular component. They are indicative of the probability that a facet is oriented in a certain direction to produce the effects expected. As such, scintillation (sparkle) effects are implied and not modeled. The option to include a theoretical description of sky illumination distribution is included but results presented here only show illumination by the sun as a point in a black sky. Analysis of effects of sun and sky illumination variations will be included future investigations.

Specular reflections are useful, for example, in computer graphics for rendering natural water surfaces (e.g., He et al. 1991, Premože & Ashikhmin 2001), in illumination engineering (e.g., Wynn 2000a,b), and to determine surface optical properties (e.g., Stagg & Charalampopoulos 1991, Matchko & Gerhart 2005, Wellems et al. 2006). With some simplifying assumptions, we find that the peak around the specular direction is indeed caused by the specular component of the surface and is an artifact of the geometrical variability of the surface, not of the optical property

of the surface. The intensity of the light emerging from the system changes with surface roughness and approaches the horizon with increased incidence angle. No roughness effects in polarization are perceptible due to the fact that the effective Mueller matrices used merely shift the phase of the light (an ocean water Mueller matrix such as that empirically by Kokhanovsky 2003 could be used to enhance the effects of surface roughness). We expect, however, that significant effects will arise if absorption is included in the model.

CHAPTER 5

# EPILOGUE

In this brief closing chapter, we summarize our conclusions, reiterate the limitations of the approaches described in this work and investigate their potential for future improvements that may lead to investigations with applications outside the field of ocean optics.

## 5.1 Conclusions

One of the motivating issues addressed in this work is how the reflectance of a submerged underwater surface changes with roughness and how that change might affect remote observations. Since remote sensing in shallow water environments is most often done with nadir or near-nadir viewing, Part I (Chap. 2) considers an instrument viewing at nadir with sun-only illumination at varying incidence angles. The results indicate that the observed radiance from the underwater surface decreases substantially as roughness increases, but that there is very little change in the spectral character of the radiation. What spectral differences appear are small and are primarily due to the increase in the water optical path due to the roughened surface. For the cases discussed here, there are virtually no spectral effects on the surface reflectance as roughness changes even when second order reflections are considered.

The implication is that observations of bathymetry would be adversely affected if only one spectral band is used to extract depth or infer shape. If radiance decreases as depth increases, a rough area would appear deeper than a flat surface of the same material. On the other hand, it might be possible to develop a spectral algorithm to extract both depth and bottom type using several spectral bands. It

might even be possible to make some estimate of bottom roughness. For example, assuming that the water is homogeneous, consider the following four situations:

1. A flat bottom of the same material at different depths. In this case a single band would be sufficient to extract depth.

2. A bottom of the same material at the same depth, but with varying roughness. The brightness of the bottom would vary but the color would be close to invariant.

3. A bottom of the same material, now at different depths and varying roughness. Its brightness would change with both depth and roughness. If, however, the change is due to depth alone, then the spectral change is controlled entirely by the spectral variation induced by attenuation in the water.

4. Different bottoms of homogeneous material, at different depths and varying roughness. If the spectral character shows invariance then the brightness change is due to depth differences. If any spectral variation is perceptible and if it is different from what may be expected from the water type, then it is probably due to a change in bottom type.

The spectral invariance of the bottom as the roughness changes at a particular depth has only been considered for the case in which the roughness is small relative to the water depth. If the bottom undulations are large relative to the depth (i.e., $a \approx z$ in Fig. 2.1), the variations in optical path through the water could result in significant spectral differences.

Another finding is that second order reflections contribute weakly to the overall reflectance even for the roughest, but diffuse, surface considered. It is important to note that the surface roughness is modeled from a single-valued function and is

intended to mimic a relatively smoothly varying bottom. For very rough underwater surfaces, say, a coral reef, a seagrass bed, or a bottom covered with large rocks, higher order reflections might become more important and the spectral character of the bottom might have a more observable effect.

Finally, shadowing and obscuration result in significant changes in the magnitude of the reflectance that would have a more predictable, albeit non-Lambertian, effect otherwise. These will be significant for underwater observations at large viewing angles and so are likely to be insignificant for above-water, nadir-viewing instruments.

From results in Part II (Chap. 3), the nadir-viewing reflectance change is strongly dependent on the amplitude-to-period ratio of the defining waveform of the surface but very little on the relative distance between the surface and a detector of fixed viewing half-angle. The deviation away from the nadir-viewing Lambertian value varies wildly with increasing roughness in the near field but approaches a stable limit when the detector is far enough away from the surface. This information may be useful when the effective roughness dimension is larger than the instrument field of view, i.e., when the surface is in the near field. For a submerged surface in clear shallow water near-field effects will be apparent through the air-water interface and the observed reflectance may not be easily related to a far-field value.

The way the bidirectional reflectance distribution function (BRDF) changes with roughness is of primary concern for in-water observations, but has interesting implications for remote sensing farther afield. It appears that the darkening of a surface observed by a remote system is due to the redistribution of light into the retroreflection and forward scattering directions, both of which have been observed

in laboratory experiments. The retroreflection peak is common to all diffuse but rough surfaces. One implication of the variation in the BRDF is that bottom roughness effects are more detectable in the retroreflection direction but, unlike the nadir-viewing situation, reflectance should increase with increasing roughness. This suggests that a dual-direction sensing system may be able to distinguish roughness variations more effectively than a nadir-viewing instrument alone. The increase in retroreflectance and the decrease in nadir reflectance with roughness is expected to be highly correlated. Again, if roughness and only roughness (not depth or bottom type) is changing, then the spectral variations should be minimal.

Finally, the behavior of specular reflections from a system with rough surfaces is studied. Part III (Chap. 4) is a preliminary attempt to separate the effects of the distribution of specular reflectance from that of diffuse reflectance. The formulation using Mueller matrices and Stokes vectors includes polarization effects that could not have easily been handled using other formulations. While this effort did not produce any remarkably new results, the model predictions did meet expectations and matched published observations and Monte Carlo simulations. The intensity of light emerging from the system is expected to carry the effects of all the roughness interactions. The speckle area increases with increasing surface roughness as its peak moves toward the horizon faster than the specular direction with increasing sun angle. With absorption ignored, however, there is negligible change in the polarization patterns.

## 5.2 Limitations

> "My sense of smell is far more sensitive than my sense of sight. I wish I could smell the polarization of light."
>
> *Wendy in 2007*

The limitations encountered are consequences of the simplifications that make the problems more tractable. In the two-dimensional model, all the scattering happens in the solar plane and although the largest greatest changes are expected to happen here, the orientation of remote sensing systems in the natural environment cannot always happen along this alignment, nor are the surfaces of interest conveniently aligned. The extension into three dimensions is a step that remedies this as well as facilitates the analysis of the full hemispherical distribution of reflection and transmission directions. The symmetry along the solar plane, however, facilitates the analysis of the reflectance distributions, so even as the directions of the water surface and bottom surface roughness are allowed to be aligned away from the solar plane none of those results are analyzed here.

Light is assumed to be collimated but incoherent; no interference effects are allowed. Except for a brief inclusion of sand reflectance in the visible range, spectral variations in the system have been ignored and so no cross-spectral effects could have been observed (e.g., the aureole effect; Minnaert 1948, Luchinin & Sergiyevskiy 1986, Walker 1994, p. 502). Factors that may be significant to the change of the apparent reflectance of a submerged underwater surface but that have been ignored include: diffraction (Hoover & Gamiz 2006), volume scattering, absorption and total internal reflection (Plass et al. 1975). Another simplifying assumption is the random polarization of the incident light. While this is a rea-

sonable assumption for sunlight, light from the sky almost always is somewhat polarized.

In terms of surface geometry, our realizations have been confined to sinusoids, except for the randomized slope distribution of the water surface. Although we can account for shadowing and obscuration the surface must be a single-valued, differentiable function. Thus, we cannot model surfaces with cavities, fall offs or sharp edges. Furthermore, the technique of representing the surface of interest by a point in space with a variation of tilts does not hold any spatial memory. A point on the surface does not know whether a point adjacent to is tilted in some way as to be able to contribute to interreflections, for example. Where there is some spatial memory, the model is simplified so that the detector only looks straight down at the surface and so no bidirectional reflectance distribution can be constructed. No inhomogeneities have been allowed on the surfaces, and thus our model surfaces can hardly be said to mimic the material characteristics of realistic natural surfaces.

No effort has been made to model the overall reflectance change due to, say, first and second order reflections, or both the diffuse and specular components of reflectance together. Although the dissection may facilitate an understanding of the different factors affecting light by separating their effects out, it does not help provide a stronger intuition on what may actually be happening in the natural environment. Furthermore, not all the light lost in the system due to roughness by shadowing or obscuration and interreflections are accounted for.

The results of the reflectance and polarization distributions are presented on generalized polar plots. Depending on the location of the detector and the ori-

entation of its optical axes, the distributions may be distorted and thus may be slightly misleading.

## 5.3 Future prospects

"To infinity, and beyond!"

*Buzz Lightyear*

The apparent reflectance of a surface is a function also of illumination conditions, among other things, and in the natural environment this is dominated by sun and sky contributions. Many aspects of these illumination sources are well-known and theoretical expressions have been derived. Effects of the variability in illumination will be included in future investigations of reflectance changes from both diffuse and specular but rough surfaces.

An almost-ready question to consider is how absorption might affect the polarization of a system such as an air-water-bottom system. How can absorption, as a pathlength problem, be included in a model that does not have spatial memory? Is it even possible? Using the approach in Part III, how different would the diffuse behavior of a submerged rough surface be? The inclusion of a diffuse component would be an increase in the problem dimension but it is expected to be a trivial step. An important supplement though is to compare theoretical results with some measurements, be it of the diffuseness or specular reflectance property or polarization effects of a surface. At the next opportunity, a few more questions will be addressed:

1. How can polarizers be used to discriminate surfaces?

2. Is there an optimum polarization angle that would provide the most information?

3. Is it possible to derive surface roughness given a reflectance map?

4. What is the importance of the orientation of the polarization ellipse, and how can this be manipulated in active sensing to enhance the information about the surface from the radiance in a scene?

APPENDIX A

# RELEVANT CALCULUS

Physicists and engineers tend to make liberal use of the approximation of $\Delta x$ by $dx$.

*Larson et al., 2006, in Calculus with Analytic Geometry*

## A.1 Open extended formula for integration

The following is an open "extended" formula with the same order as Simpson's rule:

$$\int_{x_1}^{x_N} f(x)dx = h\left[\frac{55}{24}f_2 - \frac{1}{6}f_3 + \frac{11}{8}f_4 + f_5 + f_6 + f_7 + \ldots + f_{N-5} + f_{N-4} + \frac{11}{8}f_{N-3} - \frac{1}{6}f_{N-2} + \frac{55}{24}f_{N-1}\right] + O\left(\frac{1}{N^4}\right) . \quad \text{(A.1)}$$

It is taken from *Numerical Recipes in FORTRAN 77* by Press et al. (1992), available online at http://www.nr.com.

## A.2 Mean Value Theorem for double integration

Let $R$ be an elementary region in $\mathbb{R}^2$. Furthermore, let $f$ be a continuous function in $R$ then there exists a point $(x_0, y_0)$ in $R$ such that

$$\iint_R f(x,y)\,dx\,dy = f(x_0,y_0)A(R) , \quad \text{(A.2)}$$

where the area of $R$ is given by

$$\iint_R dx\,dy = A(R) , \quad \text{(A.3)}$$

and $f(x_0, y_0)$ gives the mean value of the function.

## A.3 Straubel's invariant

Let $n_1$ and $n_2$ be the indices of refraction of the first and second medium, respectively. Furthermore, let $\chi_1$ be the incidence angle and $\chi_2$ the transmission angle, both with respect to the surface facet normal, $\vec{r}_n$, in the reflection-transmission plane. Squaring both sides of Snell's law (used in Eqs. 2.27, 2.28, 4.57, 4.59, 4.79) gives

$$n_1{}^2 \sin^2 \chi_1 = n_2{}^2 \sin^2 \chi_2 \ . \tag{A.4}$$

Taking the differentials with respect to $\chi_1$ and $\chi_2$ on either side, we have

$$n_1{}^2 \big(2 \cos \chi_1 \sin \chi_2\big)\, d\chi_1 = n_2{}^2 \big(2 \cos \chi_2 \sin \chi_2\big)\, d\chi_2 \tag{A.5}$$

$$n_1{}^2 \cos \chi_1 \sin \chi_1\, d\chi_1 = n_2{}^2 \cos \chi_2 \sin \chi_2\, d\chi_2 \ . \tag{A.6}$$

Recall that any given direction in the global reference system is indicated by the angle pair $(\theta, \phi)$, where $\theta$ is the angle from zenith (positive $z$-axis) and $\phi$ the azimuth (from the $x$-axis). A differential element of solid angle $\Omega(\theta, \phi)$ about $(\theta, \phi)$ is given by

$$d\Omega(\theta, \phi) = \sin \theta\, d\theta\, d\phi \ . \tag{A.7}$$

If the reflection-transmission plane were aligned with the solar plane ($\phi = 0$ or $\pi$) then $\theta = \chi$ and the reflection solid angle and the transmission solid angle are respectively given by

$$d\Omega_1 = \sin \chi_1\, d\chi_1\, d\phi_1 \tag{A.8}$$

and

$$d\Omega_2 = \sin \chi_2\, d\chi_2\, d\phi_2 \ . \tag{A.9}$$

Substituting into Eq. A.6,

$$n_1{}^2 \cos \chi_1 \frac{d\Omega_1}{d\chi_1\, d\phi_1}\, d\chi_1 = n_2{}^2 \cos \chi_2 \frac{d\Omega_2}{d\chi_2\, d\phi_2}\, d\chi_2 \ , \tag{A.10}$$

however $\phi_1 = \phi_2$, so that

$$n_1{}^2 \cos\chi_1 \, d\Omega_1 = n_2{}^2 \cos\chi_2 \, d\Omega_2 \tag{A.11}$$

$$d\Omega_1 = \left(\frac{n_2}{n_1}\right)^2 \frac{\cos\chi_2}{\cos\chi_1} \, d\Omega_2 \; . \tag{A.12}$$

This final equation is known as Straubel's invariant. It relates the change in the size of the solid angle through transmission from the first medium to the second medium to the indices of refraction and the cosine of the reflection and transmission angles. A simple proof using the Jacobian matrix is given by, e.g., Germer (2003, Eq. 15).

## A.4 Extension of the vector triple product

Let the unit vectors $\vec{a}$, $\vec{b}$ and $\vec{c}$ that share the same origin lie on a plane. Let the vectors be located respective to each other so that a normal to the plane can be described by $\vec{a} \times \vec{b}$ and $\vec{b} \times \vec{c}$, pointing in the same direction. If $\theta_{ab}$ is the angle between $\vec{a}$ and $\vec{b}$ and $\theta_{bc}$ between $\vec{b}$ and $\vec{c}$, then in general the unit normal vector to the plane from the origin is

$$\frac{\vec{a} \times \vec{b}}{\left\|\vec{a}\right\| \left\|\vec{b}\right\| \sin\theta_{ab}} = \frac{\vec{b} \times \vec{c}}{\left\|\vec{b}\right\| \left\|\vec{c}\right\| \sin\theta_{bc}} \; . \tag{A.13}$$

The vectors are of unit length so

$$\frac{\vec{a} \times \vec{b}}{\sin\theta_{ab}} = \frac{\vec{b} \times \vec{c}}{\sin\theta_{bc}} \; . \tag{A.14}$$

If any two of the vectors $\vec{a}$, $\vec{b}$ and $\vec{c}$ are known and the angles $\theta_{ab}$ and $\theta_{bc}$ can be determined, then we can solve for the third vector. Say $\vec{b}$ is unknown, then a vector *on* the plane can be described by

$$\vec{b} \times \left(\frac{\vec{a} \times \vec{b}}{\sin\theta_{ab}}\right) = \vec{b} \times \left(\frac{\vec{b} \times \vec{c}}{\sin\theta_{bc}}\right) \; . \tag{A.15}$$

This is an extension of the use of the vector triple product, and with a little algebra $\vec{b}$ is determined thus:

$$\frac{1}{\sin\theta_{ab}}\left[\vec{b}\times(\vec{a}\times\vec{b})\right]=\frac{1}{\sin\theta_{bc}}\left[\vec{b}\times(\vec{b}\times\vec{c})\right] \tag{A.16}$$

$$\frac{1}{\sin\theta_{ab}}\left[(\vec{b}\cdot\vec{b})\vec{a}-(\vec{b}\cdot\vec{a})\vec{b}\right]=\frac{1}{\sin\theta_{bc}}\left[(\vec{b}\cdot\vec{c})\vec{b}-(\vec{b}\cdot\vec{b})\vec{c}\right] \tag{A.17}$$

$$\left(\frac{1}{\sin\theta_{ab}}\right)\vec{a}-\left(\frac{1}{\sin\theta_{ab}}\cos\theta_{ab}\right)\vec{b}=\left(\frac{1}{\sin\theta_{bc}}\cos\theta_{bc}\right)\vec{b}-\left(\frac{1}{\sin\theta_{bc}}\right)\vec{c} \tag{A.18}$$

$$\left(\frac{\cos\theta_{bc}}{\sin\theta_{bc}}+\frac{\cos\theta_{ab}}{\sin\theta_{ab}}\right)\vec{b}=\left(\frac{1}{\sin\theta_{ab}}\right)\vec{a}-\left(\frac{1}{\sin\theta_{bc}}\right)\vec{c} \tag{A.19}$$

$$\vec{b}=\frac{1}{\cot\theta_{bc}+\cot\theta_{ab}}\left[\big(\sec\theta_{ab}\big)\vec{a}-\big(\sec\theta_{bc}\big)\vec{c}\right]. \tag{A.20}$$

APPENDIX B

**SOME MATLAB PROGRAMS**

## B.1 Far-field reflectance

The MATLAB function `reffar.m` as developed and described in Sec. 3.5.

```
function f = refffar(ths,phs,a,L);

% REFFFAR returns the percent reflectance
%   of an egg-carton surface compared with
%   a flat surface, where
% THS is the incoming zenith incidence angle,
% PHS the incoming azimuth incidence angle,
% A the amplitude of the waveform, and
% L the length of the waveform.
%
% Written by W. R. Clavano, 04 October 2006,
%   revised 18 October 2006, 23 April 2007.

% Example:
% f = refffar(10,90,0.2,1.1);

% Incidence direction:
ths = deg2rad(ths);
phs = deg2rad(phs);

% Vector representation:
xs = sin(ths)*cos(phs);
ys = sin(ths)*sin(phs);
zs = cos(ths);

% Taking the dot product of the incidence angle
%   and the normal at each point on the surface
%   divided by the product of their lengths:
F = @(x,y) (-a*xs*2*pi/L*cos(2*pi/L*x).*cos(2*pi/L*y)./ ...
    sqrt(1 + (a*2*pi/L*cos(2*pi/L*x).*cos(2*pi/L*y)).^2 +...
    (a*2*pi/L*sin(2*pi/L*x).*sin(2*pi/L*y)).^2)) +...
    (a*ys*2*pi/L*sin(2*pi/L*x).*sin(2*pi/L*y)./ ...
    sqrt(1 + (a*2*pi/L*cos(2*pi/L*x).*cos(2*pi/L*y)).^2 +...
    (a*2*pi/L*sin(2*pi/L*x).*sin(2*pi/L*y)).^2)) + ...
```

```
    (1*zs./sqrt(1 + (a*2*pi/L*cos(2*pi/L*x).*cos(2*pi/L*y)).^2 +...
    (a*2*pi/L*sin(2*pi/L*x).*sin(2*pi/L*y)).^2));

xmin = -10*L;
xmax = 10*L;
ymin = -10*L;
ymax = 10*L;
AS = (xmax - xmin)*(ymax - ymin);

f = dblquad(F,xmin,xmax,ymin,ymax)/AS;
```

## B.2 Near-field reflectance

The MATLAB function `refnear.m` as developed and described in Sec. 3.6.

```
function f = reffnear(ths,phs,a,L,r1,r2,r3);

% REFFNEAR returns the percent reflectance
%   of an egg-carton surface compared with
%   a flat surface in the NEAR FIELD, where
% THS is the incoming zenith incidence angle,
% PHS the incoming azimuth incidence angle,
% A the amplitude of the waveform, and
% L the length of the waveform;
% (R1,R2,R3) provide the location of the
%   detector in Cartesian space.
%
% Written by W. R. Clavano, 17 October 2006.

% Example:
% f = reffnear(10,90,0.2,1.1,1.1/3,0,6);

ths = deg2rad(ths);
phs = deg2rad(phs);

xs = sin(ths)*cos(phs);
ys = sin(ths)*sin(phs);
zs = cos(ths);

thd = 5; thd = deg2rad(thd); % Detector half-angle.
```

```
r = r3*tan(thd);

pp = 100;
qq = 100;

dX = 2*r/pp;
X = linspace(2*r/pp,(r1 + r) - 2*r/pp, ...
    pp - 1)';

Y2 = r2 + sqrt(r^2 - (X - r1).^2);
Y1 = r2 - sqrt(r^2 - (X - r1).^2);
dY = 1/qq*(Y2 - Y1);
Y = repmat(dY,[1,qq - 1]) + 1/(qq - 2)* ...
    (Y2 - 2/qq*(Y2 - Y1))*[0:qq - 2];

X = repmat(X,1,qq - 1);
t = (-2*pi/L*a*sin(ths)*cos(phs)*cos(2*pi/L*X).*cos(2*pi/L*Y))./...
    sqrt(1 + (2*pi/L*a*cos(2*pi/L*X).*cos(2*pi/L*Y)).^2 + ...
    (-2*pi/L*a*sin(2*pi/L*X).*sin(2*pi/L*Y)).^2) + ...
    (2*pi/L*a*sin(ths)*sin(phs)*sin(2*pi/L*X).*sin(2*pi/L*Y))./...
    sqrt(1 + (2*pi/L*a*cos(2*pi/L*X).*cos(2*pi/L*Y)).^2 + ...
    (-2*pi/L*a*sin(2*pi/L*X).*sin(2*pi/L*Y)).^2) + ...
    (cos(ths))./ ...
    sqrt(1 + (2*pi/L*a*cos(2*pi/L*X).*cos(2*pi/L*Y)).^2 + ...
    (-2*pi/L*a*sin(2*pi/L*X).*sin(2*pi/L*Y)).^2);
dY = repmat(dY,1,qq - 1);
tdY = t.*dY;

Oqq = repmat([55/24,-1/6,11/8,ones(1, ...
    qq - 6 - 1),11/8,-1/6,55/24], ...
    [pp - 1,1]);
Opp = [55/24,-1/6,11/8,ones(1, ...
    pp - 6 - 1),11/8,-1/6,55/24]';

sumtdY = sum(Oqq.*tdY,2);

AX = dX*sumtdY;
f = sum(Opp.*AX);
f = f/(pi*r^2);
```

## B.3 Theoretical sky luminance distributions

The standard from ISO (2004) provides the luminance distribution in terms of the ratio relative to the value at zenith:

$$\frac{L_a}{L_z} = \frac{\left[\begin{array}{rcl} 1 & + & c^*\Big( \exp\Big\{ d^*\Big[ \cos^{-1}\big( \cos\theta_s \cos\theta_k \\ & + & \sin\theta_s \sin\theta_k \cos|\phi_k - \phi_s| \big)\Big]\Big\} \exp\Big[ d^* \dfrac{\pi}{2}\Big] \Big) \\ & + & e^* \cos^2\big[ \cos^{-1}(\cos\theta_s \cos\theta_k \sin\theta_s \sin\theta_k \cos|\phi_k - \phi_s|)\big] \end{array}\right]}{\Big\{1 + c^*\Big[ \exp(d^*\theta_s) - \exp\Big(d^* \dfrac{\pi}{2}\Big)\Big] + e^* \cos^2\theta_s\Big\}\{1 + a^* \exp b^*\}}\,, \quad \text{(B.1)}$$

where the polar angle pair $(\theta_k, \phi_k)$ represents the direction of the source from a hemispherical sky and $a^*$, $b^*$, $c^*$, $d^*$ and $e^*$ are constants with values given in the program below. For our purpose, we normalize the sky radiance to the brightest point in the sky (most often in the direction of the sun):

$$L_{\text{sky}}(\theta_k, \phi_k) = \frac{\dfrac{L_a}{L_z}}{\max\left(\dfrac{L_a}{L_z}\right)}\,. \quad \text{(B.2)}$$

The following is the MATLAB function called `skylumdist.m` that returns the normalized sky luminance distribution, $L_{\text{sky}}$:

```
function F = skylumdist(zeta_s,alpha_s,dome,tinc,pinc,skytype);

% SKYLUMDIST returns the relative sky luminance distribution given
%   ZETA_S angle from vertical (zenith) [degrees],
%   ALPHA_S angle from north (azimuth) [degrees],
%   DOME output type: 0 for polar plot or 1 for spherical plot,
%   TINC increment for zenith angles [degrees], and
%   PINC increment for azimuth angles [degrees].
%
% Example: La_Lz = skylumdist(30,90,1,10,2);
%
% Written by W. R. Clavano, 06 April 2005.
%   Based on Standard No. 15469, ‘‘Spatial distribution of
%   daylight--CIE standard general sky’’, International
%   Organization for Standardization (ISO),
```

```
%   Geneva, Switzerland. Second edition. ISO 15469:2004(E).
%
% Much gratitude to Mary Patterson at the Cornell University
%   Engineering Library for help in acquiring a copy of the
%   standard.

skytypes = strvcat( ...
    '1: CIE Standard Overcast Sky, Steep luminance gradation
         towards zenith, azimuthal uniformity', ...
    '2: Overcast, with steep luminance gradation and slight
         brightening towards the sun', ...
    '3: Overcast, moderately graded with azimuthal uniformity', ...
    '4: Overcast, moderately graded and slight brightening towards
         the sun', ...
    '5: Sky of uniform luminance', ...
    '6: Partly cloudy sky, no gradation towards zenith, slight
         brightening towards the sun', ...
    '7: Partly cloudy sky, no gradation towards zenith, brighter
         circumsolar region', ...
    '8: Partly cloudy sky, no gradation towards zenith, distinct
         solar corona', ...
    '9: Partly cloudy, with the sun obscured', ...
    '10: Partly cloudy, with brighter circumsolar region', ...
    '11: White-blue sky with distinct solar corona', ...
    '12: CIE Standard Clear Sky, low luminance turbidity', ...
    '13: CIE Standard Clear Sky, polluted atmosphere', ...
    '14: Cloudless turbid sky with broad solar corona', ...
    '15: White-blue turbid sky with broad solar corona', ...
    '16: Standard Overcast Sky of CIE S003/E-1996');

disp('Sky types as defined in the ISO 15469 standard:')
disp(skytypes)
skytype = input('Enter sky type: ');
if isempty(skytype)
    skytype = 1;
end

if nargin < 5, pinc = 2; end
if nargin < 4, tinc = 10; end

skyparameters = skyparameters; % input parameters for sky types

[theta,phi] = meshgrid([0.5:tinc:360,0.5]*pi/180, ...
    [0.5:pinc:90,89]*pi/180);
```

```
gamma = phi;
zeta = pi/2 - gamma;
alpha = 2*pi - theta;

if dome == 0
    [xc,yc] = pol2cart(alpha,zeta);
else
    [x,y,z] = sph2cart(alpha,zeta,ones(size(zeta)));
end

zeta_s = zeta_s*pi/180;
alpha_s = 2*pi - alpha_s*pi/180;

if dome==0,
    [xcs,ycs] = pol2cart(alpha_s,zeta_s);
else
    [xs,ys,zs] = sph2cart(alpha_s,pi/2 - zeta_s,1);
end

if skytype<16,

    a = skyparameters(skytype,2);
    b = skyparameters(skytype,3);
    c = skyparameters(skytype,4);
    d = skyparameters(skytype,5);
    e = skyparameters(skytype,6);

    chi = acos(cos(zeta_s)*cos(zeta) + sin(zeta_s)*sin(zeta).* ...
        cos(abs(alpha - alpha_s)));

    phiz = zeros(size(zeta));
    phiz(zeta~=pi/2) = 1 + a*exp(b./cos(zeta(zeta~=pi/2)));
    phiz(zeta==pi/2) = 1;
    phi0 = 1+ a*exp(b);

    fchi = zeros(size(chi));
    fchi = 1 + c*(exp(d*chi) - exp(d*pi/2)) + e*cos(chi).^2;
    fzs = 1 + c*(exp(d*zeta_s) - exp(d*pi/2)) + e*cos(zeta_s)^2;

    La_Lz =fchi.*phiz./(fzs*phi0);

else

    La_Lz = (1 + 2*sin(gamma))/3;
```

```
end

F = La_Lz./max(max(La_Lz));

figurex = figure;
if dome==0,
    [C,h] = contourf(xc,yc,F,15);
    for i = 1:length(h);
        set(h(i),'LineStyle','none')
    end
    hold on,
    plot3(xcs,ycs,max(max(F)),'ko')
    plot(0,0,'k+')
    view([-180,90])
    htitle = title(char(cellstr(skytypes(skytype,:))));
    set(htitle,'Position', ...
        [-0.004988904409823913,1.8359254267187832, ...
        23.145740219070138], ...
        'HorizontalAlignment','center')
    text(1.5,-1,'\uparrow N','Position', ...
        [0.07483,-1.686,23.145740219070138])
    text(1.75,0,strcat('Sun(\theta,\pphi) = (', ...
        num2str(zeta_s*180/pi),',', ...
        num2str((2*pi - alpha_s)*180/pi),')'), ...
        'HorizontalAlignment','center','Position', ...
        [1.601,-1.327,23.145740219070138]);
    axis off

else
    surf(x,y,z,F);
    shading interp
    hold on,
    plot3(xs,ys,zs,'Color',[0.5,0.5,0.5], ...
        'Marker','o','MarkerFaceColor','w')
    view([-180,90])
    htitle = title(char(cellstr(skytypes(skytype,:))));
    axis off
end

axis equal
axis tight

grid off
```

```
hbar = colorbar;
axes(hbar)
title('L_{a}/L_{z} [Rel Units]','Parent',hbar)
set(gcf,'Color','none')

function skyparameters = skyparameters;
skyparameters = [ ...
    1.0000     4.0000   -0.7000    0        -1.0000    0
    2.0000     4.0000   -0.7000    2.0000   -1.5000    0.1500
    3.0000     1.1000   -0.8000    0        -1.0000    0
    4.0000     1.1000   -0.8000    2.0000   -1.5000    0.1500
    5.0000     0        -1.0000    0        -1.0000    0
    6.0000     0        -1.0000    2.0000   -1.5000    0.1500
    7.0000     0        -1.0000    5.0000   -2.5000    0.3000
    8.0000     0        -1.0000   10.0000   -3.0000    0.4500
    9.0000    -1.0000   -0.5500    2.0000   -1.5000    0.1500
    10.0000   -1.0000   -0.5500    5.0000   -2.5000    0.3000
    11.0000   -1.0000   -0.5500   10.0000   -3.0000    0.4500
    12.0000   -1.0000   -0.3200   10.0000   -3.0000    0.4500
    13.0000   -1.0000   -0.3200   16.0000   -3.0000    0.3000
    14.0000   -1.0000   -0.1500   16.0000   -3.0000    0.3000
    15.0000   -1.0000   -0.1500   24.0000   -2.8000    0.1500];
```

APPENDIX C

# LIMITS AND APPROXIMATIONS

## C.1 The limit of the transmission function

What is the limit of the transmission function of a dielectric interface as the incidence angle approaches the refracted angle?

The transmission function determines the ratio of the amount of (randomly polarized) light that is transmitted through the boundary of two different media, the rest is assumed to be reflected off the surface. In our case, we are interested in the boundary between air and water, where light travels in air and hits the water surface and is subsequently refracted into the water. This function is defined by considering linearly polarized light of which the electric vectors are perpendicular and parallel to the plane of incidence with a surface and can be found in any standard optics textbook. (For partially polarized incident skylight, consider the transmissivity of the air-water interface as given by Horváth & Varjú 1995, Appendix C.)

For our purpose, we define a relative index of refraction of the medium to air: $n = n_2/n_1$. Using Snell's law the angle at transmission is given by $\theta_t = \sin^{-1}(n \sin\theta_i)$, where $\theta_i$ is the angle the light makes on the water surface relative to the normal. The transmission function is given by

$$\tau(\theta_i, \theta_t) = 1 - \left\{ 0.5 \left[ \frac{\sin(\theta_t - \theta_i)}{\sin(\theta_t + \theta_i)} \right]^2 + 0.5 \left[ \frac{\tan(\theta_t - \theta_i)}{\tan(\theta_t + \theta_i)} \right]^2 \right\} \tag{C.1}$$

What is the limit of this function when $\theta_i$ approaches $\theta_t$? For the sine and tangent functions, the limit goes to zero.

Consider the fraction involving the sine functions first. The limit of both the numerator and denominator goes to zero. Applying l'Hôpital's rule, which states

that the limit of the ratio of two functions is equal to the limit of the ratio of the rates of change of the functions, we have

$$\lim_{\theta_i \to \theta_t} \frac{\sin(\theta_t - \theta_i)}{\sin(\theta_t + \theta_i)} = \lim_{\theta_i \to \theta_t} \left[ \frac{\cos(\theta_t - \theta_i)}{\cos(\theta_t + \theta_i)} \frac{(\theta_t' - 1)}{(\theta_t' + 1)} \right] . \tag{C.2}$$

The cosine identities

$$\cos(\theta_t - \theta_i) = \cos\theta_t \cos\theta_i + \sin\theta_t \sin\theta_i \tag{C.3}$$

and

$$\cos(\theta_t + \theta_i) = \cos\theta_t \cos\theta_i - \sin\theta_t \sin\theta_i \tag{C.4}$$

suggest that the limit of the fraction involving cosines goes to unity. Furthermore, let $u = n \sin\theta_i$ and $\theta_t = v = \sin^{-1} u$, so that

$$dv = \frac{du}{\sqrt{1 - u^2}} \tag{C.5}$$

and

$$\theta_t{}' = \frac{n \cos\theta_i}{\sqrt{1 - n^2 \sin^2\theta_i}} . \tag{C.6}$$

Substituting $\theta_t$ and $\theta_t{}'$ into Eq. C.2, we have

$$\lim_{\theta_i \to 0} \frac{\sin\left[\sin^{-1}(n\sin\theta_i) - \theta_i\right]}{\sin\left[\sin^{-1}(n\sin\theta_i) + \theta_i\right]} = \lim_{\theta_i \to 0} \frac{\dfrac{n\cos\theta_i}{\sqrt{1 - n^2\sin^2\theta_i}} - 1}{\dfrac{n\cos\theta_i}{\sqrt{1 - n^2\sin^2\theta_i}} + 1} \tag{C.7}$$

$$= \lim_{\theta_i \to 0} \frac{n\cos\theta_i - \sqrt{1 - n^2\sin^2\theta_i}}{n\cos\theta_i + \sqrt{1 - n^2\sin^2\theta_i}} \tag{C.8}$$

$$= \frac{n-1}{n+1} . \tag{C.9}$$

The limit is, quite nicely, dependent only on the relative index of refraction of water to air.

Similarly, we deal with the fraction involving tangent functions:

$$\lim_{\theta_i \to \theta_t} \frac{\tan(\theta_t - \theta_i)}{\tan(\theta_t + \theta_i)} = \lim_{\theta_i \to \theta_t} \left[ \frac{\sec^2(\theta_t - \theta_i)}{\sec^2(\theta_t + \theta_i)} \frac{(\theta_t' - 1)}{(\theta_t' + 1)} \right] \tag{C.10}$$

$$= \lim_{\theta_i \to \theta_t} \left[ \frac{\dfrac{\theta_t' - 1}{\cos^2(\theta_t - \theta_i)}}{\dfrac{\theta_t' + 1}{\cos^2(\theta_t + \theta_i)}} \right] . \tag{C.11}$$

The limit of the square of each of the cosine functions goes to unity. Again we are left with the form on the right-hand side of Eq. C.9 and get the same limit. Thus, the limit of the transmission function as the direction of incidence approaches the transmission direction is

$$\lim_{\theta_i \to \theta_t} \tau(\theta_i, \theta_t) = 1 - \left[ 0.5 \left( \frac{n-1}{n+1} \right)^2 + 0.5 \left( \frac{n-1}{n+1} \right)^2 \right] = 1 - \left( \frac{n-1}{n+1} \right)^2 . \tag{C.12}$$

## C.2 The size of the source disk

Given an incidence direction at an angle $\chi$ from the facet normal at a point $(x_0, y_0)$ on the surface, the unit vector describing the incidence direction is expressed in component form as

$$\vec{r}_{0(x_0,y_0)} = 0\,\vec{\mathrm{i}} - \sin\chi\,\vec{\mathrm{j}} - \cos\chi\,\vec{\mathrm{k}} . \tag{C.13}$$

The unit normal vector at any point on the surface is

$$\vec{r}_{n(x_0,y_0)} = -z_{x'}\,\vec{\mathrm{i}} - z_{y'}\,\vec{\mathrm{j}} + \vec{\mathrm{k}} , \tag{C.14}$$

where $z_{x'} = f_{x'}(x_0, y_0)$ in the sense of Eq. 4.23 and $z_{y'} = f_{y'}(x_0, y_0)$ of Eq. 4.24. In general, from the Fresnel equations the reflection direction in the scattering plane is

$$\vec{r}_{1(x_0,y_0)} = 0\,\vec{\mathrm{i}} - \sin\chi\,\vec{\mathrm{j}} + \cos\chi\,\vec{\mathrm{k}} . \tag{C.15}$$

The direction $\vec{r}_{0(x_0,y_0)}$ is centered around 0 on the source "disk", see Fig. C.1. Initially, we consider it here for the solar disk but extend the concept for any other

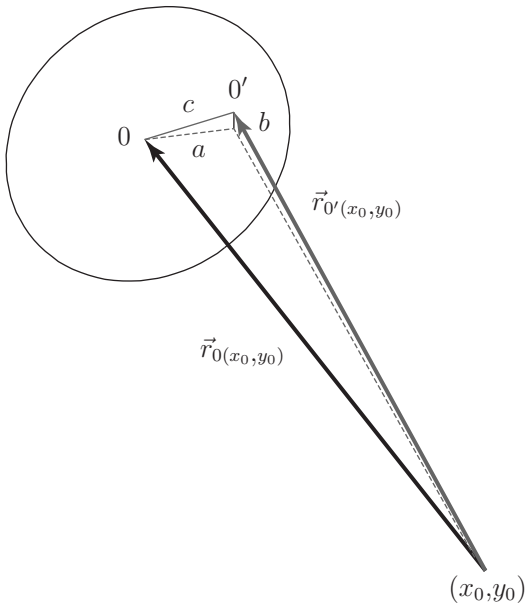


Figure C.1: Sketch of off-center source point.

source centered around a point in the sky. If we were to take a different point on the source disk, say $0'$, the incidence direction at $(x_0, y_0)$ would change to $\vec{r}_{0'(x_0,y_0)}$. Let the new point $0'$ be a distance $c$ away from 0. Using the global reference plane, an observer at $(x_0, y_0)$ could perceive this change as an azimuthal rotation through $a$ and a change in tilt of approximately an angle $b$.

Recall that the directional vectors are of unit length. The azimuthal shift at an angle $a$ can be approximated by the projected distance $a$ on the solar disk as viewed from $(x_0, y_0)$, see Fig. C.2, assuming that $a$ is very small. This can also be approximated by the vector

$$\vec{a} = a\,\vec{\mathrm{i}} + 0\,\vec{\mathrm{j}} + 0\,\vec{\mathrm{k}}\,. \tag{C.16}$$

The change in tilt $b$ is represented by transforming $\vec{r}_{0(x_0,y_0)}$ a projected distance of approximately $b$ as observed from $(x_0, y_0)$ in Fig. C.3. Using the small-angle

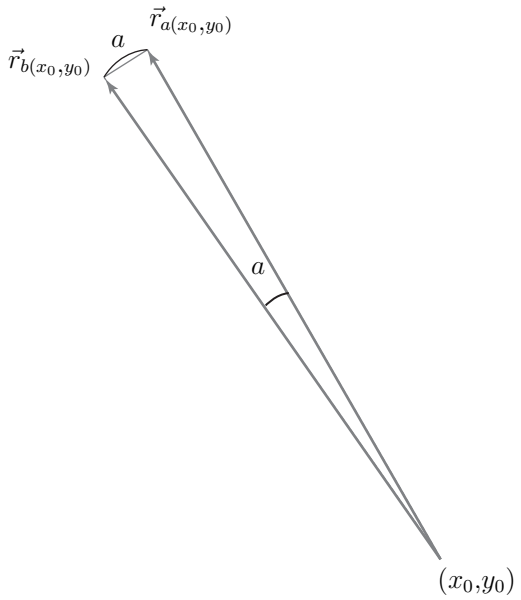


Figure C.2: Estimating the distance $a$ between two points on a source disk.

approximation, where as $b \to 0$

$$\cos b \approx 1 \tag{C.17}$$

and

$$\sin b \approx b \; . \tag{C.18}$$

The horizontal displacement on the transformed incidence plane is

$$\sin \chi - \sin(\chi - b) \tag{C.19}$$

$$\sin \chi - \sin \chi - b \cos \chi \tag{C.20}$$

$$- b \cos \chi \; , \tag{C.21}$$

and the vertical displacement is

$$\cos(\chi - b) - \cos \chi \tag{C.22}$$

$$\cos \chi + b \sin \chi - \cos \chi \tag{C.23}$$

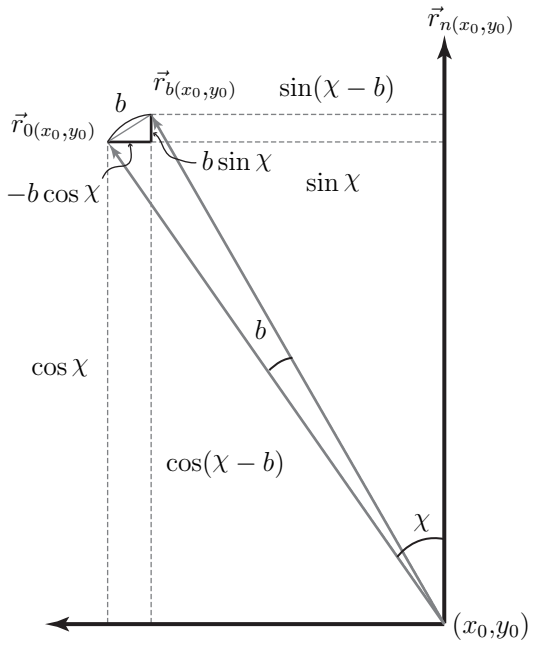


Figure C.3: Estimating the distance $b$ between two points on a source disk.

$$b\sin\chi\ . \tag{C.24}$$

This displacement can be described then by the vector

$$\vec{b} = 0\,\vec{\mathrm{i}} - b\cos\chi\,\vec{\mathrm{j}} + b\sin\chi\vec{\mathrm{k}}\ . \tag{C.25}$$

The total displacement $c$ in Fig. C.3 can be described by the vector

$$\vec{c} = \vec{a} + \vec{b}\ . \tag{C.26}$$

and the transformed incidence vector from the center of the source disk 0 to a point off-center at $0'$ is

$$\begin{aligned}\vec{r}_{0'(x_0,y_0)} &= \vec{r}_{0(x_0,y_0)} + \vec{c} \\ &= a\,\vec{\mathrm{i}} + \big(-\sin\chi - b\cos\chi\big)\,\vec{\mathrm{j}} + \big(-\cos\chi + b\sin\chi\big)\,\vec{\mathrm{k}}\ .\end{aligned} \tag{C.27}$$

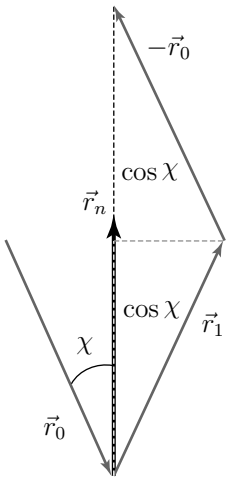


Figure C.4: Vector law of reflection.

Let the unit vectors be

$\vec{r}_0$ the incidence vector,

$\vec{r}_n$ the normal vector, and

$\vec{r}_1$ the reflection vector.

From the Fresnel equations, we have

$$\vec{r}_1 - \vec{r}_0 = \big(2\cos\chi\big)\vec{r}_n \ , \tag{C.28}$$

where $\chi$ is the angle of incidence in the plane of reflection, see Fig. C.4.

For the transformed incidence direction, using Eqs. C.15 and C.27, and factoring out $2\cos\chi$,

$$\begin{aligned}
\vec{r}_1 - \vec{r}_{0'} &= -a\,\vec{\mathrm{i}} + b\cos\chi\,\vec{\mathrm{j}} + \big(2\cos\chi - b\sin\chi\big)\vec{\mathrm{k}} \\
&= \big(2\cos\chi\big)\left[-\frac{a}{2\cos\chi}\,\vec{\mathrm{i}} + \frac{b\,\cos\chi}{2\,\cos\chi}\,\vec{\mathrm{j}} + \left(\frac{2\cos\chi}{2\cos\chi} - \frac{b\sin\chi}{2\cos\chi}\right)\,\vec{\mathrm{k}}\right] \\
&= \big(2\cos\chi\big)\left[-\frac{a}{2\cos\chi}\,\vec{\mathrm{i}} + \frac{b}{2}\,\vec{\mathrm{j}} + \left(1 - \frac{b}{2}\tan\chi\right)\,\vec{\mathrm{k}}\right] \ .
\end{aligned} \tag{C.29}$$

Equating the components of the last line with those in Eq. C.14 we have

$$z_{x'} = \frac{a}{2\cos\chi} \tag{C.30}$$

$$z_{y'} = -\frac{b}{2}\,, \tag{C.31}$$

and the $z$-component checks out:

$$1 = 1 - \frac{b}{2}\cancelto{0}{\tan\chi}. \tag{C.32}$$

Given we know the area of the region of sky (or source) of interest (see Eq. 4.51), the area of the source disk that contributes to the input irradiance can thus be approximated by

$$\begin{aligned}\iint dz_{x'}\, dz_{y'} =& \frac{1}{4}\sec\chi \iint_{R_{\text{sky}}} da\, db \\ =& \frac{1}{4}\,\text{Area}_{\text{sky}}(a,b)\,\sec\chi\,.\end{aligned} \tag{C.33}$$

Furthermore, to be able to integrate in the $(\theta_n, \phi_n)$ coordinate system, a transformation of variables is required, thus

$$\begin{aligned}\iint d\theta_n\, d\phi_n =& \iint \left|\frac{\partial(\theta_n,\phi_n)}{\partial(z_{x'},z_{y'})}\right| dz_{x'}\, dz_{y'} \\ =& \frac{\cos^3\theta_n}{\sin\theta_n}\,\frac{1}{4}\,\text{Area}_{\text{sky}}(\theta_n,\phi_n)\,\sec\chi\,.\end{aligned} \tag{C.34}$$

## REFERENCES


Aas, E. & Højerslev, N. K. 1999. Analysis of underwater radiance observations: Apparent optical properties and analytic functions describing the angular radiance distribution. *Journal of Geophysical Research* **104**, 8015–8024.

Aas, E. & Høkedal, J. 1999. Reflection of spectral sky irradiance on the surface of the sea and related properties—comparison between simulations and field measurements. *Remote Sensing of Environment* **70**, 181–190.

Barkov, V. I., Radvogin, Yu. B., Rumyantsev, Ye. L. & Tikhomirov, V. M. 1979. Influence of aerosols on the polarization of scattered light from a point source. *Izvestiya, Atmospheric and Oceanic Physics* **15**, 189–192. Translated from the Russian.

Barrick, D. 1968. Rough surface scattering based on the specular point theory. *IEEE Transactions on Antennas and Propagation* **AP-16**, 449–454.

Bass, F. G. & Fuks, I. M. 1979. *Wave Scattering from Statistically Rough Surfaces*. New York: Pergamon.

Beckmann, P. 1965. Shadowing of random rough surfaces. *IEEE Transactions on Antennas and Propagation* **AP-13**, 384–388.

Beckmann, P. & Spizzichino, A. 1987. *The Scattering of Electromagnetic Waves from Rough Surfaces*. Norwood, Massachusetts: Artech House.

Born, M. & Wolf, E. 1999. *Principles of Optics*. Cambridge, UK: Cambridge University Press. 7th (expanded) edition.

Brennan, B. & Bandeen, W. R. 1970. Anisotropic reflectance characteristics of natural earth surfaces. *Applied Optics* **9**, 405–412.

Brewster, D. 1830. On the laws of the polarization of light by refraction. *Philosophical Transactions of the Royal Society of London* **120**, 133–144.

Carder, K. L., Reinersman, P., Chen, R. F., Müller-Karger, F., Davis, C. O. & Hamilton, M. 1993. AVIRIS calibration and application in coastal oceanic environments. *Remote Sensing and Environment* **44**, 205–216.

Chandrasekhar, S. 1960. *Radiative Transfer*. New York: Dover.

Chowdhary, J., Cairns, B. & Travis, L. D. 2002. Case studies of aerosol retrievals over the ocean from multiangle, multispectral photopolarimetric remote sensing data. *Journal of Atmospheric Sciences* **59**, 383–397.

Clark, W., Burns, B., Ralston, J. & Dieguez, E. 2004. The measured effects of soils on ground penetrating radar antenna resolution. In *Proceedings of the Tenth International Conference on Ground Penetrating Radar, 21-24 June 2004, Delft, The Netherlands*. pp. 125–128.

Cox, C. & Munk, W. 1954. Measurement of the roughness of the sea surface from photographs of the sun's glitter. *Journal of the Optical Society of America* **44**, 838–850.

Cox, C. & Munk, W. 1956. Slopes of the sea surface deduced from photographs of sun glitter. *Bulletin of the Scripps Institute of Oceanography* **6**, 401–488. URL `http://repositories.cdlib.org/sio/bulletin/6no9`

Cronin, T. W. & Shashar, N. 2001. The linearly polarized light field in clear, tropical marine waters: spatial and temporal variation of light intensity, degree of polarization and e-vector angle. *The Journal of Experimental Biology* **204**, 2461–2467.

Davis, J. M. & Cox, S. K. 1982. Reflected solar radiances from regional scale scenes. *Journal of Applied Meteorology* **21**, 1698–1712.

Flynn, D. S. & Alexander, C. 1995. Polarized surface scattering expressed in terms of a bidirectional reflectance distribution function matrix. *Optical Engineering* **34**, 1646–1650.

Fougnie, B., Frouin, R., Lecomte, P. & Deschamps, P.-Y. 1999. Reduction of skylight reflection effects in the above-water measurement of diffuse marine reflectance. *Applied Optics* **38**, 3844–3856.

Fuks, I. M. 2002. Effective probability density function of rough surface slopes when strong shadowing is present. *Waves in Random Media* **12**, 401–416.

Germer, T. A. 2003. Polarized light diffusely scattered under smooth and rough interfaces. In *Polarization Science and Remote Sensing*, J. A. Shaw & Tyo, J. S. (eds). pp. 193–204. Presented at the Society of Photo-Optical Instrumentation Engineers (SPIE) Conference.

Gershun, A. A. & Popov, O. L. 1955. On the question of the dispersion of light by matte glass. *Svetotekhnika (Illumination Engineering)* **1**, 3–8. In Russian.

Goldstein, D. 2003. *Polarized Light*. New York: Marcel Dekker. 2nd edition.

Govaerts, Y. M. & Verstraete, M. M. 1998. Raytran: a Monte Carlo ray-tracing model to compute light scattering in three-dimensional heterogeneous media. *IEEE Transactions on Geoscience and Remote Sensing* **36**, 493–505.

Gu, Z.-H., Lu, J.-Q., Maradudin, A. A., Martinez, A. & Mendez, E. R. 1993. Coherence in the single and multiple scattering of light from randomly rough surfaces. *Applied Optics* **32**, 2852–2859.

Hapke, B. 1993. *Theory of Reflectance and Emittance Spectroscopy*. Cambridge, UK: Cambridge University Press.

Hapke, B. 1998. The opposition effect of the moon: coherent backscattering *and* shadow hiding. *Icarus* **133**, 89–97.

He, X. D., Torrance, K. E., Sillion, F. X. & Greenberg, D. P. 1991. A comprehensive physical model for light reflection. In *SIGGRAPH '91: Proceedings of the 18th Annual International Conference on Computer Graphics and Interactive Techniques*. New York: ACM Press, pp. 175–186.

Hébert, M. 2006. *Compositional model for predicting multilayer reflectances and transmittances in color reproduction*. Ph.D. thesis, École Polytechnique Fédérale de Lausanne. URL `http://diwww.epfl.ch/w3lsp/publications/colour/Thesis-hebert.pdf`.

Hochberg, E. J. & Atkinson, M. J. 2000. Spectral discrimination of coral reef benthic communities. *Coral Reefs* **19**, 164–171.

Høkedal, J. & Aas, E. 1998. Observations of spectral sky radiance and solar irradiance, *Report 103*. Department of Geophysics, University of Oslo, Oslo, Norway.

Hoover, B. G. & Gamiz, V. L. 2006. Coherence solution for bidirectional reflectance distributions of surfaces with wavelength-scale statistics. *Journal of the Optical Society of America A* **23**, 314–328.

Horváth, G. & Varjú, D. 1995. Underwater refraction—polarization patterns of skylight perceived by aquatic animals through Snell's window of the flat water surface. *Vision Research* **35**, 1651–1666.
URL `http://www.ingentaconnect.com/content/els/00426989/1995/00000035/00000012/art00254`

Hu, B., Lucht, W. & Strahler, A. H. 1999. The interrelationship of atmospheric correction of reflectances and surface BRDF retrieval: a sensitivity study. *IEEE Transactions on Geoscience and Remote Sensing* **37**, 724–738.

Hulburt, E. O. 1934. Polarization of light at sea. *Journal of the Optical Society of America* **24**, 35–42.

Hurwitz, H. J. & Jones, R. C. 1941. A new calculus for the treatment of optical systems. II. Proof of three general equivalence theorems. *Journal of the Optical Society of America* **31**, 493–499.

ISO 1992. Solar energy: reference solar spectral irradiance at the ground at different receiving conditions. Direct normal and hemispherical solar irradiance for air mass 1,5, ISO 9845–1. International Organization for Standardization.

ISO 2004. Spatial distribution of daylight—CIE standard general sky. ISO 15469:2004(E), CIE S 011/E:2003. Prepared by the International Commission on Illumination (CIE). International Organization for Standardization.

Ivanoff, A. & Waterman, T. H. 1958. Factors, mainly depth and wavelength, affecting the degree of underwater light polarization. *Journal of Marine Research* **16**, 283–307.

Ivanov, A. P. & Prikhach, A. S. 1976. Fluctuation behavior of the intensity of light reflected by a sinusoidal wave. *Izvestiya, Atmospheric and Oceanic Physics* **12**, 728–732. In English.

Ivanov, A. P. & Toporets, A. S. 1956. Investigation of diffuse reflection by means of polarized light. I. *Journal of Technical Physics of the Academy of Sciences of the USSR* **1**, 598–604. Translated and published by the American Institute of Physics from the Russian original, Vol. 36, No. 3.

Jin, Z. & Simpson, J. J. 1999. Bidirectional anisotropic reflectance of snow and sea ice in AVHRR Channel 1 and 2 spectral regions. I. Theoretical analysis. *IEEE Transactions on Geoscience and Remote Sensing* **37**, 543–554.

Jones, R. C. 1941a. New calculus for the treatment of optical systems. I. Description and discussion of the calculus. *Journal of the Optical Society of America* **31**, 488–493.

Jones, R. C. 1941b. New calculus for the treatment of optical systems. III. The Sohncke theory of optical activity. *Journal of the Optical Society of America* **31**, 500–503.

Jones, R. C. 1942. A new calculus for the treatment of optical systems. IV. *Journal of the Optical Society of America* **32**, 486–493.

Jones, R. C. 1947a. A new calculus for the treatment of optical systems. V. A more general formulation, and description of another calculus. *Journal of the Optical Society of America* **37**, 107–110.

Jones, R. C. 1947b. A new calculus for the treatment of optical systems. VI. Experimental determination of the matrix. *Journal of the Optical Society of America* **37**, 110–112.

Jones, R. C. 1948. New calculus for the treatment of optical systems. VII. Properties of the N-matrices. *Journal of the Optical Society of America* **38**, 671–685.

Jones, R. C. 1956. New calculus for the treatment of optical systems. VIII. Electromagnetic theory. *Journal of the Optical Society of America* **46**, 126–131.

Joyce, K. E. & Phinn, S. E. 2002. Bi-directional reflectance of corals. *International Journal of Remote Sensing* **23**, 389–394.

Kattawar, G. W. & Adams, C. N. 1989. Stokes vector calculations of the submarine light field in an atmosphere-ocean with scattering according to a Rayleigh phase matrix: Effect of interface refractive index on radiance and polarization. *Limnology and Oceanography* **34**, 1453–1472.
URL `http://new.aslo.org/lo/toc/vol_34/issue_8/1453.pdf`

Kattawar, G. W. & Plass, G. N. 1976. Asymptotic radiance and polarization in optically thick media: ocean and clouds. *Applied Optics* **15**, 3166–3178.

Koenderink, J. J., van Doorn, A. J., Dana, K. J. & Nayar, S. 1999. Bidirectional reflection distribution function of thoroughly pitted surfaces. *International Journal of Computer Vision* **31**, 129–144.

Kokhanovsky, A. A. 2003. Parameterization of the Mueller matrix of oceanic waters. *Journal of Geophysical Research* **108**, 3175–3178.

Lambert, J. H. 1760. *Photometria sive de mensure de gratibus luminis, colorum umbrae*. Augsburg: Eberhard Klett. Translation into English by D. DiLaura, (IESNA, 2001).

Levin, N., Ben-Dor, E. & Karnieli, A. 2004. Topographic information of sand dunes as extracted from shading effects using Landsat images. *Remote Sensing of Environment* **90**, 190–209.

Liang, S. & Strahler, A. H. 1993. An analytic BRDF model of canopy radiative transfer and its inversion. *IEEE Transactions on Geoscience and Remote Sensing* **31**, 1081–1092.

Liu, Y. & Voss, K. 1997. Polarized radiance distribution measurement of skylight. II. Experiment and data. *Applied Optics* **36**, 8753–8764.

Lord Rayleigh 1910. Colours of sea and sky. *Nature* **83**.

Louchard, E. M., Reid, R. P., Stephens, F. C., Davis, C. O., Leathers, R. A. & Downes, T. V. 2003. Optical remote sensing of benthic habitats and bathymetry in coastal environments at Lee Stocking Island, Bahamas: a comparative spectral classification approach. *Limnology and Oceanography* **48**, 511–521.

Luchinin, A. G. 1979. Influence of wind waves on the characteristics of the light field backscattered by the bottom and the intervening water. *Izvestiya, Atmospheric and Oceanic Physics* **15**, 531–534. In English.

Luchinin, A. G. & Sergiyevskiy 1986. Effect of surface waves on the color of the sea. *Izvestiya, Atmospheric and Oceanic Physics* **22**, 600–603. In English.

Lyzenga, D. R. 1978. Passive remote-sensing techniques for mapping water depth and bottom features. *Applied Optics* **17**, 379–383.

Maignan, F., Bréon, F.-M. & Lacaze, R. 2004. Bidirectional reflectance of Earth targets: evaluation of analytical models using a large set of spaceborne measurements with emphasis on the Hot Spot. *Remote Sensing of Environment* **90**, 210–220.

Martonchik, J. V., Bruegge, C. J. & Strahler, A. H. 2000. A review of reflectance nomenclature used in remote sensing. *Remote Sensing Reviews* **19**, 9–20.

Matchko, R. M. & Gerhart, G. R. 2005. Polarization azimuth angle in daylight scenes. *Optical Engineering* **44**, 8001–8009.

McCluney, W. R. 1994. *Introduction to Radiometry and Photometry*. Boston: Artech House.

Meerkoetter, R. 1990. Reflection functions for inhomogeneous land surfaces. *Applied Optics* **29**, 4192–4198.

Meister, G., Rothkirch, A., Spitzer, H. & Bienlein, J. 2001. Width of the specular peak perpendicular to the principal plane for rough surfaces. *Applied Optics* **40**, 6072–6080.

Meister, G., Wiemker, R., Monno, R., Spitzer, H. & Strahler, A. 1998. Investigation on the Torrance-Sparrow specular BRDF model. In *Proceedings of the IEEE International Geoscience and Remote Sensing Symposium, Seattle, Washington, 06-10 July 1998*. pp. 2095–2096.
URL `citeseer.ist.psu.edu/meister98investigation.html`

Meyers, J. P. 2002. *Modeling Polarimetric Imaging using DIRSIG*. Ph.D. thesis, Rochester Institute of Technology, Rochester, New York.

Millar, R. F. 1973. The Rayleigh hypothesis and a related least-squares solution to scattering problems for periodic surfaces and other scatterers. *Radio Science* **8**, 785–796.

Minnaert, M. 1941. The reciprocity principle in lunar photometry. *The Astrophysical Journal* **93**, 403–410.

Minnaert, M. 1942. The reflection of light in rippled surfaces. *Physica* **9**, 925–935.

Minnaert, M. 1948. *The Nature of Light and Colour in the Open Air*. New York: Dover.

Mobley, C. D. 1994. *Light and Water: Radiative Transfer in Natural Waters*. San Diego: Academic Press.
URL `http://www.curtismobley.com/lightandwater.zip`

Mobley, C. D. 2006. *Hydrolight Technical Documentation*. Sequoia Scientific, Inc.
URL `http://www.sequoiasci.com/products/Hydrolight.aspx`

Mobley, C. D. & Mazel, C. 1999. Informal notes on reflectances. Prepared for the *1999 Coastal Benthic Optical Properties (CoBOP) Principal Investigators Meeting* (draft copy).

Mobley, C. D. & Sundman, L. K. 2003. Effects of optically shallow bottoms on upwelling radiances: Inhomogeneous and sloping bottoms. *Limnology and Oceanography* **48**, 329–336.

Mobley, C. D., Zhang, H. & Voss, K. J. 2003. Effects of optically shallow bottoms on upwelling radiances: bidirectional reflectance distribution function effects. *Limnology and Oceanography* **48**, 337–345.

Mullamaa, Yu. R. 1962. Diffuse reflection and transmission of light in case of rough surface separating two isotropic mediums. *Izvestiia Akademii nauk SSSR, Seriia geofizicheskaia.* **5**, 5–22. In Russian, with English abstract.

Mullamaa, Yu. R. 1964. The reflection of direct radiation from an ocean surface. *Bulletin of the Academy of Sciences of the U.S.S.R., Geophysics series.* **8**, 1232–1246. Translated from the Russian by C. M. Wade, American Geophysical Union.

Nicodemus, F. E. (ed.). 1976. *Self-study manual on optical radiation measurements —Part 1: Concepts*. Washington, D.C.: U.S. Department of Commerce, National Bureau of Standards (NBS).

Nicodemus, F. E., Richmond, J. C., Hsia, J. J., Ginsberg, I. W. & Limperis, T. 1977. Geometrical considerations and nomenclature for reflectance, *Technical report*. National Bureau of Standards, Washington, D.C.

Oren, M. & Nayar, S. K. 1995. Generalization of the Lambertian model and implications for machine vision. *International Journal of Computer Vision* **14**, 227–251.

Otremba, Z. 2003. Relationships between quantities describing reflective features of both land and ocean areas. Presented at the Second International Conference on Current Problems in Optics of Natural Waters, St. Petersburg, Russia, 8–12 Sept. 2003.
URL `http://www.am.gdynia.pl/~zotremba/badania/publikacje/ONW2003-Otremba.pdf`

Otremba, Z. 2004. Modelling the bidirectional reflectance distribution functions (BRDF) of sea areas polluted by oil. *Oceanologia* **46**, 505–518.

Philpot, W. D. 1989. Bathymetric mapping with passive multispectral imagery. *Applied Optics* **28**, 1569–1578.

Plass, G. N., Kattawar, G. W. & Guinn, J. A., Jr. 1975. Radiative transfer in the earth's atmosphere and ocean: influence of ocean waves. *Applied Optics* **14**, 1924–1936.

Premože, S. & Ashikhmin, M. 2001. Rendering natural waters. *Computer Graphics Forum* **20**, 189–199.
URL `citeseer.ist.psu.edu/article/premoze00rendering.html`

Press, W. H., Teukolsky, S. A., Vetterling, W. T. & Flannery, B. P. 1992. *Numerical Recipes in FORTRAN 77. The art of scientific computing.* Cambridge University Press. 2nd edition.
URL `http://www.nrbook.com/a/bookfpdf.php`

Priest, R. G. & Germer, T. A. 2000. Polarimetric BRDF in the microfacet model: theory and measurements. In *Proceedings of the 2000 Meeting of the Military Sensing Symposia Specialty Group on Passive Sensors*. pp. 169–181.
URL `http://physics.nist.gov/Divisions/Div844/publications/germer/GermerPriestMicroFacet.pdf`

Priest, R. G. & Meier, S. R. 2002. Polarimetric microfacet scattering theory with applications to absorptive and reflective surfaces. *Optical Engineering* **41**, 988–993.

Sabbah, S., Barta, A., Gál, J., Horváth, G. & Shashar, N. 2006. Experimental and theoretical study of skylight polarization transmitted through Snell's window of a flat water surface. *Journal of the Optical Society of America A* **23**, 1978–1988.

Sandmeier, St., Müller, Ch., Hosgood, B. & Andreoli, G. 1998a. Physical mechanisms in hyperspectral BRDF data of grass and watercress. *Remote Sensing of Environment* **66**, 222–233.

Sandmeier, St., Müller, Ch., Hosgood, B. & Andreoli, G. 1998b. Sensitivity analysis and quality assessment of laboratory BRDF data. *Remote Sensing of Environment* **64**, 176–191.

Sandmeier, S. R. 2000. Acquisition of bidirectional reflectance factor data with field goniometers. *Remote Sensing of Environment* **73**, 257–269.

Satlantic, Inc. 2000. HyperTSRB User's Manual. Revision 6.1.

Sears, F. W. 1949. *Optics*. Cambridge, Massachusetts: Addison-Wesley Press, Inc., Principles of Physics Series.

Shen, J. & Maradudin, A. A. 1980. Multiple scattering of waves from random rough surfaces. *Physical Review B* **22**, 4234–4240.

Simonot, L. & Obein, G. 2007. Geometrical considerations in analyzing isotropic or anisotropic surface reflections. *Applied Optics* **46**, 2615–2623.

Smith, B. G. 1967. Geometrical shadowing of a random rough surface. *IEEE Transactions on Antennas and Propagation* **AP-15**, 668–671.

Smith, R. C. 1974. Structure of solar radiation in the upper layers of the sea. In *Optical Aspects of Oceanography*, N. G. Jerlov & Nielsen, E. S. (eds). London: Academic Press, pp. 95–119.

Smith, R. C. & Baker, K. S. 1981. Optical properties of the clearest natural waters (200-800nm). *Applied Optics* **20**, 177–184.

Snyder, W. C. 1998. Reciprocity of the bidirectional reflectance distribution function (BRDF) in measurements and models of structured surfaces. *IEEE Transactions on Geoscience and Remote Sensing* **36**, 685–691.

Snyder, W. C. 2002. Definition and invariance properties of structured surface BRDF. *IEEE Transactions on Geoscience and Remote Sensing* **40**, 1032–1037.

Stagg, B. J. & Charalampopoulos, T. T. 1991. Surface-roughness effects on the determination of optical properties of materials by the reflection method. *Applied Optics* **30**, 4113–4118.

Takashima, T. & Masuda, K. 1985. Degree of radiance and polarization of the upwelling radiation from an atmosphere-ocean system. *Applied Optics* **24**, 2423–2429.

Timofeeva, V. A. 1957. Distribution of light in the sea. *Works of the Marine Hydrophysics Institute, Academy of Sciences of the USSR* **11**, 97–104. In Russian.

Timofeeva, V. A. 1962. Spatial distribution of the degree of polarization of natural light in the sea. *Bulletin of the Academy of Sciences of the U.S.S.R., Geophysics series.* **12**, 1160–1164. Translated into English by L. G. Robbins, American Geophysical Union.

Torrance, K. E. & Sparrow, E. M. 1967. Theory of off-specular reflection from roughened surfaces. *Journal of the Optical Society of America* **57**, 1105–1114.

Tyler, J. E. 1960. Radiance distribution as a function of depth in an underwater environment. *Bulletin of the Scripps Institute of Oceanography* **7**, 363–412.

Tynes, H., Kattawar, G. W., Zege, E. P., Katsev, I. L., Prikhach, A. S. & Chaikovskaya, L. I. 2001. Monte Carlo and multicomponent approximation methods for vector radiative transfer by use of effective Mueller matrix calculations. *Applied Optics* **40**, 400–412.

Tyo, J. S., Goldstein, D. L., Chenault, D. B. & Shaw, J. A. 2006. Review of passive imaging polarimetry for remote sensing applications. *Applied Optics* **45**, 5453–5469.

van Ginneken, B., Stavridi, M. & Koenderink, J. J. 1998. Diffuse and specular reflectance from rough surfaces. *Applied Optics* **37**, 130–139.

van Weiringen, J. S. 1947. Reflection of light by rippled water surfaces. *Proceedings of the Koninklijke Nederlandse Akademie van Wetenschappen* **50**, 952–958. Communicated by M. Minnaert on 27 September 1947.

Voss, K. J., Mobley, C. D., Sundman, L. K., Ivey, J. E. & Mazel, C. H. 2003. The spectral upwelling radiance distribution in optically shallow waters. *Limnology and Oceanography* **48**, 364–373.

Walker, R. E. 1994. *Marine Light Field Statistics*. New York: Wiley.

Waterman, P. C. 1975. Scattering by periodic surfaces. *Journal of the Acoustical Society of America* **57**, 791–802.

Waterman, T. H. 1954. Polarization patterns in submarine illumination. *Science* **120**, 927–932.

Wellems, D., Ortega, S., Bowers, D., Boger, J. & Fetrow, M. 2006. Long wave infrared polarimetric model: theory, measurements and parameters. *Journal of Optics A: Pure and Applied Optics* **8**, 914–925.
URL `http://www.ingentaconnect.com/content/iop/jopta/2006/00000008/00000010/art00014`

Wentz, F. J. 1976. Cox and Munk's sea surface slope variance. *Journal of Geophysical Research* **81**, 1607–1608.

Wolff, L. B. 1994. Diffuse-reflectance model for smooth dielectric surfaces. *Journal of the Optical Society of America A* **11**, 2956–2968.

Wynn, C. 2000a. An introduction to BRDF-based lighting, *Technical report*. NDVIA Corporation. URL `chris.wynn@ndvia.com`.

Wynn, C. 2000b. Real-time BRDF-based lighting using cube-maps, *Technical report*. NDVIA Corporation.
URL `http://pages.cpsc.ucalgary.ca/~mario/591/PR/6-reflection-models/BRDF/BRDFSeparable.pdf`

Yang, P., Wei, H., Kattawar, G. W., Hu, Y. X., Winker, D. M., Hostetler, C. A. & Baum, B. A. 2003. Sensitivity of the backscattering Mueller matrix to particle shape and thermodynamic phase. *Applied Optics* **42**, 4389–4395.

Zaki, K. A. & Neureuther, A. R. 1971a. Scattering from a perfectly conducting surface with a sinusoidal height profile: TE polarization. *IEEE Transactions on Antennas and Propagation* **AP-19**, 208–214.

Zaki, K. A. & Neureuther, A. R. 1971b. Scattering from a perfectly conducting surface with a sinusoidal height profile: TM polarization. *IEEE Transactions on Antennas and Propagation* **AP-19**, 747–751.

Zaneveld, J. R. V. & Boss, E. 2003. The influence of bottom morphology on reflectance: theory and two-dimensional geometry model. *Limnology and Oceanography* **48**, 374–379.

Zhang, H., Voss, K. J. & Reid, R. P. 2003a. Determining the influential depth for surface reflectance of sediment by BRDF measurements. *Optics Express* **11**, 2654–2665.

Zhang, H., Voss, K. J., Reid, R. P. & Louchard, E. M. 2003b. Bidirectional reflectance measurements of sediments in the vicinity of Lee Stocking Island, Bahamas. *Limnology and Oceanography* **48**, 380–389.

Zhu, Q. Z. & Zhang, Z. M. 2004. Anisotropic slope distribution and bidirectional reflectance of a rough silicon surface. *Journal of Heat Transfer* **126**, 985–992.